Development and Evaluation of Relaxation-Based Measures of Myelin Content and Microstructure in Rodent Brains

By

Kathryn Louise West

Dissertation
Submitted to the Faculty of the
Graduate School of Vanderbilt University
in partial fulfillment of the requirements
for the degree of

DOCTOR OF PHILOSOPHY
in

Biomedical Engineering
December, 2016
Nashville, Tennessee

Approved:

Mark D. Does, Ph.D.

Adam W. Anderson, Ph.D.

Kevin C. Ess, MD, Ph.D.

Daniel F. Gochberg, Ph.D.

John C. Gore, Ph.D.

ACKNOWLEDGEMENTS

The work in this dissertation would not have been possible without the help and support from many people and funding sources. I would first like to thank the financial support from my Graduate Research Fellowship from the National Science Foundation and the grant for Sub-voxel tissue characterization with MRI from the National Institute of Health. I would also like to thank all of the support from Dr. Gore and the staff and resources at the Vanderbilt University Institute of Imaging Science. It has been a pleasure and to be trained at such a collaborative and well-respected institution. I want to especially thank my advisor, Dr. Mark Does for his mentorship, knowledge, and teaching throughout the years. While I might have not appreciated his critical experimental and writing approaches some days along the way, I am now very grateful for learning from someone I truly respect as a great experimental researcher, writer, and teacher.

The entire Does lab has been a great encouragement over the years, especially Nate, who directly helped make much of the work in this dissertation possible and Mary Kate who was a source of daily motivation and laughter. My friends and family have also been essential throughout my education, providing much love and support. Over all of the highs and lows of grad school, I want to thank Drew, Elise, Elizabeth and Courtney for their constant reassurance and moral support and understanding. Finally, I want to especially thank my parents, Carey and Vicki West for instilling in me the importance of education and a strong work ethic and always pushing and supporting me to do my best.

TABLE OF CONTENTS

Page

LIST OF TABLES

LIST OF FIGURES

CHAPTER 1

INTRODUCTION

Rodent models of white matter disease are of great interest in neurobiology and neurodevelopment to increase the understanding of pathology, disease progression, and treatment options. While histology is the current gold standard for determining the degree of myelination and microstructural characteristics in white matter, it is limited to *ex vivo* tissue with small coverage area, requires many tissue-preparation steps and is relatively time-consuming. In contrast, imaging, specifically magnetic resonance imaging (MRI), provides an opportunity to directly assess myelination, and potentially microstructure either non-invasively (*in vivo*) or non-destructively (*ex vivo*) across whole brain in a more time-efficient manner. In addition, imaging methods have the ability to link rodent studies to clinically relevant human diagnosis and monitoring.

While two quantitative relaxation-based MRI techniques display correlative measures to myelin content, neither can provide an absolute measure of the volume of myelin similar to histology. In addition to the myelin volume, histology provides further microscopic information such as axon size and myelin thickness. However, MRI is inherently macroscopic with resolution ~ 100X greater than the average axon size. Previous work has shown the potential for obtaining microscopic information using MRI, but there has been a lack of validation to histology. Therefore, the work in this dissertation aims to fill the gaps of both macroscopic and microscopic imaging of myelin with MRI by:

1. Developing MRI and histology methods for rodent brain

2. Validating myelin volume imaging in multiple animal models
3. Evaluating microstructural information from g-ratio imaging

CHAPTER 2

BACKGROUND

2.1 WHITE MATTER AND MYELIN

The mammalian nervous system is mainly comprised of two types of tissue, gray and white matter. Neurons are the major cellular component of the central and peripheral nervous systems (CNS and PNS, respectively) that transmit and receive signals to and from the rest of the body. Axons extend as long projections from the neuronal cell body and provide the pathway for signal transmission. In white matter, to increase conduction speed along the axon, myelin surrounds the axons in a sheath-like structure, seen in Fig 2.1 (1–3).

Myelin is composed of ~ 80% lipid and 20% protein and forms in a lamellar, membranous structure around the axon. The layers of myelin run in a nodal fashion along the axon, creating nodes of Ranvier, which are small breaks in the myelin. In order to increase the speed of action potential conduction down the axon, myelin electrically insulates the axons between nodes. This induces salutatory conduction from one node of Ranvier to the next instead of traversing the entire length of the axon. This is a vital aspect of complex neuronal sensory, motor, and behavioral functionality (4). The myelin bilayers wrap around the axons leaving space between layers, which is filled with water as seen in Fig 2.1. This water makes up ~ 40% of myelin weight and is called myelin water (1).

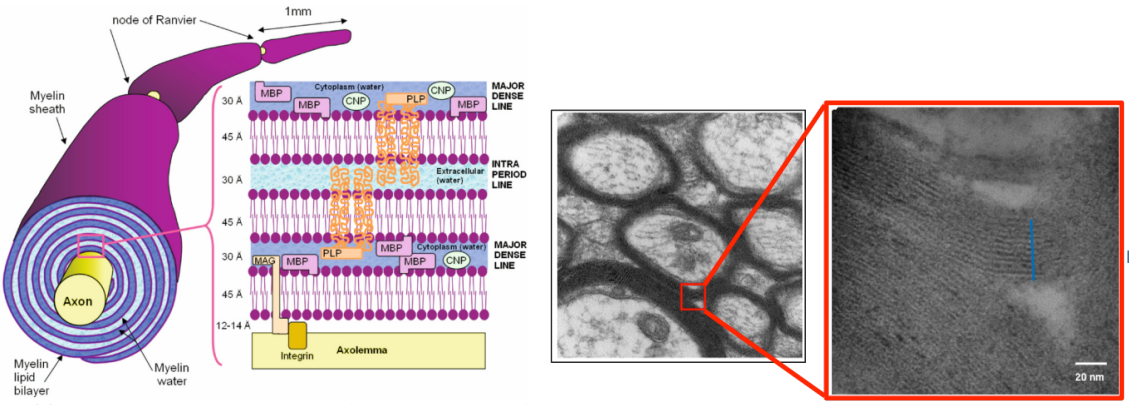

Figure 2.1. Diagram and microscopy of myelin. (Left) Diagram of a myelinated axon along with a close up of the make-up of the lipid bilayers (4). (Right) Electron microscopy images of myelinated axons from a mouse brain. The high resolution image displays a similar banding pattern between lipids and water layers as shown in the diagram.

Since myelin can increase conduction speed 10 to 100X, demyelinated axons or damage to the myelin layers can drastically inhibit neuronal health. Decreased speed of signal transmission has the largest effect on complex motor and sensory signaling, which leads to neuronal diseases. This can be seen in many neurodegenerative disease, such as Multiple Sclerosis (MS) and developmental disorders such as Tuberous Sclerosis Complex (TSC). These diseases have been shown to be directly related to the health of the myelin content and structure (5–7). Consequently, the ability to quantitatively monitor myelin content and structure would be quite advantageous to assess disease progression as well as treatment efficacy (4).

2.1.1 Axon And Myelin Geometry

Myelin is produced by oligodendrocytes in the CNS and Schwann cells in the PNS. Oligodendrocytes are branched and myelinate multiple axons while Schwann cells myelinate only one axon. The thickness of myelin is largely believed to be dependent on the size of the axon (8). This is not surprising since axon size and myelin thickness are inversely proportionate

to conduction velocity along the axon. We can quantify this relationship by the g-ratio, the ratio of axon radius to myelinated fiber radius as shown in Fig 2.2.

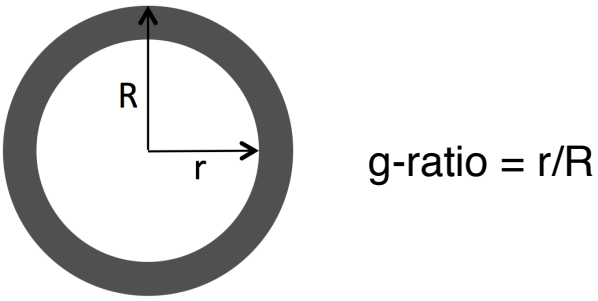

Figure 2.2. Diagram of the g-ratio of myelinated axon**.**

The g-ratio is known to change as myelination occurs during development as well as demyelination disease processes. Therefore, this quantitative metric has been strongly associated as a more specific measure of white matter and myelin health (9).

2.2 MYELIN DEVELOPMENT AND TRANSGENIC MODELS

The PI3K/Akt/mTOR (mammalian target of rapamycin) pathway has proven to be a key pathway of myelination through displayed involvement in myelin development and differentiation of oligodendrocyte precursor cells (OPCs). In this work, several transgenic mouse models are used to interrogate the role of different players in the PI3K/Akt/mTOR pathway shown below in Fig 2.3 with a star signifying the genes targeted (10)**.**

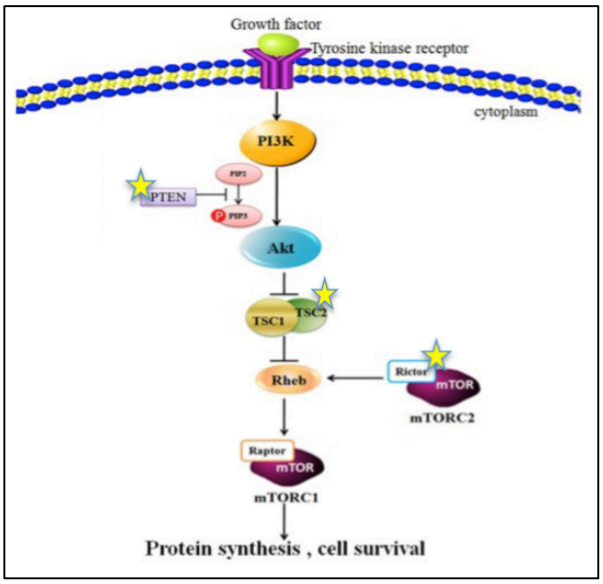

Figure 2.3. Diagram of the PI3K/Akt/mTOR pathway. Stars signify the three genes targeted in conditional knockout models in this work (10).

All transgenic models were conditional knockouts, mutating the gene of interest only in oligodenrocytes and oligodenrocyte precursor cells (OPCs). This was done using the Cre-recombinase technique and an *Olig2* promoter.

The first model targets the *Tsc2* gene. The Tuberous Sclerosis Complex (TSC) includes both *TSC1* and *TSC2* which inhibit mTORC1 (mammalian target of rapamycin complex) and activate mTORC2 signaling. Therefore, deletion of either gene activates mTORC1 and inhibits mTORC2 signaling. When *Tsc*2 is conditionally knocked out there is a decrease in the number and the maturation of oligodendrocytes, which maybe contribute to the decrease in myelination (7). *Rictor* is targeted in the second model which is required for mTORC2 signaling and embryonic development. Since *Rictor* is directly related to mTORC2 signaling, by targeting *Rictor,* (in comparison to *Tsc2*), the model is more specific to determine contributions if mTORC2 signaling. While myelination decreases in this model, it is not as drastic as with the conditional knockout of *Tsc2* suggesting that mTORC2 is not completely responsible for changes

associated with *Tsc2* (11–13). The third model targets *Pten* (phosphatase and tensin homologue deleted on chromosome 10), which affects the PI3K pathway upstream of *Tsc*2 and *Rictor*. Deletion of *Pten* is known to be characteristic of high-grade tumors since it negatively regulates the PI3K pathway resulting in cell proliferation. In oligodendrocytes and OPCs, deletion of *Pten* overactivates *Akt* and downstream mTOR and has been shown to result in thicker myelin (14). Between the three conditional knockout models, we can interrogate changes in myelin from changes in the PI3K pathway as a whole (*Pten*), after *Akt* signaling (*Tsc2*), and at a key endpoint protein of the pathway (*Rictor*). This provides a rich data set for understanding myelin development and imaging capabilities.

2.3 FUNDAMENTALS OF NUCLEAR MAGNETIC RESONANCE (15)

Magnetic resonance imaging (MRI) relies on the basic principles of nuclear magnetic resonance (NMR). Nuclei that have unpaired protons, such as ^{1}H, exhibit spin and act as magnetic dipoles. While the spins are normally randomly-oriented, when placed in an external magnetic field ($\vec{B}_0$) in the *z*-axis, these spins align with $\vec{B}_0$ either parallel or anti-parallel. There is a small excess of spins aligned parallel and thus there is a net magnetic moment ($\vec{\mu}$). Due to the net torque on $\vec{\mu}$ from the magnetic field, we can describe the motion of $\vec{\mu}$ as

$$\frac{d\vec{\mu}}{dt} = \gamma\vec{\mu} \times \vec{B}_0 \qquad [2.1]$$

which describes a precession of $\vec{\mu}$ about $\vec{B}_0$ with an angular frequency (ω_0) of

$$\omega_0 = \gamma B_0 \qquad [2.2]$$

where γ is the gyromagnetic ratio, which is ~2.68x10^8 rad/s/T or γ/2π ~ 42.6 MHz/T for ^{1}H protons and B_0 is in units of Telsa [T]. We call ω_0 the Larmor precession frequency, which is dependent on the external magnetic field strength (B_0) shown in *Eq*. 2.2.

Instead of describing individual spins ($\vec{\mu}$), we can describe a sum of protons as a magnetization vector, $\overrightarrow{M}$. As before, we can describe the equation of motion of $\overrightarrow{M}$ due to an external magnetic field ($\vec{B}_{\text{ext}}$) as

$$\frac{d\overrightarrow{M}}{dt} = \gamma \overrightarrow{M} \times \vec{B}_{ext} \qquad [2.3]$$

When $\vec{B}_{\text{ext}}$ is a constant field ($\vec{B}_0$), $\overrightarrow{M}$ is in equilibrium (M_0) and precessing at ω_0. To obtain signal, we need to perturb the spins by applying another magnetic field ($\vec{B}_1$), orthogonal to $\vec{B}_0$ at the Larmor frequency. Therefore, now $\vec{B}_{\text{ext}} = \vec{B}_0\hat{z} + \vec{B}_1\hat{x}$ and we can write *Eq*. 2.3 in terms of each axis as

$$\begin{aligned} \frac{dM_x}{dt} &= (\omega_0 - \omega)M_y \\ \frac{dM_y}{dt} &= -(\omega_0 - \omega)M_x + \omega_1 M_z \\ \frac{dM_z}{dt} &= -\omega_1 M_y \end{aligned} \qquad [2.4]$$

where $\omega_1 = \gamma B_1$ and ω is the angular frequency of the rotating reference frame. The angle that $\overrightarrow{M}$ is tipped from the *z*-axis (θ) is dependent of the strength and duration of $\vec{B}_1$ for a constant amplitude, rectangular pulse as

$$\theta = \gamma B_1 t = \omega_1 t\,. \qquad [2.5]$$

Assuming $\omega = \omega_0$ and $M_z(0) = M_0$ we can solve *Eq*. 2.4 as,

$$M_x(t) = 0$$
$$M_y(t) = M_0 \sin(\omega_1 t) \qquad [2.6]$$
$$M_z(t) = M_0 \cos(\omega_1 t)$$

2.3.1 Relaxation (15)

Spins aligned with the main, static magnetic field are at a state of minimum energy; after magnetization is flipped to the transverse plane, the spins now have higher energy. In order to return to equilibrium, spins interact with the local environment and transfer energy to the surrounding lattice. The return to equilibrium, or relaxation, can be described as,

$$\frac{dM_z}{dt} = \frac{1}{T_1}\left(M_0 - M_z\right) \qquad [2.7]$$

where T_1 is the spin-lattice relaxation time. Transverse magnetization decreases in time due to this longitudinal recovery, but it also decreases due to interactions between spins. Some spins may precess at frequencies slightly higher or lower than Larmor frequency, which changes the phase of the spins. When these spins are summed, phase coherence is lost and the magnetization vector decreases. This process can be described as below

$$\frac{dM_\perp}{dt} = -\frac{1}{T_2}\left(M_\perp\right) \qquad [2.8]$$

where $M_\perp$ is the magnetization in the transverse (*x*-*y*) plane and T_2 is the spin-spin relaxation time. The T_2 is affected by the motion of spins. For example, spins that are moving around more (such as free water) have an averaging out effect in phase and a slower decrease in transverse magnetization.

As before, we can solve *Eqs.* 2.7 and 2.8 to describe relaxation in time.

$$M_{\perp}(t) = M_{\perp}(0) * \exp\left(\frac{-t}{T_2}\right)$$
$$M_z(t) = M_0 + \left[M_z(0) - M_0\right] * \exp\left(\frac{-t}{T_1}\right) \quad [2.9]$$

We see that $M_{\perp}$ decays exponentially with time constant T_2 and M_z recovers back to equilibrium exponentially with time constant T_1. Relaxation time constants are characteristic to different tissue types and used to create a variety of contrasts as described below.

2.4 CURRENT WHITE MATTER MRI TECHNIQUES

Magnetic Resonance Imaging is a very valuable tool in brain imaging, providing contrast between gray and white matter. While qualitative techniques can detect gross changes to tissue, such as MS lesions, these techniques are nonspecific to underlying pathology and white matter health. Information obtained from more advanced quantitative techniques can probe more specific changes to tissue microstructure and provide more detailed information about the disease, its progression and/or drug treatment efficacy (16).

As described above, myelin is mainly a lipid structure, which has a very short-lived signal from lipids (< 1 ms), making direct imaging of myelin difficult. Therefore, most current techniques can only indirectly investigate myelin and axon integrity based on myelin water or interactions between water and myelin. Current myelin imaging approaches include qualitative T_1-weighted (spin-lattice relaxation) and T_2-weighted (spin-spin relaxation) imaging, as well as quantitative measures of MR Spectroscopy (MRS), Diffusion Tensor Imaging (DTI), Magnetization Transfer Imaging (MTI), and Multi-Exponential T_2 imaging (MET_2) (4). T_2-weighted images provide highly sensitive contrast based on spin-spin relaxation (T_2) differences. In normal myelinated white matter, the water in axons and between myelin sheaths has shorter T_1

and T_2 values compared to gray matter. This results in hypointense white matter structures on T_2-weighted images and hyperintense signal in T_1-weighted images compared to gray matter (17).

Beyond qualitative imaging, quantitative imaging techniques such as MRS and DTI provide more specific, microscopic information. MR Spectroscopy provides the ability to detect signal from metabolites in the brain, which provides very particular information about pathology and metabolism, providing insight into disease mechanisms (4). Diffusion Tensor Imaging is capable of detecting changes in the direction and anisotropy of water diffusion. In the brain, axons are highly directional, creating a strong diffusion anisotropy with water diffusing axially (along the axon) much more than radially. In axon degeneration or demyelination, axon integrity is lost and DTI can detect this as a change in the diffusion anisotropy (18,19). While MRS and DTI are sensitive to myelin, MET_2 and MTI have been investigated as more specific biomarkers of myelin.

2.4.1 Mutli-Exponential T_2

MET_2 imaging is based on the spin echo pulse sequence seen in Fig 2.4 (20,21).

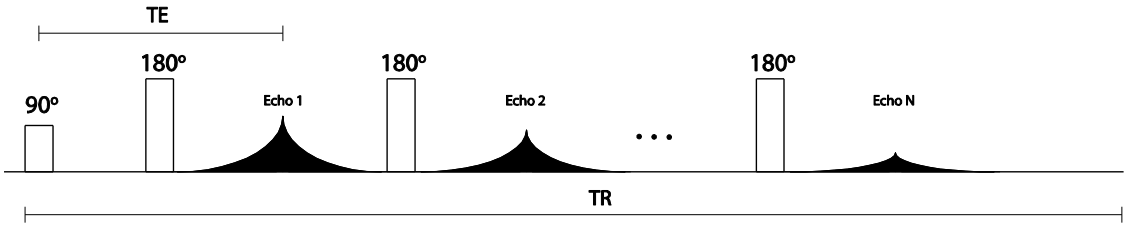

Figure 2.4. Multi-exponential T_2 experiment pulse diagram. A 90-degree excitation pulse is followed by a train of 180-degree pulses to sample the T_2 decay.

In a spin echo experiment, signal is rotated from alignment with B_o to the transverse plane by a 90-degree excitation pulse. After excitation, signal dephases exponentially in the transverse

plane at the rate $R_2^* = 1/T_2^*$; therefore, at a time, $T_E/2$ after the 90-degree pulse, a 180-degree refocusing pulse is applied. The refocusing pulse flips the spins and they begin to rephase, increasing transverse signal exponentially. Since spins rephase at the same rate as dephasing, after a time $T_E/2$ after the 180-degree pulse, spins are in phase, forming the peak spin echo signal (i.e., Echo 1, 2, and N in Fig 2.4). MET_2 data is acquired by repeating 180-degree refocusing pulses every T_E numerous times (N times in Fig 2.4). This samples the signal, which decays exponentially with time constant T_2, from echo to echo (*See Eq.* 2.9). Each echo time provides a qualitative T_2-weighted image, described above. After N echoes are acquired, the remaining time in the defined T_R is elapsed allowing for T_1 recovery (*See Eq.* 2.9) before acquiring another train of echo signals.

Through non-negative least squares (NNLS) analysis (described below), we can fit MET_2 data to obtain a T_2 spectrum. In the central nervous system (CNS), *3* peaks are generally found in the spectrum of T_2 values. The T_2 peaks correspond to the hindrance of water motion; therefore, the shortest peak represents water trapped between myelin sheaths ($T_2 \sim$ 5-40ms, depending on B_0), the middle peak represents intra- and extra-axonal water ($T_2 \sim$ 30-80ms, depending on B_0), and cerebrospinal fluid ($T_2 >$ 1s) is the longest peak *in vivo*. The percentage of short T_2 signal is a quantitative measure of myelin water content, termed the Myelin Water Fraction (MWF) and correlates well with myelin content (22,23).

2.4.1.1 Non-negative Least Squares (NNLS) Analysis

Myelin water imaging (MWI) by MET_2 provides specific information about myelin content and microstructure in white matter (23,24). Equation 2.10 describes MET_2 decay signal from a spin echo experiment, where y is the acquired signal, M is the number of T_2 values to fit, typically 100

as to not bias results, N is the number of echoes acquired, and s is the spectral amplitude of each T_2 component. Typically, T_j is logarithmically-spaced and ranges from a few milliseconds to 500ms to encompass the range of expected relaxation times.

$$y_i = \sum_{j=1}^{M} s_j e^{-t_i/T_j}, \quad i = 1, 2, \dots, N \qquad [2.10]$$

This can be generalized into a linear system in equation 2.11,

$$y_i = \sum_{j=1}^{M} A_{ij} s_j, \quad i = 1, 2, \dots, N \qquad [2.11]$$

where A_{ij} represents a matrix describing exponential decay with N echoes at M possible T_2 relaxation times, respectively. Knowing y and defining A based on the current experimental conditions (number of acquired echoes and echo spacing (T_E)), the vector s can be determined by minimizing the least-squares misfit in equation 2.12.

$$\sum_{i=1}^{N} \sum_{j=1}^{M} \left(A_{ij} s_j - y_i\right)^2, \quad i = 1, 2, \dots, N \qquad [2.12]$$

Since noise in the measured data (y_i) is inherent, the misfit cannot be reduced to zero. The fitting can therefore be regularized based on some characteristic of the resulting spectrum in order to increase reproducibility in return for decreased resolution. For example, one can minimize the curvature of the spectrum, or the second order finite difference, as seen in equation 2.13.

$$\sum_{i=1}^{N} \sum_{j=1}^{M} \left(A_{ij} s_j - y_i\right)^2 + \mu \sum_{j=1}^{M-2} \left(s_{j+2} - 2s_{j+1} + s_j\right)^2, \quad i = 1, 2, \dots, N \qquad [2.13]$$

μ is generally chosen in order to smooth the T_2 spectrum so that the chi-squared statistic of the misfit is equal to about the number of data points, so each data point is misfit by one standard deviation. If it is smaller, the fit is too accurate and will fit the noise. If the chi-squared value is

much larger, the data will not be accurately fit. Smoothing provides a continuous and physically realistic model of the spectrum (22).

After the spectrum is found, the T_2 peaks and the fractional components of the area under those peaks can be determined by using the spectrum derivative. From this, MWF is determined as the fractional component of T_2 signal below a defined T_2 threshold based on typical T_2 characteristics (dependent on B_0) as seen in Fig 2.5 (23).

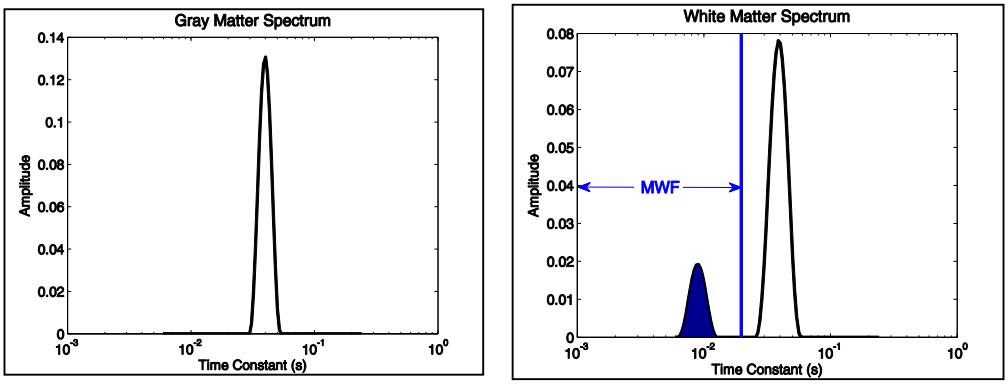

Figure 2.5. T_2 spectra from gray matter and white matter regions of interest. White matter has a short T_2 peak which corresponds to signal from myelin water (MWF).

2.4.1.2 Extended Phase Graph Algorithm

MET_2 is an important characterization of neurological tissue microstructure. However, accurate measurement of MET_2 using a standard multi-exponential NNLS fitting depends on pure exponential decay with an assumed perfect refocusing flip angle (B_1) of 180 degrees. Across a large volume, exponential decay is hampered by multiple coherence pathways arising from B_1 non-uniformity, resulting in stimulated echoes. Stimulated echoes arise from spins that see the original 90 degree excitation pulse and subsequent refocusing pulses less than 180 degrees. Instead of being refocused, the signal can be returned to the longitudinal axis where it does not experience transverse relaxation and a later refocusing pulse can return the spin back to the transverse plane. This increases signal at that echo time since these spins did not encounter true

T_2 relaxation as expected. This phenomenon can be seen beginning at the second echo time with increasing effects as refocusing flip angle decreases as seen in Fig 2.6. Using NNLS to fit decay curves that exhibit impure exponential behavior, results in improper curve fitting and biased T_2 values as seen in Fig 2.7 (25).

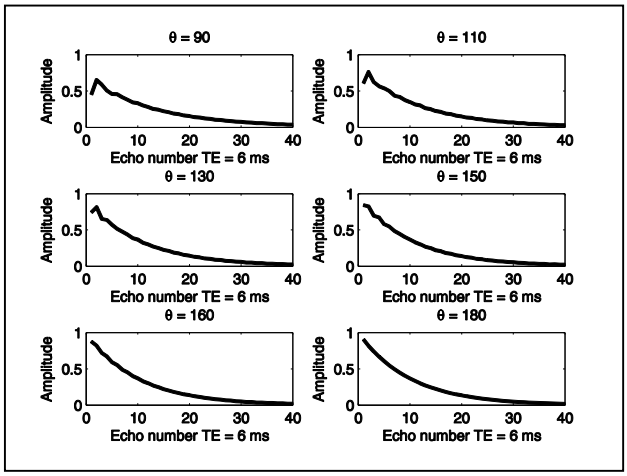

Figure 2.6. Example decay curves. Stimulated echoes contamination from non-uniform B1 on exponential decay curves. Non-negative least squares (NNLS) T_2 fitting techniques expect pure exponential decay.

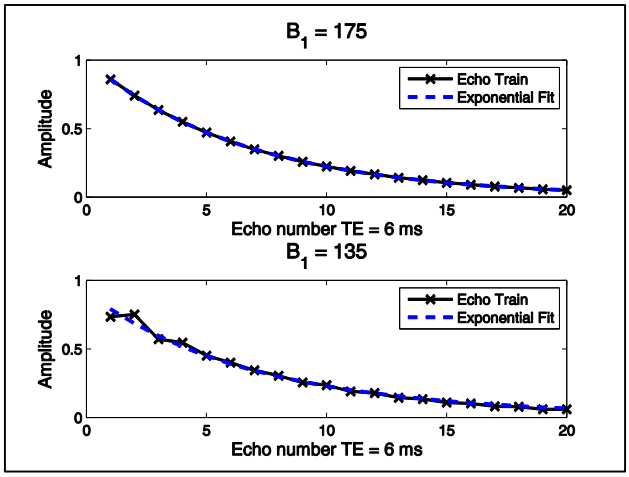

Figure 2.7. Exponential fitting of decay curves. Exponential fitting with a refocusing flip angle near perfect 175 degrees and 135 degrees. The stimulated echoes produced by the lower flip angle do not follow the exponential decay model.

One approach to avoid stimulated echo contamination is to use variable crusher gradients to remove the stimulated echo pathway. Here, each refocusing pulse has a unique pair of symmetric crusher gradients straddling the refocusing pulse with phase φ_n, where n = 1 to number of echoes. With this scheme, the spins in a stimulated echo pathway will accumulate phase φ_1 before being restored to the longitudinal axis. The phase is then rewound by $\varphi_2, \varphi_3 \ldots \varphi_N$ after returning to the transverse plane by a later refocusing pulse. Since $\varphi_1 \neq \varphi_{2,3,\ldots N}$, phase will not be cancelled and the signal will be incoherent. While this technique is effective, signal is inherently thrown away and the gradient strengths needed to crush all unwanted echoes in a linearly modulated crusher scheme, especially as B_1 decreases, become increasing large (26,27).

Another option to remove simulated echo contamination is to use composite refocusing pulses. These are a series of pulses with varied flip angles designed to produce a net 180-degree refocusing pulse that is minimally sensitive to inhomogenous B_o and B_1 fields (28,29). However, this technique also uses large crusher gradients to remove out-of-slice signal and has limited multi-slice capability. The pulse also greatly increases the specific absorption rate (SAR) as compared to other shaped pulses. Instead of avoiding stimulated echoes, recently, it has been shown that the Extended Phase Graph (EPG) algorithm (25) can be utilized to concurrently fit B_1 and multiple T_2s from an appropriate CPMG multiple spin echo measurement (30,31).

The EPG algorithm is an iterative method that tracks the phase and orientation of spins, known as the Magnetization Phase State Vector (*MPSV*) throughout a defined pulse sequence. Three phase states are identified: dephasing spins in the transverse plane (F), rephasing spins in the transverse plane (F^*), and spins along the longitudinal axis that maintain phase (Z). The *MPSV* contains the three phase states for each echo time period, giving a column vector 3 times the number of echoes in length, since the maximum number of dephasing states that a spin can

accrue is defined by the echo train length. The initial magnetization vector ($MPSV_o$), *Eq.* 2.14, describes the normalized magnetization in the transverse plane prior to relaxation (F_1).

$$MPSV_0 = [1\ 0\ 0\ 0\ \cdots]^T \quad [2.14]$$

Throughout the defined pulse sequence, a series of matrices are applied to the *MPSV* to describe changes to spin states. The rotation matrix (*R*), *Eq.* 2.15, defines the effect of an applied pulse (α) on spin vectors. The relaxation matrix (*E*), *Eq.* 2.16, defines the signal decay between refocusing pulses. The transition matrix (*T*) in *Eq.* 2.17 describes the change in phase state of magnetization vectors after a refocusing pulse, whether they continue in the dephasing state (*F*), enter the rephasing state (*F**), or maintain phase in the longitudinal axis (*Z*).

$$R: \begin{bmatrix} F_n \\ F_n^* \\ Z_n \end{bmatrix}^+ = \begin{bmatrix} \cos^2\left(\frac{\alpha}{2}\right) & \sin^2\left(\frac{\alpha}{2}\right) & -i\sin\alpha \\ \sin^2\left(\frac{\alpha}{2}\right) & \cos^2\left(\frac{\alpha}{2}\right) & i\sin\alpha \\ -\frac{1}{2}i\sin\alpha & \frac{1}{2}i\sin\alpha & \cos\alpha \end{bmatrix} \begin{bmatrix} F_n \\ F_n^* \\ Z_n \end{bmatrix} \quad [2.15]$$

$$E: \begin{bmatrix} F_1 \\ F_1^* \\ Z_1 \\ F_2 \\ F_2^* \\ Z_2 \\ F_3 \\ F_3^* \\ Z_3 \end{bmatrix}^+ = \begin{bmatrix} E_2 & 0 & 0 & 0 & 0 & 0 & 0 & 0 & 0 \\ 0 & E_2 & 0 & 0 & 0 & 0 & 0 & 0 & 0 \\ 0 & 0 & E_1 & 0 & 0 & 0 & 0 & 0 & 0 \\ 0 & 0 & 0 & E_2 & 0 & 0 & 0 & 0 & 0 \\ 0 & 0 & 0 & 0 & E_2 & 0 & 0 & 0 & 0 \\ 0 & 0 & 0 & 0 & 0 & E_1 & 0 & 0 & 0 \\ 0 & 0 & 0 & 0 & 0 & 0 & E_2 & 0 & 0 \\ 0 & 0 & 0 & 0 & 0 & 0 & 0 & E_2 & 0 \\ 0 & 0 & 0 & 0 & 0 & 0 & 0 & 0 & E_1 \end{bmatrix} \begin{bmatrix} F_1 \\ F_1^* \\ Z_1 \\ F_2 \\ F_2^* \\ Z_2 \\ F_3 \\ F_3^* \\ Z_3 \end{bmatrix} \quad \begin{aligned} E_1 &= exp\left(-\frac{TE}{2T_1}\right) \\ E_2 &= exp\left(-\frac{TE}{2T_2}\right) \end{aligned} \quad [2.16]$$

$$T: \begin{bmatrix} F_1 \\ F_1^* \\ Z_1 \\ F_2 \\ F_2^* \\ Z_2 \\ F_3 \\ F_3^* \\ Z_3 \end{bmatrix}^+ = \begin{bmatrix} 0 & 1 & 0 & 0 & 0 & 0 & 0 & 0 & 0 \\ 0 & 0 & 0 & 0 & 1 & 0 & 0 & 0 & 0 \\ 0 & 0 & 1 & 0 & 0 & 0 & 0 & 0 & 0 \\ 0 & 0 & 1 & 0 & 0 & 0 & 0 & 0 & 0 \\ 1 & 0 & 0 & 0 & 0 & 0 & 0 & 0 & 0 \\ 0 & 0 & 0 & 0 & 0 & 1 & 0 & 1 & 0 \\ 0 & 0 & 0 & 1 & 0 & 0 & 0 & 0 & 0 \\ 0 & 0 & 0 & 0 & 0 & 0 & 0 & 0 & 0 \\ 0 & 0 & 0 & 0 & 0 & 0 & 0 & 0 & 1 \end{bmatrix} \begin{bmatrix} F_1 \\ F_1^* \\ Z_1 \\ F_2 \\ F_2^* \\ Z_2 \\ F_3 \\ F_3^* \\ Z_3 \end{bmatrix} \quad [2.17]$$

The matrices are applied to the Magnetization Phase State Vector (*MPSV*) from right to left according to the pulse sequence, as described in *Eq.* 2.18, which begins as normalized transverse signal ($MPSV_0$) shown in *Eq.* 2.14. The signal created by the spin echo (M_n) is described by the signal in $MPSV_n(1)$ (*Eq.* 2.19). This describes the spins that were rephasing and have transitioned to the dephasing state, which necessitates a period of coherence and hence a spin echo.

$$MPSV_n = ETR(\alpha_n) \cdot E^2TR(\alpha_{n-1}) \cdots E^2TR(\alpha_1) \cdot E \cdot MPSV_0 \quad [2.18]$$

$$M_n = MPSV_n(1) \rightarrow Signal = F_1\,(1st\ in-phase\ state) \quad [2.19]$$

For voxel-by-voxel B_1 and T_2 fitting, the EPG algorithm first utilizes the described matrix multiplication to define a basis set of exponential curves based on the full range of T_2 values and a discrete number of refocusing flip angles ($N_\alpha \sim$ 5-10). The basis flip angles are linearly spaced for a range of expected α (i.e., 130-180 degrees), which are appropriate assumptions for B_1 in a 3D acquisition. The basis set is calculated prior to fitting any voxels to reduce computation time. A T_2 spectrum is fit via NNLS for each of the basis α and the sum-squared error between the experimental decay data and the fitted EPG-defined decay curves is calculated. This provides a coarse estimate of probable α that voxel experienced. Then, a fine spline interpolation (<0.5 degree spacing) is applied to the residuals to find the minimum corresponding to the precise α that voxel experienced. Once α is determined, basis decay curves are recalculated for the specific α and the T_2 spectrum is fit using NNLS as described previously. An example of the fitting can be seen in Fig 2.8 in comparison to pure exponential fitting in Fig 2.7. EPG estimation allows for 3D volumetric coverage without bias in fitted T_2 data due to non-uniform B_1 (30,31).

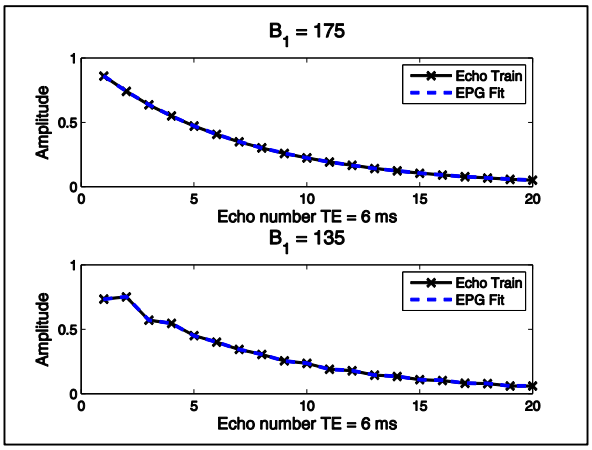

Figure 2.8. EPG fitting of decay curves. Exponential fitting based on the EPG Algorithm at near perfect 180 degree refocusing pulse and much lower (135 degrees). The EPG Algorithm accurately accounts for the stimulated echoes and properly fits the decay curve unlike exponential decay fitting in Fig 2.6.

2.4.1.3 Cramer-Rao Lower Bound (CRLB) Calculations

Given data measurements, y_i with noise, v_i, and g_i the estimated value of y_i based on model parameters (θ_j), the data can be described by equation 2.20

$$y_i = g(x_i, \theta_j) + v_i\,, \quad i = 1{:}N,\ j = 1{:}J \tag{2.20}$$

Where N is the number of data points and J is the number of model parameters, θ. The added noise (v_i) is a random variable drawn from the Gaussian-distributed probability density function (PDF) with an expected mean of 0 and variance of σ^2.

$$f(v_i) = \frac{1}{\sqrt{2\pi\sigma_i^2}} \exp\left(\frac{-{v_i}^2}{2\sigma_i^2}\right) \tag{2.21}$$

Then, y_i is also a random variable and can also be described a by a normally-distributed PDF

$$f(y_i) = \frac{1}{\sqrt{2\pi\sigma_i^2}} \exp\left(\frac{-(y_i - g(x_i,\theta_j))^2}{2\sigma_i^2}\right) \tag{2.22}$$

While the PDF describes the probability of certain outcomes as a function of model parameter values, the likelihood function describes the likelihood of model parameter values given observed outcomes. In other words, the likelihood function is considering the probability density function as a function of parameter space instead of the random variable y_i. Therefore, the likelihood function describes the most likely value of θ based on a distribution. If we assume the measurements are independent and the added noise follows a Gaussian distribution, then the likelihood function is described as

$$f(\theta_i; x, y) = \frac{1}{\sqrt{2\pi\sigma^2}} \exp\left(-\frac{1}{2}\sum_{i=1}^{N}\left(\frac{y_i - g_i(\theta)}{\sigma}\right)^2\right) \quad [2.23]$$

When the likelihood, or equivalent, log-likelihood function used for mathematical simplicity, is maximized, an optimal parameter estimator can be chosen by minimizing χ^2 defined in equation 2.24.

$$\chi^2 = \sum_{i=1}^{N}\left(\frac{y_i - g_i(x_i, \theta)}{\sigma_i}\right)^2 \quad [2.24]$$

To minimize χ^2, the function can be differentiated and set to zero to solve for optimal parameters. However, if we want to statistically evaluate the estimated parameters, one can consider the χ^2 function with respect to each parameter. The curvature of these functions inversely describes the uncertainty of the model parameter. Therefore, we can take the second order partial derivative of χ^2 with respect to each parameter to determine as shown in equations 2.25

$$\frac{\partial^2 \chi}{\partial \theta_j \partial \theta_k} = \frac{-2}{\sigma^2} \sum_{i=1}^{N} \left[\frac{-\partial g(x_i,\theta)}{\partial \theta_k} \frac{\partial g(x_i,\theta)}{\partial \theta_j} + (y_i - g(x_i,\theta)) \frac{\partial^2 g(x_i,\theta)}{\partial \theta_j \partial \theta_k} \right] \quad [2.25]$$

Since this the left hand term in eq. 2.25 is a random function, we need to consider its expected value. For an unbiased estimator, $E[y_i - g(x_i,\theta)] = 0$, therefore, the second term on the right had side equals zero and we are left with,

$$E\left[\frac{\partial^2 \chi}{\partial \theta_j \partial \theta_k}\right] = \frac{-2}{\sigma^2} \sum_{i=1}^{N} \left[\frac{-\partial g(x_i,\theta)}{\partial \theta_k} \frac{\partial g(x_i,\theta)}{\partial \theta_j} \right] = J^T J \quad [2.26]$$

where J is the Jacobian matrix which is an *N* x *N* matrix of partial derivative of *g* with respect to each fitted parameter, θ. The Fisher Information Matrix (FIM, F_{jk}) is then defined as the expected value of curvature matrix. Additionally, if we do not assume identically distributed noise, σ^2 is not constant for all *N* as shown in equation 2.27,

$$F_{jk} = \sum_{i=1}^{N} \frac{1}{{\sigma_{y_i}}^2} \frac{\partial g(x_i)}{\partial \theta_j} \frac{\partial g(x_i)}{\partial \theta_k} = J^T \Sigma_y^{-1} J \quad [2.27]$$

where *j* and *k =1:M*, the number of fitted parameters and Σ_y is the uncertainty of the observed data, an *N* x *N* matrix of variances and covariances. The FIM describes the amount of information that is known about each parameter based on the curvature of the χ^2 statistic of fit. The parameter covariance matrix (Σ_θ) is the inverse of the curvature, or Fisher information matrix, and the Cramer-Rao lower bound of variance for each parameter is defined as

$$\sigma_{\theta_j}^2 \geq [F^{-1}]_{jj} = \left[\left(J^T \Sigma_y^{-1} J \right)^{-1} \right]_{jj} \quad [2.28]$$

where θ_j is the estimated model parameter. The CRLB defines the maximum precision possible based on experimental conditions (32,33).

2.4.2 Magnetization Transfer

Magnetization transfer, first described by Wolff and Balaban (Wolff and Balaban, 1989), is a mechanism that describes the exchange of magnetization between the free water protons (^{1}H) and protons bound to macromolecules. To describe this exchange, a two-pool model is used as seen in Fig 2.9 below,

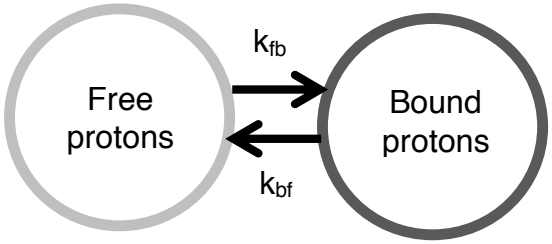

Figure 2.9. Two pool model of exchange. Free protons represent those water protons moving in space, whereas macromolecular protons are those attached and motionally restricted.

where k_{fb} is the first order rate constant of ^{1}H from the free to the bound, macromolecular pool and k_{bf} is rate constant in the opposite direction. This exchange occurs via dipolar interactions or chemical exchange when free ^{1}H are near macromolecular ^{1}H. As discussed above, myelin is a large component of white matter and mainly consists of ^{1}H bound to macromolecules; therefore, the magnetization transfer contrast is much greater in normal white matter than gray matter. However, other structures, like cell membranes, also contain bounded ^{1}H, so magnetization transfer contrast is not specific to myelin.

Since the motion of bound ^{1}H is restricted, these nuclei will be greatly influenced by their local magnetic field, causing a loss in phase coherence and a very short T_2 (< 1ms). Conversely, with freely moving ^{1}H, local field fluctuations average out leading to a much longer T_2 (> 10 ms). As T_2 is inversely related to spectral width, macromolecular protons exhibit a broad frequency spectrum, while free water protons have a narrow bandwidth centerd at Larmor frequency ($\Delta = \omega_o - \omega$) as seen below in Fig 2.10.

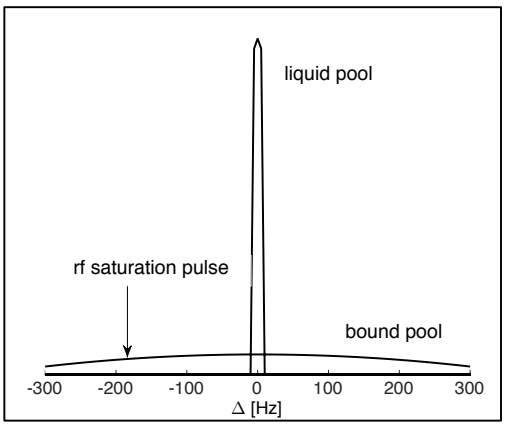

Figure 2.10. Frequency spectrum of bound protons and liquid, free protons.

The short T_2 of macromolecular ^{1}H prevents direct imaging with standard MRI sequences, but they can be investigated through the MT effect on the free water. By selectively affecting one of the proton pools, subsequent magnetization exchange between the two pools will alter the observed free water signal based on the amount of bound proton content. Since free water has a relatively narrow bandwidth, if an off-resonance pulse is applied prior to an imaging sequence, the macromolecular pool is partially saturated, while the free water pool remains mainly unaffected. The saturated magnetization will transfer energy to the free pool based on the rate of exchange between the two pools and the resulting image will have decreased signal. By

comparing this saturated image signal (M_{SAT}) to a typically acquired image signal (M_0), a Magnetization Transfer Ratio (*MTR*) can be calculated as,

$$MTR = \frac{M_0 - M_{SAT}}{M_0} \quad [2.26]$$

where *MTR* will be lowest in regions of high bound, macromolecular content. However, this ratio is only semi-quantitative and varies among scanners and protocol choices (34–36).

2.4.2.1 Quantitative Magnetization Transfer

Another option is to perform a quantitative Magnetization Transfer (qMT) experiment. Several methods have been developed (37–39) but in this work, the selective inversion recovery (SIR) technique described by Gochberg and Gore is used and described by the pulse sequence shown in Fig 2.11. This technique is based on a normal inversion recovery (IR) preparation followed by a Fast Spin Echo (FSE) readout; however the shortest inversion times (T_I) used are in the millisecond range, which is much shorter than typical IR sequences.

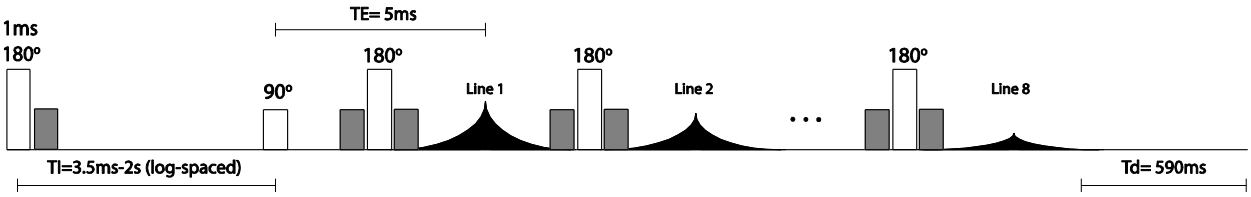

Figure 2.11. Selective Inversion Recovery pulse diagram. A 180-degree inversion pulse is followed by a Fast Spin Echo readout to acquire all lines of k-space.

The inversion pulse is much longer than the T_2 of bound ^{1}H but much shorter than the T_2 of free ^{1}H and utilizes a low power pulse to selectively invert the free water pool, while bound spins are

majorly unaffected. Magnetization transfer occurs between the two pools via dipolar cross-relaxation or chemical exchange and can be modeled by replacing $1/T_1$ in *Eq*. 2.7 with a matrix and adding a coupling term to the Bloch equations commonly known as the Bloch-McConnell equations (40–42) as seen below in *Eqs.* 2.27 and 2.28

$$\frac{dM_z}{dt} = \boldsymbol{L_1}(M_z(t) - \boldsymbol{M}_0) \quad [2.27]$$

$$\boldsymbol{L_1} = \begin{bmatrix} -(R_{1f} + k_{fb}) & k_{bf} \\ k_{fb} & -(R_{1b} + k_{bf}) \end{bmatrix} \quad [2.28]$$

where, as before, *f* and *b* represent the free and bound pools, respectively, the equilibrium magnetization in both pools is $\boldsymbol{M_0} = [M_{0f}\,;\, M_{0b}]$, R_1 is the longitudinal relaxation rate of each pool without MT, and M_z(t) is the longitudinal magnetization at time *t*. From these equations, it is clear that in the case of no exchange ($k = 0$) only the first term remains and relaxation is only dependent on one pool as in *Eq*. 2.7. To describe acquired M_z(t), *Eq*. 2.27 can be solved as before giving *Eq.* 2.29

$$M_z(t) = [M_z(0) - \boldsymbol{M_0}] \exp(-\boldsymbol{L_1}t) + \boldsymbol{M_0} \quad [2.29]$$

where $\boldsymbol{L_1}$ is the matrix in *Eq.* 2.28. While this describes inversion recovery data with full recovery ($T_R >> T_1$), here full recovery is not reached and there is a finite delay time (T_d) between the last echo and subsequent inversion pulse. However, at the end of signal acquisition, both pools (free and bound) have no longitudinal magnetization ($M_z = 0$). The free pool is saturated after a 90-degree pulse followed by a train of 180-degree pulses and the bound pool is drawn to the free pool via the MT effect. Therefore, the initial condition, $M_z(0) = M_z(t = T_d)$ is the solution of *Eq.* 2.29 with $t = 0$ after acquisition readout, so $M_z(t = 0) = 0$ as shown in *Eq* 2.30

$$M_z(T_d) = \boldsymbol{R}[\boldsymbol{M_0} - \boldsymbol{M_0}\exp(-\boldsymbol{L_1}T_d)] \quad [2.30]$$

In *Eq*. 2.30, $\boldsymbol{M_0}$ is dependent on the efficiency of the inversion pulse described by $\boldsymbol{R} = [S_f ; S_b]$ where S_f, and S_b describe the inversion and saturation effects of the inversion pulse on the free and bound pools, respectively. Based on mass balance between the two pools, $k_{fb}M_{0f} = k_{bf}M_{0b}$. Therefore, from *Eqs* 2.28 and 2.30, there are 7 unknowns: R_{1f}, R_{1b}, k_{mf}, M_{0f}, M_{0b}, S_f, and S_b. It has been shown in prior studies (37) that the fitting has little dependence on S_b and R_{1b}. S_b has been estimated based on a 1-ms hard inversion pulse, a bound pool with Gaussian linewidth, and bound T_2 = 10-20 μs, providing S_b = 0.83 (37). With little dependence on R_{1b}, we can set it equal to 1s for fitting. From this, the remaining 5 parameters are estimated and BPF = $\frac{M_{0b}}{M_{0f}+M_{0b}}$.

2.5 REFERENCES

1. Morell P, Quarles R, Norton W. Formation, structure, and biochemistry of myelin. In: 4th ed. New York: Raven Press Ltd; 1989. pp. 109–136.

2. Trapp BD, Kidd G. Structure of the myelinated axon. In: London: Elsevier Academic Press; 2004. pp. 3–27.

3. Van De Graff K. Nervous tissue and the central nervous system. In: New York: McGraw-Hill; 2002. p. 351.

4. Laule, Vavasour, Kolind, Li D. Magnetic resonance imaging of myelin. 2007.

5. Trapp BD, Ransohoff R, Rudick R. Axonal pathology in multiple sclerosis: relationship to neurologic disability. Current opinion in neurology 1999;12:295–302. doi: 10.1097/00019052-199906000-00008.

6. Simao G, Raybaud C, Chuang S, Go C, Snead O, Widjaja E. Diffusion Tensor Imaging of Commissural and Projection White Matter in Tuberous Sclerosis Complex and Correlation with Tuber Load. American Journal of Neuroradiology 2010;31:1273–77. doi: 10.3174/ajnr.A2033.

7. Carson R, Kelm N, West K, Does M, Fu C, Weaver G, McBrier E, Parker B, Grier M, Ess K. Hypomyelination following deletion of Tsc2 in oligodendrocyte precursors. Annals of Clinical Translational Neurology 2015;2:1041–54. doi: 10.1002/acn3.254.

8. Berthold C, Nilsson I, Rydmark M. Axon diameter and myelin sheath thickness in nerve fibres of the ventral spinal root of the seventh lumbar nerve of the adult and developing cat. Journal of anatomy 1983;136:483–508.

9. Nave K-AA, Trapp BD. Axon-glial signaling and the glial support of axon function. Annual review of neuroscience 2008;31:535–61. doi: 10.1146/annurev.neuro.30.051606.094309.

10. Fang X, Zhou X, Wang X. Clinical development of phosphatidylinositol 3-kinase inhibitors for non-Hodgkin lymphoma. Biomarker Research 2013;1:1–7.

11. Carson RP, Fu C, Winzenburger P, Ess KC. Deletion of Rictor in neural progenitor cells reveals contributions of mTORC2 signaling to tuberous sclerosis complex. Human Molecular Genetics 2013;22:140–52. doi: 10.1093/hmg/dds414.

12. Wahl SE, McLane LE, Bercury KK, Macklin WB, Wood TL. Mammalian target of rapamycin promotes oligodendrocyte differentiation, initiation and extent of CNS myelination. The Journal of neuroscience : the official journal of the Society for Neuroscience 2014;34:4453–65. doi: 10.1523/JNEUROSCI.4311-13.2014.

13. Bercury KK, Dai J, Sachs HH, Ahrendsen JT, Wood TL, Macklin WB. Conditional ablation of raptor or rictor has differential impact on oligodendrocyte differentiation and CNS myelination. The Journal of neuroscience : the official journal of the Society for Neuroscience 2014;34:4466–80. doi: 10.1523/JNEUROSCI.4314-13.2014.

14. Harrington EP, Zhao C, Fancy SP, Kaing S, Franklin RJ, Rowitch DH. Oligodendrocyte PTEN is required for myelin and axonal integrity, not remyelination. Annals of Neurology 2010;68:703–16. doi: 10.1002/ana.22090.

15. Brown RW, Cheng Y-CN, Haacke EM, Thompson MR, Venkatesan R. Magnetic Resonance Imaging: Physical Principles and Sequence Design. 2nd ed. New Jersey: John Wiley & Sons; 2014 p. 1008.

16. Neema M, Stankiewicz J, Arora A, et al. T1- and T2-Based MRI Measures of Diffuse Gray Matter and White Matter Damage in Patients with Multiple Sclerosis. Journal of Neuroimaging 2007;17:16S–21S. doi: 10.1111/j.1552-6569.2007.00131.x.

17. Stanisz G, Odrobina E, Pun J, Escaravage M, Graham S, Bronskill M, Henkelman R. T1, T2 relaxation and magnetization transfer in tissue at 3T. Magnetic Resonance in Medicine 2005;54:507–12. doi: 10.1002/mrm.20605.

18. Alexander AL, Lee JE, Lazar M, Field AS. Diffusion tensor imaging of the brain. Neurotherapeutics 2007;4:316–29. doi: 10.1016/j.nurt.2007.05.011.

19. Goldberg-Zimring D, Mewes AU, Maddah M, Warfield SK. Diffusion tensor magnetic resonance imaging in multiple sclerosis. Journal of neuroimaging 2005;15:68S–81S. doi:

10.1177/1051228405283363.

20. Meiboom S, Gill D. Modified Spin-Echo Method for Measuring Nuclear Relaxation Times. Review of Scientific Instruments 1958;29:688. doi: 10.1063/1.1716296.

21. Hahn E. Spin Echoes. Physical Review 1950;80:580–94.

22. Whittall K, MacKay A. Quantitative interpretation of NMR relaxation data. Journal of Magnetic Resonance 1989;84:134–52. doi: 10.1016/0022-2364(89)90011-5.

23. Mackay A, Whittall K, Adler J, Li D. In vivo visualization of myelin water in brain by magnetic resonance. Magnetic Resonance in Medicine 1994;31:673–7. doi: 10.1002/mrm.1910310614.

24. Laule, Leung, Lis D, Traboulsee, Paty, MacKay, Moore G. Myelin water imaging in multiple sclerosis: quantitative correlations with histopathology. Multiple sclerosis (Houndmills, Basingstoke, England) 2006;12:747–53. doi: 10.1177/1352458506070928.

25. Hennig J. Echoes—how to generate, recognize, use or avoid them in MR-imaging sequences. Part II: Echoes in imaging sequences. Concepts in Magnetic Resonance 1991;3:179–92. doi: 10.1002/cmr.1820030402.

26. Crawley, Henkelman. Errors in T2 estimation using multislice multiple-echo imaging. Magnetic Resonance in Medicine 1987;4:34–47. doi: 10.1002/mrm.1910040105.

27. Does M, Gore J. Complications of nonlinear echo time spacing for measurement of T2. NMR in Biomedicine 2000;13:1–7. doi: 10.1002/(SICI)1099-1492(200002)13:1<1::AID-NBM603>3.0.CO;2-E.

28. Poon C, Henkelman R. Practical T2 quantitation for clinical applications. J Magn Reson Im 1992;2:541–53. doi: 10.1002/jmri.1880020512.

29. Whittall K, Mackay A, Graeb D, Nugent R, Li DK, Paty D. In vivo measurement of T2 distributions and water contents in normal human brain. Magnetic Resonance in Medicine 1997;37:34–43. doi: 10.1002/mrm.1910370107.

30. Lebel MR, Wilman AH. Transverse relaxometry with stimulated echo compensation. Magnetic Resonance in Medicine 2010;64:1005–14. doi: 10.1002/mrm.22487.

31. Prasloski T, Mädler B, Xiang Q. Applications of stimulated echo correction to multicomponent T2 analysis. Magnetic Resonance in Medicine 2012;67:1803–14. doi: 10.1002/mrm.23157.

32. Kay S. Fundamentals of Statistical Signal Processing: Estimation Theory . Prentice Hall; 1993.

33. Van Trees H. Detection, Estimation, and Modulation Theory, Part 1. New York: Wiley; 1968.

34. Henkelman R, Stanisz G, Graham S. Magnetization transfer in MRI: a review. NMR in Biomedicine 2001;14:57–64. doi: 10.1002/nbm.683.

35. Henkelman MR, Huang X, Xiang Q, Stanisz G, Swanson SD, Bronskill MJ. Quantitative interpretation of magnetization transfer. Magnetic Resonance in Medicine 1993;29:759–66. doi: 10.1002/mrm.1910290607.

36. Horsfield MA, Barker GJ, Barkhof F, Miller DH, Thompson AJ, Filippi M. Guidelines for using quantitative magnetization transfer magnetic resonance imaging for monitoring treatment of multiple sclerosis. Journal of Magnetic Resonance Imaging 2003;17:389–97. doi: 10.1002/jmri.10266.

37. Gochberg DF, Gore JC. Quantitative magnetization transfer imaging via selective inversion recovery with short repetition times. Magnetic Resonance in Medicine 2007;57:437–41. doi: 10.1002/mrm.21143.

38. Sled JG, Pike BG. Quantitative imaging of magnetization transfer exchange and relaxation properties in vivo using MRI. Magnetic Resonance in Medicine 2001;46:923–31. doi: 10.1002/mrm.1278.

39. Yarnykh VL, Yuan C. Cross-relaxation imaging reveals detailed anatomy of white matter fiber tracts in the human brain. NeuroImage 2004;23:409–24. doi: 10.1016/j.neuroimage.2004.04.029.

40. Li K, Zu Z, Xu J, Janve V, Gore J, Does M, Gochberg D. Optimized inversion recovery sequences for quantitative T1 and magnetization transfer imaging. Magnetic Resonance in Medicine 2010;64:491–500. doi: 10.1002/mrm.22440.

41. Dortch, Horch, Does. Development, simulation, and validation of NMR relaxation-based exchange measurements. The Journal of Chemical Physics 2009;131:164502. doi: 10.1063/1.3245866.

42. McConnell H. Reaction Rates by Nuclear Magnetic Resonance. J Chem Phys 1958;28:430. doi: 10.1063/1.1744152.

CHAPTER 3

MULTI-EXPONENTIAL T_2 MYELIN WATER IMAGING IN EX-VIVO RODENT BRAIN

3.1 INTRODUCTION

Magnetic Resonance Imaging (MRI) offers the ability to non-destructively evaluate normal and diseased white matter across whole rodent brain. Through conventional MRI measures, image contrast has been shown to be sensitive to various white matter pathologies, such as demyelination (1–3), axonal damage (4–6), and edema (7,8); however, these approaches generally lack specificity. In order to relate changes in MRI contrast to specific changes in white matter microstructure, more advanced quantitative techniques have been developed. In particular, multi-exponential analysis of transverse relaxation (MET_2) offers a relatively specific approach to myelin water imaging (MWI).

MET_2 analysis of the water proton magnetic resonance signal from white matter provides a T_2 spectrum which is typically comprised of two signal components. The faster-relaxing signal component has been shown to primarily result from the water that is trapped between the lipid bilayers which comprise myelin (9,10), while the slower-relaxing component is primarily derived from the remainder of the water in both intra- and extra-axonal spaces. The myelin water fraction (MWF) is defined as the fraction of fast-relaxing component compared to the total water signal. Despite that this approach was first demonstrated in humans two decades ago (11), there is a paucity of reports of MWI in small animals. Gareau et al. demonstrated MWI in guinea pig brain (12), and a few papers have presented MWI in rat spinal cord (13–15), but to our knowledge MWI by MET_2 analysis has not been effectively applied in rat or mouse brain. Does

and Gore used MET_2 analysis in studies of rat brain *in vivo* but did not find a reproducible myelin water signal from cerebral white matter, which was attributed to limitations of spatial resolution and signal-to-noise ratio (SNR) (16).

If resolution and SNR are the limiting factors, then using higher static magnetic field strengths (B_0) and imaging excised and chemically fixed brains, which permits long scan times, may provide the necessary resolution and SNR for effective MWI in rodent brains *ex vivo*. The SNR efficiency when imaging excised tissues can also be increased by loading the tissue with paramagnetic contrast agent to reduce longitudinal relaxation time (T_1) (17–19). However, both increased B_0 and use of paramagnetic agents will reduce T_2, making the MET_2 analysis more difficult, statistically, and so the benefit of either of these approaches for MWI is unclear.

In addition to SNR limitations, conventional multiple spin echo imaging necessary for MET_2 analysis assumes near perfect B_1 refocusing and gradient spoiling of stimulated echoes (20), which limits coverage of multi-slice or 3D acquisitions to highly uniform regions of the transmit radiofrequency (RF) coil. The extended phase graph (EPG) algorithm (21) can be used to account for B_1^+ variation in T_2 measurements (22,23), thereby alleviating this restriction. In short, the algorithm fits the effective refocusing pulse flip angle along with T_2, making T_2 estimates roughly independent of B_1^+.

Presented here is an evaluation of MWI at high and ultra-high field in rodent brain. We first determine the effect of gadolinium (Gd), (in the form of Gd-DTPA) on T_1 and T_2, of rat cerebral white matter at B_0 = 7 T and 15.2 T. Next, we consider the influence of choice of regularization technique for fitting MET_2 data. Then, we assess the benefits of higher field strengths and/or the addition of Gd. Then, we evaluate the reproducibility of MWF across animals and across

different concentrations of Gd loading. Finally, we evaluate the impact of scan parameters, namely echo time and receiver bandwidth, on MWF.

3.2 MATERIALS AND METHODS

3.2.1 Tissue Preparation

Animal studies were approved by the Vanderbilt University Institutional Animal Care and Use Committee. Twelve adult female Sprague-Dawley rats were anesthetized with isoflurane and sacrificed via transcardial perfusion. The perfusion consisted of 1X phosphate-buffered saline (PBS) wash followed by 2.5% glutaraldehyde + 2% paraformaldehyde (modified Karnovsky solution). Following perfusion, brains were quickly removed from skull and immersed in the fixative solution for 1 week. Brains were then washed with 1X PBS + 0.01% sodium azide, changing wash 4-5 times over 1 week to remove excess fixative. In seven of eleven cases, Gd-DTPA (Magnevist; Berlex, Montville, NJ) at concentrations of 0.25 mM (2), 0.5 mM (3), or 1.0 mM (2) were included in the perfusate, immersion and wash solutions. The time course of fixation and loading tissues with Gd-DTPA was not optimized, but was consistent with previous studies (18,19) and no obvious signs of non-uniform Gd distribution were observed. Studies on larger brains may require longer preparation periods to achieve a uniform distribution of Gd.

3.2.2 Magnetic Resonance Imaging

Imaging was performed on two systems: i) a 7-T 16-cm horizontal bore Agilent/Varian (Santa Clara, CA) DirectDrive scanner, using a 38-mm diameter Litz quadrature coil (Doty Scientific, Columbia, SC) for transmission and reception, and ii) a 15.2-T 11-cm horizontal bore Bruker

(Rheinstetten, Germany) BioSpec scanner, using a 35-mm diameter Bruker quadrature volume coil for transmission and reception.

First, longitudinal and transverse relaxation times (T_1 and T_2) were measured in one brain with 0.5 mM and one brain without Gd at both 7 T and 15.2 T. For these measurements, low-resolution imaging allowed relatively rapid scans with high SNR, minimal echo spacing, and long repetition times (T_R). T_1 was measured using a slice-selective fast spin echo sequence with minimum echo time (T_E) and 8 logarithmically-spaced T_R values ranging from minimum T_R to >3× the expected T_1. Slice thickness and in-plane voxel dimensions were each 500 μm. T_2 was measured using a 3D multiple spin-echo sequence with non-selective excitation and refocusing pulses, 160 μs and 100 μs in duration, respectively. Each refocusing pulse was surrounded by 428 μs duration 6 G/cm amplitude crusher gradients, phase-encoding gradients were rewound after each echo, and a two-part (+X/-X) phase cycling scheme was used. With these constraints, secondary echoes that were not excited by the initial excitation pulse were removed, and the observed echo magnitudes could be computed with the extended phase graph (EPG) algorithm (Hennig, 1991). Sampling of transverse signal decay was achieved with T_E = 3.75 ms, number of echoes (N_E) = 60, and receiver bandwidth (BW) = 50 kHz. Repetition times were set to be ≈ 3 × T_1 for each case. Images were encoded in a 64 × 64 × 64 matrix over a 3.2 × 3.2 × 3.2 cm^3 field of view (FOV) resulting in 500 μm isotropic resolution.

Based on analysis of these low resolution scans, high resolution (250 μm isotropic resolution) 3D multiple spin echo imaging was implemented in three brains without Gd and in three brains loaded with Gd = 0.25 mM, 0.5 mM, and 1.0 mM, respectively. In each case, scan parameters were predicted to be optimal for MWF estimation (see 2.3 *Data Analysis)* for a 4-hr scan time as seen in Table 3.1. These scans were encoded with a matrix size of 128 × 64 × 64

over a 3.2 × 1.6 × 1.6 cm^3 FOV. High-resolution data were zero-padded to 256 × 128 × 128 resulting in images reconstructed to 125 μm isotropic resolution.

Table 3.1. Scan Parameters used at 7T and 15.2T Parameters were found based on predicted maximum MWF SNR (See *3.2.3 Data Analysis*) for a 4-hr scan duration and defined concentration of Gadolinium ([Gd]). Optimal repetition times (T_R), echo times (T_E), number of echoes (N_E), number of excitations (N_{EX}), and receiver bandwidths (BW) are shown.

	[Gd] (mM)	T_R (s)	T_E (ms)	N_E	N_{EX}	BW (kHz)
7T						
	0	1.76	7.2	37	2	29.76
	0.25	0.88	8.6	24	4	20.98
	0.5	0.88	9.1	24	4	19.39
	1.0	0.59	11.5	15	6	14.22
15.2T						
	0	1.76	5.5	36	2	42.61
	0.25	0.88	6.4	26	4	32.89
	0.5	0.88	6.9	24	4	29.09
	1.0	0.59	8.6	16	6	20.98

To assess sensitivity of MWF to T_E, we also acquired 2D MET_2 data from an EPG-compatible sagittal single slice acquisition. To maintain the same refocusing pulse through the slice, the 180-degree hermite pulse bandwidth was 3.75X the 90-degree Gaussian pulse

bandwidth. At both 7T and 15.2T, we acquired 6 scans at 6 different T_E equally space between 4.5/4.94ms and 15/18ms at 7/15.2T with minimum receiver bandwidth per T_E. For each scan, T_E * $N_E = 3.9*T_{2,IE}$, T_R provided 82% signal recovery, and NEX = max multiple of 2 for scan time ~ 20 minutes. This was performed in four brains loaded with Gd = 0, 0.25 mM, 0.5 mM, and 1.0 mM resulting in 36 MET_2 scans per brain per field strength. Scans were encoded with a matrix size of 128 × 64 over a 3.2 × 1.6 cm^2 FOV with 0.75mm slice thickness. High-resolution data were zero-padded to 256 × 128 resulting in images reconstructed to 125 μm in-plane resolution.

3.2.3 Data Analysis

All data analysis was performed using MATLAB R2013b (The Mathworks, Natick MA) and MET_2 analyses were performed using the freely available Multi Exponential Relaxation Analysis (MERA) toolbox (http://www.vuiis.vanderbilt.edu/~doesmd/MERA/MERA_Toolbox.html). Prior to Fourier reconstruction, k-space data for all images were apodized using a 2D or 3D Tukey window with a 0.25 taper-to-window ratio. The low-resolution variable-T_R image magnitudes from a region of interest comprising the corpus callosum were fitted to a 3-parameter mono-exponential function to estimate T_1, with and without contrast agent. The longitudinal relaxivity of Gd was then computed as $r_1 = (1/T_{1Gd}-1/T_{1noGd})/0.5mM$ and assumed to be the same for all white matter water.

For MET_2 analysis of the low-resolution images, the N_E echo magnitudes from each image voxel were fitted to a linear combination of signals described by 2 gaussian-shaped components in the log-T_2 domain and a refocusing pulse flip angle (θ), as outlined in Appendix A. Thus, for each voxel, five independent parameters were fitted: $\theta, f_S, T_{2S}, f_L, T_{2L}$, where subscripts S and L

indicate the short-lived and long-lived components, respectively. In cases where T_{2S} fell within a certain domain, $T_{2myelin,min} \leq T_{2S} \leq T_{2myelin,max}$, this signal component was defined as a myelin water signal, with signal fraction and T_2 defined as f_M and T_{2M}, respectively. Similarly, f_{IE} and T_{2IE} were defined for intra- and extra-axonal spaces from signals components with $T_{2IE,min} \leq T_{2L} \leq T_{2IE,max}$. Defining myelin and intra-/extra-axonal water signals this way automatically excluded spurious 2nd components when the signal was effectively mono-exponential, without having to do both one- and two-component fits. Domain boundaries ($T_{2M/IE,min/max}$) were determined from representative measured spectra—see 3. *Results*. Finally, transverse relaxivity was computed as $r_2 = (1/T_{2LGd}\text{-}1/T_{2LnoGd})/0.5$ mM. In principle, one could measure relaxivity of the short- and long-T_2 signals independently, but the precision of T_2 estimates for the long-T_2 component is much greater than that of the short T_2 (24,25) and a previous study suggests that loading the tissue with Gd affects both components approximately equally (26). Consequently, the same r_2 value was used for both short- and long-T_2 signals.

Given these relaxation and relaxivity measures, a predictive two-component signal model for multiple spin echo measurements was defined as

$$S_n = \left[f_M \exp\left(-nT_E \left(\frac{1}{T_{2M,\,noGd}} + r_2 C_{Gd} \right) \right) + f_{IE} \exp\left(-nT_E \left(\frac{1}{T_{2IE,\,noGd}} + r_2 C_{Gd} \right) \right) \right] \times \left[1 - \exp\left(-\left(T_R - N_E \times T_E \right) \left(\frac{1}{T_{1,\,noGd}} + r_1 C_{Gd} \right) \right) \right], \quad [3.1]$$

where n indicates echo number, C_{Gd} is the concentration of Gd in the tissue preparation solutions, and all other terms are as previously defined. With this signal model and the known relationship between image noise variance and receiver bandwidth, the Cramér-Rao lower bounds (CRLB) of

variance of f_M were formulated as a function of T_E, N_E, T_R, C_{Gd}, image matrix size, number of averaged excitations (N_{EX}), and total scan time (T_{scan}). Details of this relationship are omitted here, but follow a similar prior analysis (25) with the addition of a T_R and C_{Gd} to the signal equation. Using CRLB calculations, optimal values (for minimum coefficient of variation of f_M) of T_E, N_E, and T_R were computed assuming a 128 × 64 × 64 acquisition matrix, N_{EX} equal to a multiple of 2 (to provide averaging and the add/subtract phase-cycle), and a range of total scan times and C_{Gd} values. From these CRLB calculations, the predicted myelin water SNR was defined as f_M/σ_M, where σ_M is the square root of the CRLB of variance of f_M, and myelin water SNR efficiency was defined as $f_M/\sigma_M/\sqrt{T_{scan}}$, where T_{scan} is the total scan duration.

Since there is no standard for T_2-spectral fitting, the MET_2 analysis of high-resolution multiple spin echo data were fit using 4 different methods to explore options. T_2 spectra were estimated using the multiple-gauss fitting along with three variations of a conventional linear inverse approach (27). Compared to low-resolution data, there was one key difference in the multiple-gauss fitting. As some previous literature has found that 3 T_2 components may be necessary to describe transverse relaxation in white matter (28,29), multiple-gauss fitting was implemented with 3 components, although spectral analysis reduced the results to five independent parameters, ($\theta, f_M, T_{2M}, f_{IE}, T_{2IE}$), as described above. Again, this permitted identical analysis of all voxels did not require repeated fitting with varied number of components. For comparison, one brain was also analyzed using only 2-gaussian components. For the three linear inverse methods, data were fit by non-negative least-squares (NNLS; (30)) to the sum of signals from 100 logarithmically spaced T_2 components, as defined by the EPG algorithm and spanning $T_E/2$ to 500 ms in the T_2 domain, similar to previous work (23). In two variations the spectra were regularized using a minimum curvature constraint with either regularization adjusted for

each voxel via the generalized cross validation (GCV) method (31) or a conservative regularization held constant across all voxels. In the third variation, the spectra were not regularized.

3.3 RESULTS

From the low resolution scans, Fig 3.1 shows the voxels exhibiting ≥ 5% f_M and the average of their T_2 spectra, with and without Gd, and at both 7 T and 15.2 T. The corresponding measured T_{2M} and T_{2IE} values are shown in Table 3.2 and are generally consistent with literature (18,26,32,33) although there are no directly comparable studies. Likewise, the measured relaxivities, both r_1 and r_2 (measured from the long-T_2 signals) are consistent with previous literature in value and dependence on B_0 (18,34). It is also apparent from Table 3.2 that transverse relaxivity measured from the myelin water component did not yield expected results, with values of ≈ 120 s^{-1}/mM at 7 T but close to 66 s^{-1}/mM at 15.2 T, thereby supporting the use of long-T_2 signals only to estimate r_2.

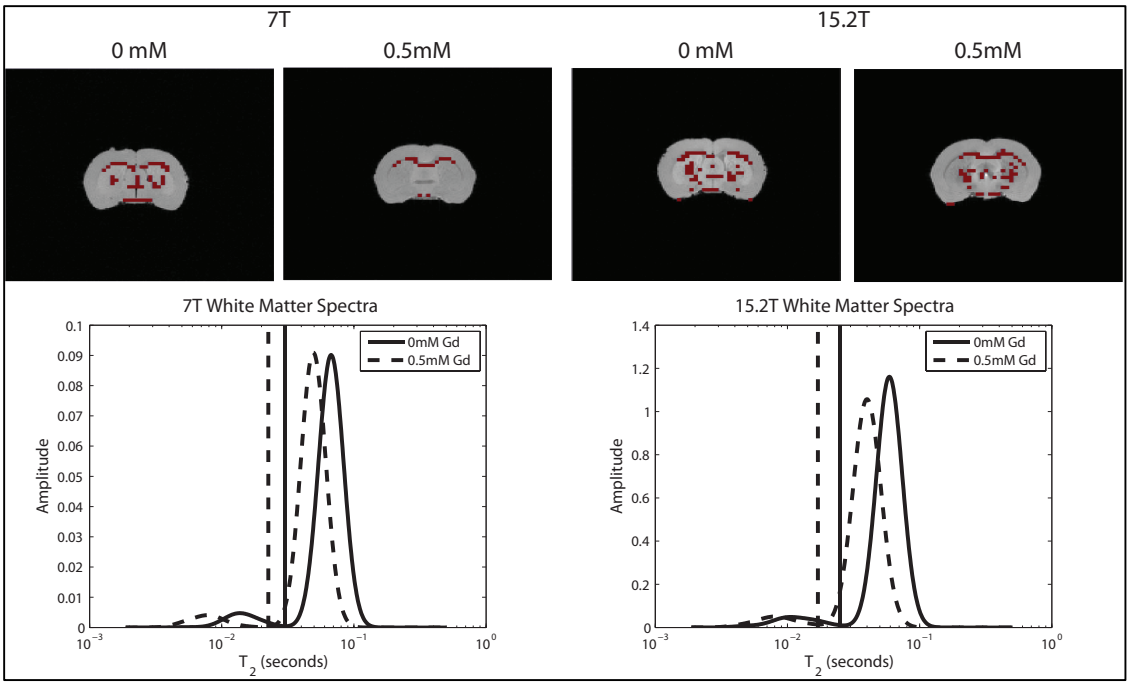

Figure 3.1. Mean T_2 spectra (left) of voxels with >5% Myelin Water Fraction (f_M) (right). At 7T and 15.2T doping with Gadolinium (Gd) (dashed) lowers T_2 as compared to undoped tissue (solid) as expected. Myelin water cutoff values were found from the T_2 with the lowest amplitude between the T_{2M} and T_{2IE} peaks.

Table 3.2. Longitudinal and transverse relaxation times (T_1 & T_2) and corresponding relaxivity values (r_1 & r_2). Two-component T_1 and T_2 peaks and relaxivity measures were found as explained in Data Analysis at 7T and 15.2T for brains loaded with 0mM and 0.5mM of Gadolinium (C_{Gd}) from voxels with >5% myelin water fraction (f_M) (see Fig 3.1).

	C_{Gd} (mM)					
	0		0.5			
	T_1 (ms)	T_2 (ms)	T_1 (ms)	T_2 (ms)	r_1 (s^{-1}/mM)	r_2 (s^{-1}/mM)
7 T						
Myelin Water		13.8 ± 0.5		7.55 ± 0.5		
I/E Water	998 ± 11	67.0 ± 0.6	389 ± 5	49.2 ± 0.7	3.13 ± 0.03	10.78 ± 0.68
15.2 T						
Myelin Water		10.7 ± 0.6		7.9 ± 0.4		
I/E Water	1498 ± 27	59.3 ± 0.8	482 ± 4	40.3 ± 0.8	2.81 ± 0.02	15.96 ± 0.51

Fig 3.2 shows a plot of predicted MWF SNR efficiency for high resolution imaging as a function of C_{Gd} at both 7 T and 15.2 T. The results predict that both increasing B_0 and loading tissue with Gd offer some advantage for MET_2 analysis in excised and fixed rat brain. CRLB calculations predict maximum SNR efficiency at $C_{Gd} = 0.2$ and 0.3 mM at 7 T and 15.2 T, respectively, with a net benefit compared to no Gd up to $C_{Gd} \approx 0.5$-0.75 mM. While obtaining highest possible SNR is desirable, scan duration may be the limiting factor. Therefore, as shown before, Table 3.1 displays scan parameters required to obtain maximal predicted f_M SNR given a 4hr scantime and C_{Gd} = 0, 0.25, 0.5, and 1.0mM. A less intuitive observation from Table 3.1 is that optimal T_E increases with increasing C_{Gd}—one might expect the opposite, since T_2s are reduced. However, as the ratio of long- to short-T_2 values becomes smaller (i.e., the two signal components are relaxing at a more similar rate) it is predicted from simulation and CRLB calculations that increased SNR to separate them in fitting, obtained through the lower receiver bandwidth afforded by the increased T_E is beneficial (25).

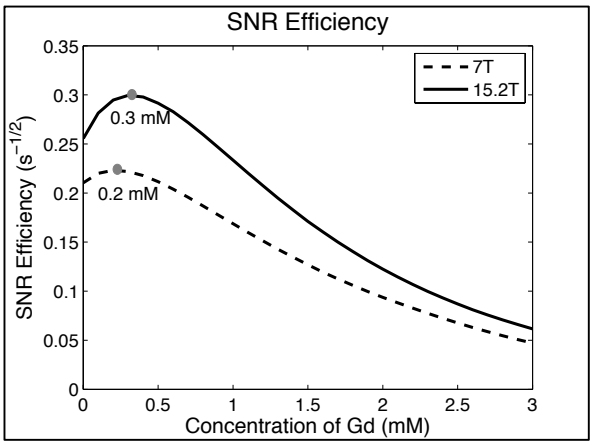

Figure 3.2. Myelin Water Fraction SNR Efficiency versus concentration of Gd (C_{Gd}) doping at 7T and 15.2T. Curves are based on relaxivity measures (see Table 3.2) and Cramér-Rao lower bounds (CRLB) of variance calculations of myelin water fraction (f_M). For each C_{Gd}, the maximum SNR efficiency is found for any scan duration.

The comparison of different MET_2 analysis methods is presented in Figs 3.3 – 3.5. Fig 3.3 shows f_M maps derived from (left) 2- and (right) 3-gaussian component fitting as well as corresponding example spectra from a voxel in the internal capsules. The f_M maps are similar or identical for most of the voxels in the corpus callosum and external capsules, but show noticeably greater f_M values in the internal capsules and much of the sub-cortical gray matter. The cause of this effect is apparent from the spectra. The 3-component spectrum shows a typical myelin water signal ($T_2 \approx 10$ ms), an intermediate T_2 component ($T_2 \approx 40$ ms) and a small longer-lived component ($T_2 \approx 100$ ms). Fitting this same signal with only two components results in the shorter-lived component capturing both myelin water and some intermediate T_2 signals. For voxels adequately described by two components, all fitted components with T_2 in the aforementioned myelin T_2 domain were summed to define the myelin water signal. The only cost to using 3-component fitting was computation time, but fitting every voxel with three components was still much faster than fitting each voxel separately with 1-, 2-, and 3-components then using a statistical test to select the most appropriate fit.

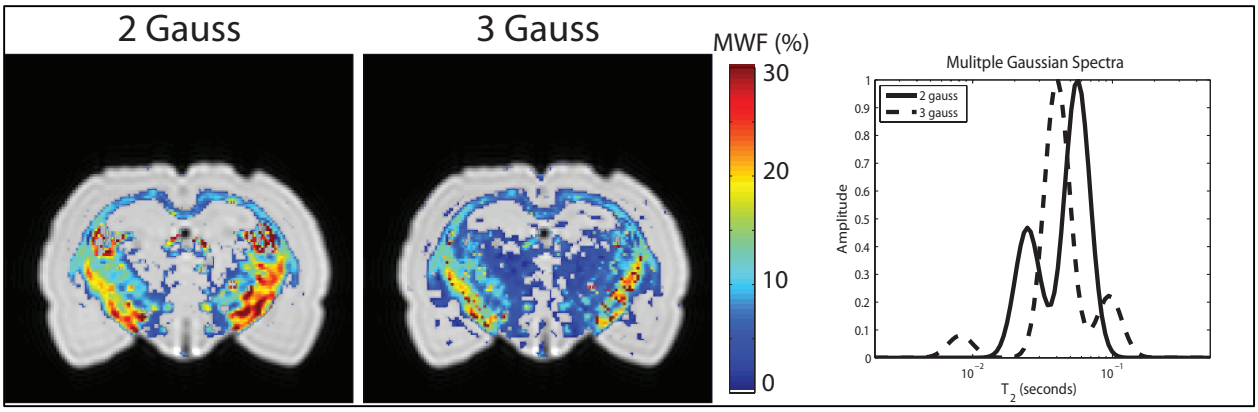

Figure 3.3. 2-Gaussian versus 3-Gaussian component fitting. Increasing the number of Gaussian components on the log-T_2 domain to 3, greatly reduced f_M in the internal capsules and voxels near borders. The difference in the two spectra from a representative voxel (right) displays the decrease in f_M as the error of the fit decreased.

Of course, the need to define any number of components can be effectively removed by using a conventional linear inverse approach (27). Fig 3.4 shows representative f_M maps derived from the multiple gauss fitting and three linear inverse approaches with different spectral regularizations (GCV-adjusted minimum curvature, constant minimum curvature, or unregularized). Qualitatively, all four maps are similar, so one could argue that any one of these approaches is reasonable. The map from unregularized spectra, in particular, shows greater f_M values, while the multiple gauss fitting produced the smoothest maps. Fig 3.5 quantitatively displays f_M and standard deviation from an ROI of the corpus callosum from each brain in Fig 3.4. Generally, we see expected results, with an increase in f_M and standard deviation from multiple gaussian fitting to unregularized fitting at both 7T and 15.2T. Additionally, we see similar results from C_{Gd} = 0 and 0.5mM at each field strength. The average root mean square error across the different analysis methods were all <0.25% of maximum signal amplitude. With no gold-standard, absolute accuracy of the different fitting methods cannot be evaluated, so spatially-invariant minimum curvature spectral regularization was used for all subsequent MET_2 analysis because it was relatively fast and yielded similar results to other regularized spectral methods.

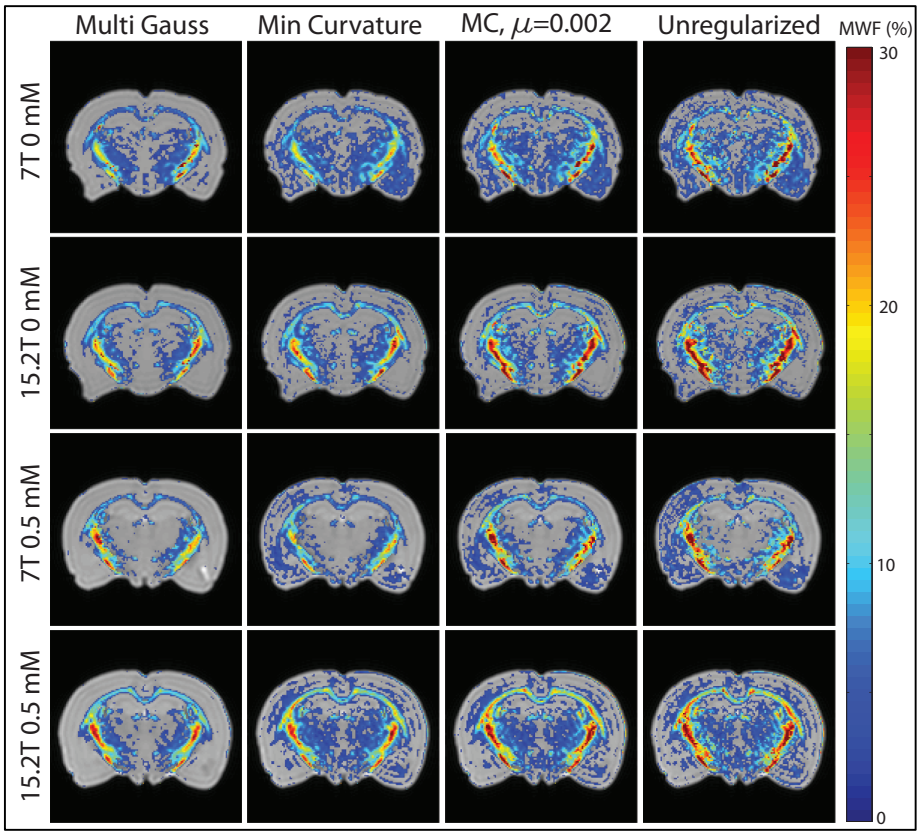

Figure 3.4. Myelin Water Fraction (f_M) maps at 7T and 15.2T doped with 0 and 0.5mM Gd and analyzed using 4 different MET_2 data fitting techniques. MET_2 data was collected using optimal scan parameters (see *2. Materials and Methods*) at 7T (top) and 15.2T (bottom). f_M was deemed as the fraction of signal with a peak $T_2 < T_{2M}$ (see Fig 3.1) after MET_2 analysis based on four techniques: i) three Gaussian-components in the log-T_2 domain ii) Non-Negative Least Squares (NNLS) regularized with a minimizing curvature constraint with regularizing parameter adjusted for each voxel by generalized cross-validation, iii) NNLS regularized with a constant regularizing parameter for all voxels, and iv) NNLS without regularization.

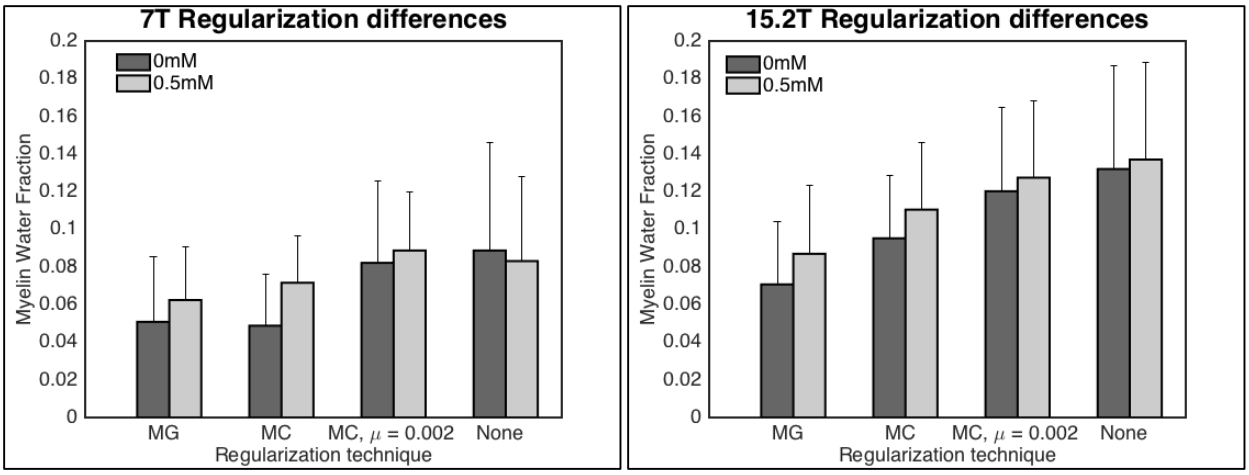

Figure 3.5. Myelin Water Fraction (f_M) differences from choice of MET_2 analysis at 7T and 15.2T with 0 and 0.5mM Gd. f_M and standard deviation at (left) 7T and (right) 15.2T from MET_2 analysis based on four techniques: i) three Gaussian-components in the log-T_2 domain ii) Non-Negative Least Squares (NNLS) regularized with a minimizing curvature constraint with regularizing parameter adjusted for each voxel by generalized cross-validation, iii) NNLS regularized with a constant regularizing parameter for all voxels, and iv) NNLS without regularization with (dark gray) 0mM and (light gray) 0.5mM Gd.

High resolution f_M maps obtained using the predicted optimal 4-hour scan protocols for the case of C_{Gd} = 0 and 0.5 mM (See *2.2 Magnetic Resonance Imaging* and Table 3.1), and at both 7 T and 15.2 T, are shown in Fig 3.6. Across scan protocols (with and without Gd at both field strengths), f_M maps display qualitatively similar results in white matter and expected $f_M \sim 0$ in gray matter. The f_M is ~ 10-15% in most white matter, consistent with similar observation in human brain values (11,23). The concurrently fitted B_1^+ maps in Fig 3.7 from a C_{Gd} = 0 mM brain (results were similar at C_{Gd} = 0.5 mM) are generally smooth and primarily varying in the axial direction, as expected for B_1^+ variation that is primarily induced by the geometry of the RF coil. Some differences in B_1^+ between white and gray matter regions are apparent, (particularly in the axial view of the images collected at 15.2 T), although these differences are small and had little impact on the fitted T_2 spectra. Fig 3.8 displays mean f_M and standard deviation from three repeated scans for several regions of interest in the sagittal and axial slices. Mean f_M is similar in

each region between scan protocols, but variations between 7T and 15.2T are generally larger than differences between C_{Gd} at the same field strength. This is consistent with previous works comparing MWF at 1.5T and 3.0T (35,36) , although it is not entirely clear why MWF increases with B_0.

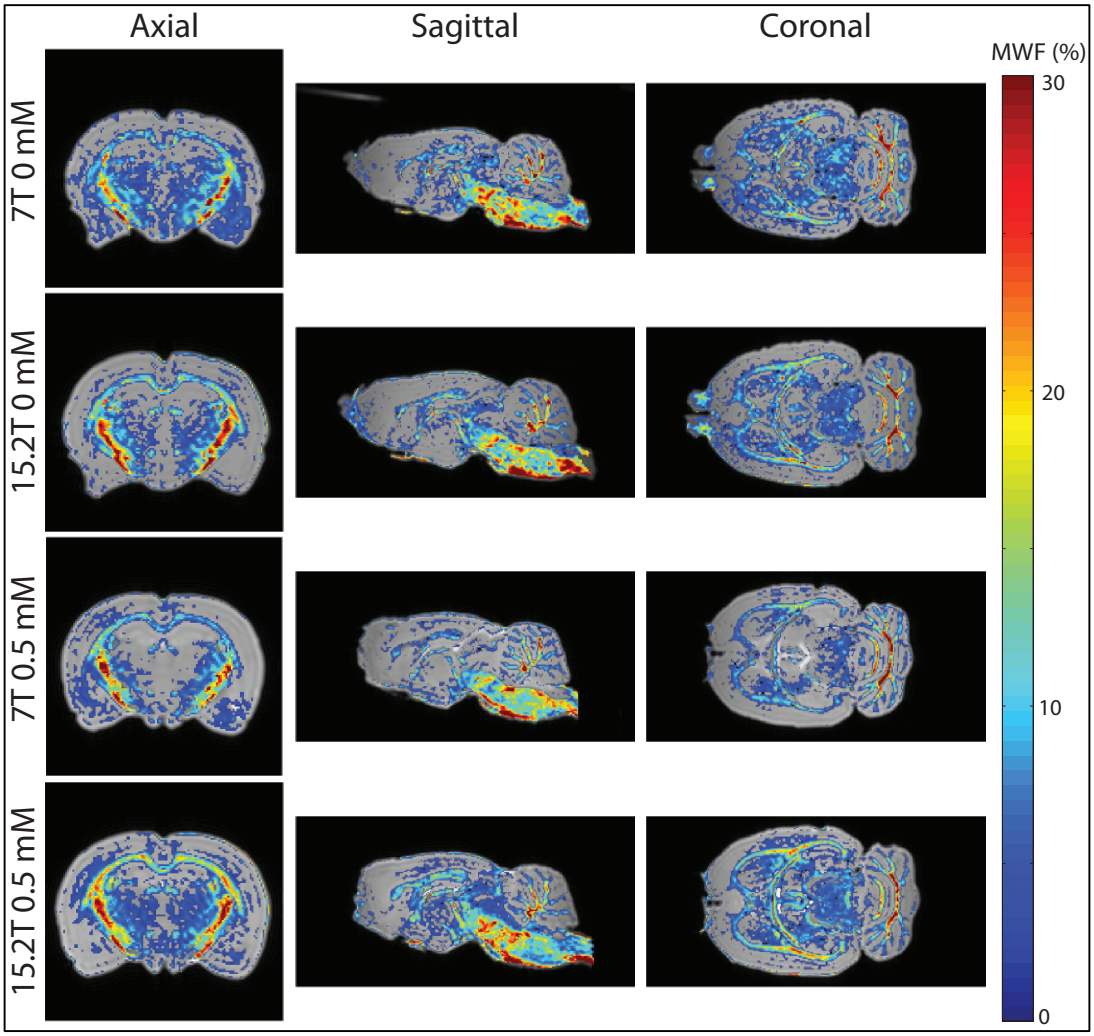

Figure 3.6. Myelin Water Fraction (f_M) maps at 7T and 15.2T with 0 and 0.5mM Gd. MET_2 data was collected using optimal scan parameters (see *2. Materials and Methods*) at 7T and 15.2T with C_{Gd} = 0mM (top) and 0.5mM (bottom). f_M was deemed the fraction of signal with a peak $T_2 < T_{2M}$ (see Fig 3.1) after MET_2 analysis using NNLS and a defined regularization parameter (see 3.2.3 Data Analysis).

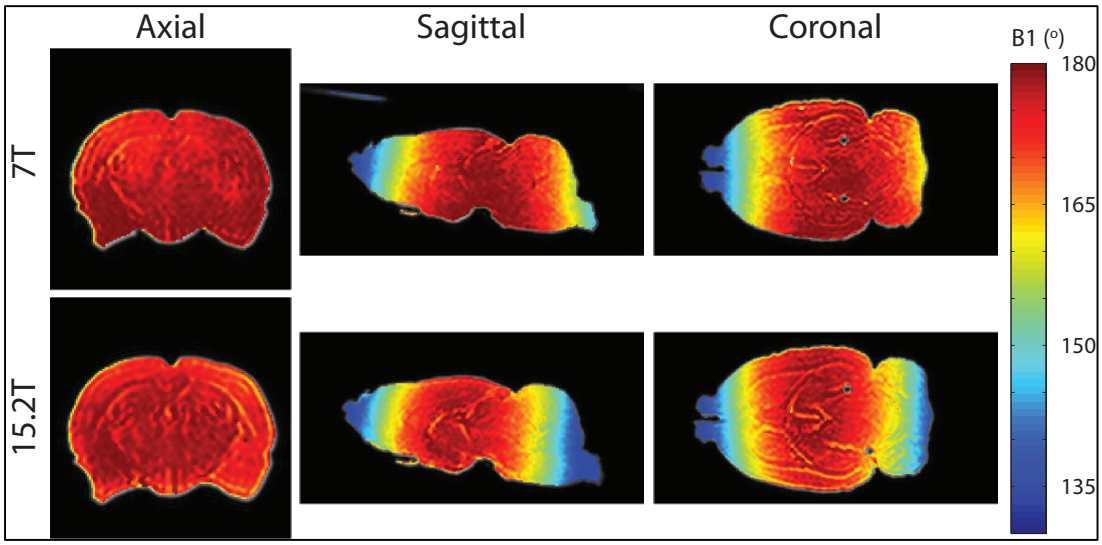

Figure 3.7. B_1^+ maps from 7T and 15.2T. B_1^+ is found from the Extended Phase Graph (EPG) algorithm (see 3.2.3 Data Analysis). B_1^+ at 15.2T varies more in the axial direction than at 7T and B_1^+ in the central axial plane at both fields is uniformly ~170-180°, as expected.

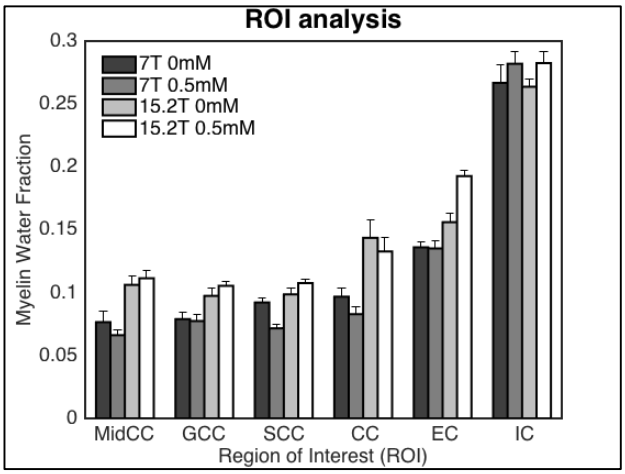

Figure 3.8. Region of Interest (ROI) f_M values across scans. Similar ROIs were drawn in each region of the brain for scans at 7T and 15.2T with C_{Gd} = 0 and 0.5mM. Three ROIs in the sagittal slice were the middle corpus callosum (Mid CC), Splenium (Spl), and Genu. Three ROIs in the axial slice were the CC, external capsule (EC), and internal capsule (IC).

Reproducibility of f_M maps between animals is demonstrated in Fig 3.9 and 3.10. Fig 3.9 displays maps from approximately the same axial slice in 3 different rat brains (a, b, and c), all with C_{Gd} = 0 mM acquired at 7T and 15.2T. Qualitatively, all maps look similar between field

strength and across brains. Fig 3.9 also displays quantitative measures of f_M and standard deviation in a corpus callosum ROI in each brain at both field strengths. We see no significant differences between brains, but higher f_M at 15.2T compared to 7T as discussed above. Similarly, Fig 3.10 displays f_M maps of 4 rat brains with C_{Gd} = 0 mM, 0.25 mM, 0.5 mM, and 1.0 mM, each acquired with predicted optimal 4-hr protocols, respectively at 15.2T. All maps in Fig 3.10 exhibit comparable results, which displays consistency over various C_{Gd}. Fig 3.10 also shows quantitative differences in f_M from a corpus callosum ROI of each slice. We see no significant differences from C_{Gd} = 0mM – 1mM, but there might be a slight increase as C_{Gd} increases.

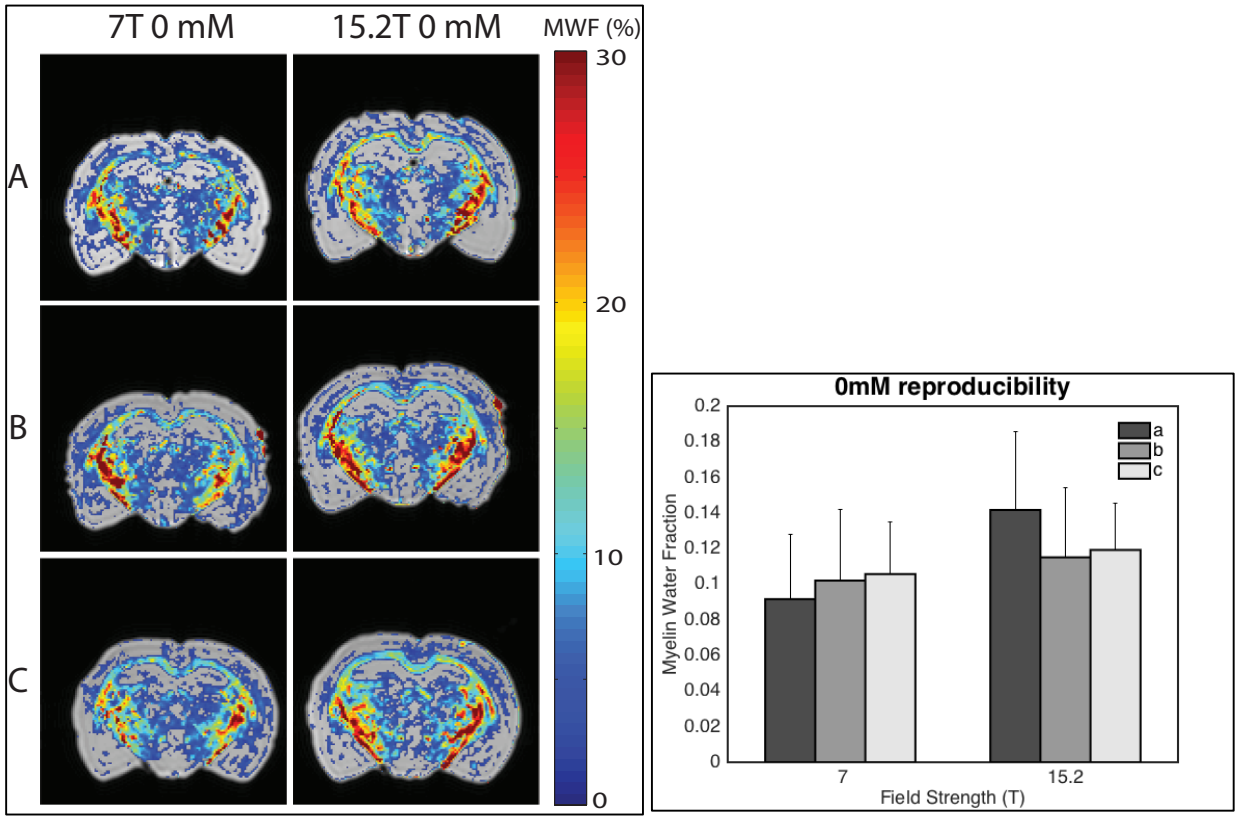

Figure 3.9. f_M maps of three different rat brains (A-C) with C_{Gd}=0mM at 7T (left) and 15.2T (right). Maps display strong similarities between 7T and 15.2T for each brain. Based on similar axial slices, all brains (A-C) show comparable f_M maps. Bar graph displays f_M and standard deviation in the corpus callosum of each brain at 7T and 15.2T with no significant differences between brains, but an increase with field strength.

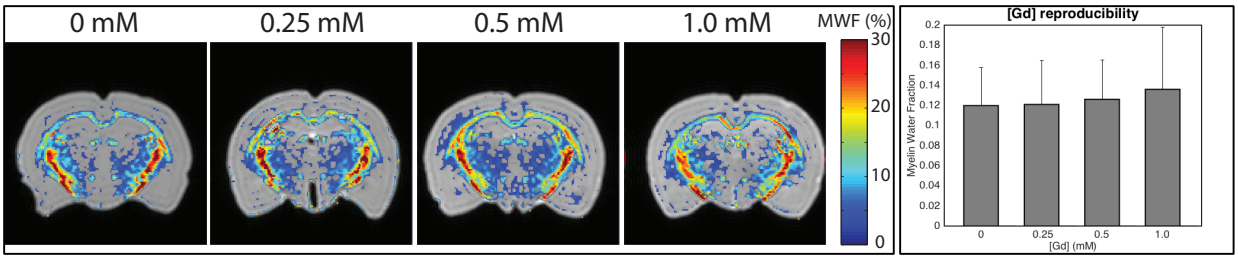

Figure 3.10. f_M maps of four rat brains with C_{Gd}=0mM, 0.25mM, 0.5mM, and 1.0mM at 15.2T obtained from predicted optimal protocols for each C_{Gd}. Based on similar axial slices, all brains show comparable f_M maps. Bar graph displays f_M and standard deviation in the corpus callosum of each brain with no significant differences between C_{Gd} but a slight increase may be due to acquisition parameters used (T_E).

Finally, we assessed the optimal parameter predictions from CRLB calculations used here and proposed by Dula et al (25). Fig 3.11 displays (top) f_M and (bottom) standard deviation across a corpus callosum ROI from 2D MET$_2$ sagittal scans at 7T and 15.2T. Data was acquired at 6 different T_E with C_{Gd} = 0, 0.25, 0.5, and 1.0mM (*See 3.2.2 Magnetic Resonance Imaging*). Contrary to CRLB predictions, for both 7T and 15.2T, we see the best agreement in f_M across C_{Gd} at the shortest T_E. As T_E increases, f_M tends to increase, likely due to statistically more challenging data fitting, especially with C_{Gd} = 0.5 or 1.0mM. This could explain the slightly higher f_M with increasing C_{Gd} in Fig 3.10 due to longer T_E used for predicted optimal SNR (*see* Table 3.1). 7T data suggest potentially some benefit in using slightly longer than minimum T_E (7.6ms) affording lower bandwidth to increase SNR and lower standard deviation.

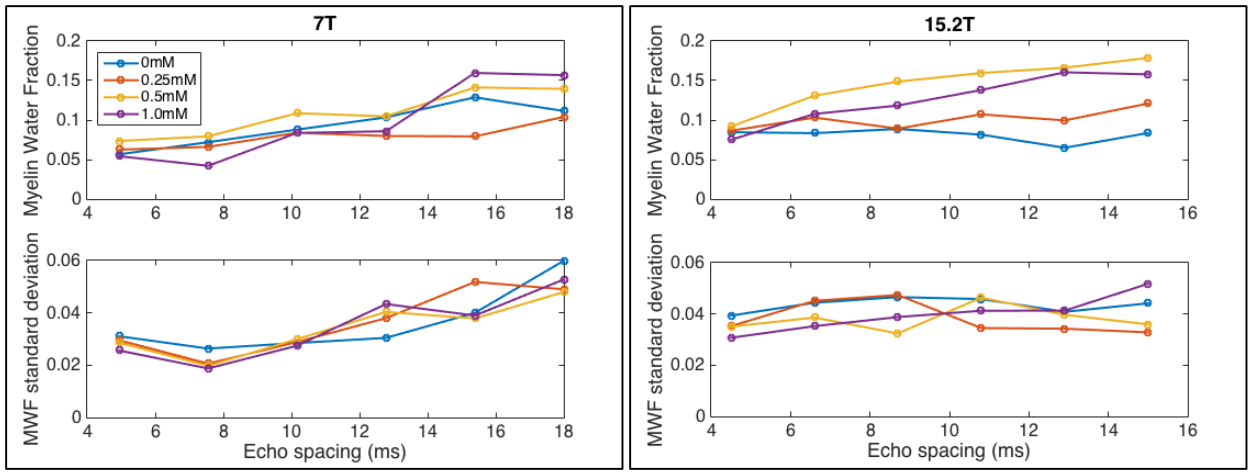

Figure 3.11. Mean and standard deviation of f_M at 7T and 15.2T. Results are from an ROI from the corpus callosum on a sagittal slice from 2D MET$_2$. Data shown from four different C_{Gd}.

Fig 3.12 displays mean +/- standard deviation of image SNR from 7T and 15.2T at each echo time. First, we see that image SNR at the shortest echo time (minimal T_2-weighting) at 15.2T is ~2.23X image SNR at 7T at all C_{Gd}, as we would expect (15.2÷7 = 2.17). Next, we can see that image SNR is > 500 in all cases at 15.2T, so this explains minimal benefit to increasing T_E since SNR is already high at minimum T_E. In contrast at 7T, image SNR with C_{Gd} = 0mM is ~270 at minimum T_E. In combination with Fig 3.11, this shows that as B_0 decreases and T_2 increases, there may be some benefit to slightly longer T_E to increase SNR, especially without or with minimal C_{Gd}. But in opposition to the CRLB predictions, at both field strengths, shorter T_E (< $T_{2,M}$) is likely the best choice for consistent f_M.

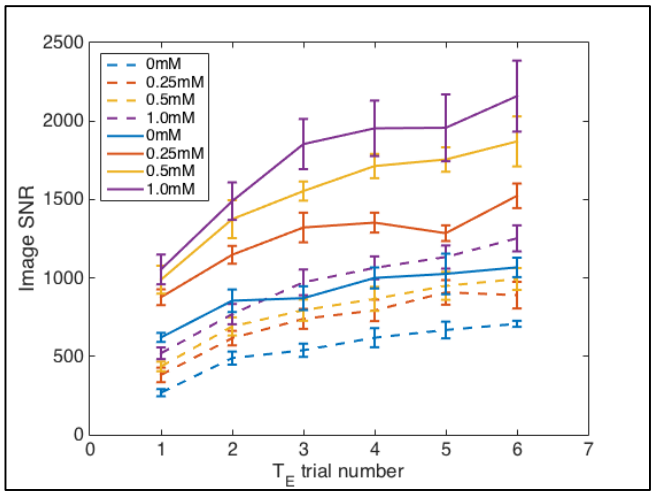

Figure 3.12. Image signal-to-noise ratio (SNR) at (dashed) 7T and (solid) 15.2T. Results are from an ROI from the corpus callosum on a sagittal slice from 2D MET$_2$. Data shown from four different C_{Gd}.

3.4 DISCUSSION

The results demonstrate feasibility of whole brain MWF mapping in excised and chemically fixed rat brains. The primary conclusions based on the experimental data, are i) increased B_0, up to at least 15.2 T, provides increased SNR efficiency with little effect on f_M, and ii) loading tissue with up to ≈ 1 mM Gd improves or modestly decreases f_M precision. While Fig 3.11, especially at 15.2T, does not agree with predictions from the two-pool model, this is not surprising since tissue is much more complicated than bi-exponential water components. As noted above, another factor that may be limiting the accuracy of the two-pool model is the assumption that both pools are affected equally by the addition of contrast agent. In the least, the model and experimental data support the idea that MWI of *ex vivo* rodent brains can be extended to ultra-high field and will tolerate the use of some Gd, with little or no cost in f_M precision with $T_E < T_{2,M}$. These observations are important because both increased B_0 and the use of Gd have been shown previously to benefit other *ex vivo* brain imaging protocols (17,37,38). For example, preparing

monkey brains slices with 1 mM Gd was previously recommended for optimizing diffusion weighted imaging 4.7T (18).

Between the four protocols demonstrated in Figs 3.4 and 3.5, f_M maps are similar but not identical, suggesting that comparing f_M values should be restricted to data acquired at the same B_0 and loaded with the same concentration of Gd. Similarly, because MET_2 data analysis is an inherently ill-posed inverse problem, the choice of fitting technique will impact results. The linear inverse approach has the advantage of not requiring any a priori knowledge about the number of distinct T_2 components; however, one must still decide on the type and extent of spectral regularization, and how to extract a finite number of signal components from the fitted spectrum. Fitting multiple gaussian shaped components requires a priori determination of the number of components and the width of these components, presenting the potential for a poor fit. However, as noted here, there is little cost in over-estimating the number of components somewhat, and this approach brings two other advantages: a reduction in the degrees of freedom of the problem, resulting in greater fitted parameter precision, and the ability to accurately account for overlapping spectral components. While Fig 3.4 demonstrates somewhat smoother f_M maps from multiple gaussian fitting and minimum curvature with voxel-wise adjustment of regularization, these techniques are time-consuming and may not be appropriate for whole brain applications without increased computer power. For example, to estimate 7,355 non-zero voxels in one axial slice implemented using MATLAB and run on a computer with 3.0GHz AMD Phenom processor with 16Gb RAM, average processing times were 1.85, 3.24, 0.070, and 0.036 sec/voxel for multiple-gaussian, GCV-adjusted minimum curvature, minimum curvature with constant regularization weighting, and unregularized fit, respectively. Therefore, in the current case, constant regularization weighting provides consistency with commonly used methods

which employ some spectral regularization while obtaining large-scale results in a time-efficient manner. Ultimately, the important point is that any number of MET_2 analysis routines may be used to produce similar results.

One aspect of the MET_2 analysis that is demonstrated to be critical for whole brain studies is the inclusion of B_1^+ as a free parameter. For a single axial slice, it is likely that one can calibrate effective refocusing to be 170°-180° across the entire slice, as we see from central axial slices in Fig 3.7. At this range of flip angles the refocusing is > 99% efficient ($\sin^2(170°/2) = 0.992$), so spoiling the non-refocused signal will increase apparent transverse relaxation rate only modestly by $-\log\{\sin^2(\theta/2)\}/T_E < 1\ s^{-1}$ for $T_E \geq 7.5$ ms (39) . However, for flip angles of 140°, 150°, and 160°, (as can be seen at the axial extremes of the rat brains in Fig 3.6) the corresponding apparent rate increases with $T_E = 7.5$ ms are a much larger 16.6, 9.2, and $4.1 s^{-1}$, respectively. Without B_1^+ fitting as part of the MET_2 analysis, these rate increases will shift the T_2 spectrum to the left, reducing the ratio of long- to short-T_2 values and, therefore, result in noisier f_M maps. Additionally, as θ deviates further from 180°, greater crusher gradient areas are required to effectively remove non-spin-echo signals. For example, dephasing transverse magnetization by 2π radians across a 250-μm thick slice using a 1-ms crusher gradient requires approximately 100 mT/m gradient amplitude, so a multiple spin echo sequence using linearly modulated crusher gradients (40) requires $N_E/2 \times 100$ mT/m peak gradient amplitude. Typical gradient systems available on small animal MRI systems have a maximum amplitude of 400 – 1000 mT/m, making proper spoiling impractical to implement. B_1^+ fitting can account for spatial variations in flip angle and reduce effects from these confounding factors in MET_2 data.

While the methods described here were based on rat brain model predictions, they were also tested on an *ex vivo* mouse brain as demonstrated in Fig 3.13. The voxel size was decreased

to 150 µm isotropic resolution and scan time was increased to 6 hours to increase SNR. The brain was doped with 1 mM of Gd, because it was prepared for a separate study including diffusion weighted imaging. Using calculated parameters from our model of $T_R/T_E/N_E/BW/N_{EX}$ = 520 ms/5.8 ms/18/38.5 kHz/6 and fit using the NNLS fitting with a constant minimum curvature regularization as above, f_M maps were obtained in mouse brain at 15.2 T. Maps display comparable results to those from rat brain (Fig 3.5), with f_M ~ 10-15% in most white matter, demonstrating the ability to extend MWI to *ex vivo* mouse brain.

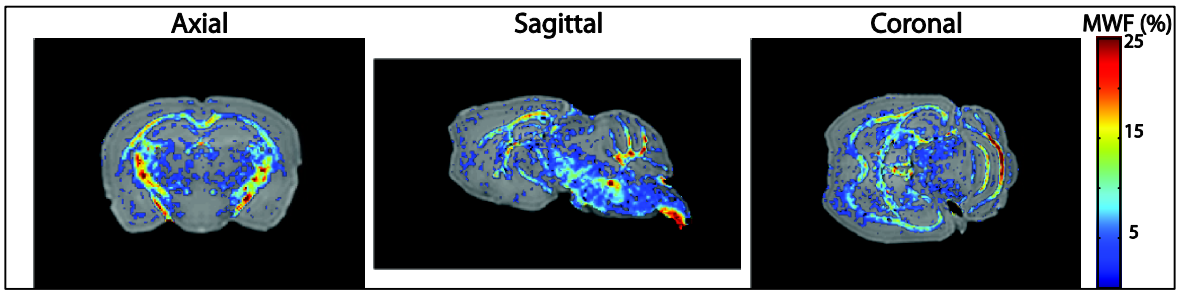

Figure 3.13. Mouse f_M maps collected at 15.2T. (Left to right) Images are from the axial, sagittal and coronal planes with respect to the magnet, respectively. Data was collected using a 6 hour protocol at 150µm isotropic resolution and tissue was loaded with 1mM of Gd.

3.5 CONCLUSIONS

Using a two-pool model of transverse relaxation in white matter as well as measurement relaxation and Gd relaxivity characteristics in rat brain at 7 T and 15.2 T, predicted optimal approaches for MWI in *ex vivo* rodent brains is presented. While the results do not fully support the simple two-pool model, the results demonstrate that both increasing B_0 and the loading of tissue with Gd provides improved SNR efficiency with minimal effect on MWF. Whole brain high-resolution (250 µm isotropic) MWF maps were demonstrated with 4hr scan times, and results were roughly consistent across a range of Gd concentrations and between 7 T and 15.2 T. Mouse brain MWI was demonstrated at 150 µm isotropic resolution in a 6-hr scan with similar results. Additionally, we show that it is not critical to optimize protocols, but $T_E < T_{2,M}$ should be used.

ACKNOWLEDGEMENTS

Grant Sponsors: NIH EB001744 and NSF Graduate Research Fellowship 2011126474.

3.6 APPENDIX

MULTIPLE GAUSSIAN FITTING

Fitting the multiple spin echo data to a T_2 spectrum and an effective refocusing pulse flip angle, θ, was performed as follows. First, the linear inverse solutions followed the method described by Prasloski et al (23) and briefly restated here. Let column vector **d** define the N_E spin echo signals; let column vector **s** define the full fitted T_2 spectrum, N_T elements long; and let $\mathbf{A}(\theta)$ be the system matrix that defines a normalized signal amplitude at every echo time, t_i, i = 1 to N_E, for every time constant $T_{2,j}$, j = 1 to N_T, and refocusing flip angle θ. This **A** matrix can be computed using the EPG algorithm (21). The signal equation is then

$$\mathrm{d} = \mathrm{A}(\theta)\mathrm{s} \qquad [A1]$$

and **s** can be estimated by NNLS,

$$\hat{\mathrm{s}} = \arg\min_{\mathrm{s}} \left\| \mathrm{A}(\theta)\mathrm{s}\text{-}\mathrm{d} \right\|, \ \mathrm{s} \geq 0 \qquad [A2]$$

given **d** and $\mathrm{A}(\theta)$. Since θ is unknown, it must be estimated as $\hat{\theta}$; to do so, a system matrix $\mathrm{A}(\theta_k)$ was computed for each of k = 1 to N_θ, where the range of θ values spanned the expected flip angles. For the present work, N_θ = 10 and θ was uniformly spaced between 130° and 180°. For linear inverse solutions, the sum square errors, e_k, were computed as

$$\mathrm{e}_\mathrm{k} = \left\| \mathrm{A}(\theta_\mathrm{k})\hat{\mathrm{s}}_\mathrm{k}\text{-}\mathrm{d} \right\|, \ \mathrm{k} = 1 \text{ to } \mathrm{N}_\theta \qquad [A3]$$

A spline interpolation was then used to compute $\hat{\theta}$ as the flip angle that minimizes the fit error, and the final spectral estimate, $\hat{s}$, was computed from Eq [A2] with system matrix $\mathbf{A}(\hat{\theta})$.

Extending this framework to multiple gaussian component fitting was done by decomposing the spectrum **s** into a linear combination of N_G gaussian shaped spectral components, then employing a separable least squares approach (Golub and Pereyra, 2003). That is, let

$$s = G(\alpha)f \qquad [A4]$$

where $\mathbf{G}(\boldsymbol{\alpha})$ is a N_T x N_G matrix, each column being a gaussian shaped function in log-T_2 space, centered at $T_{2,l} = \alpha_l$ for l = 1 to N_G, and **f** is a column vector of N_G component amplitudes. Therefore,

$$d = A(\theta)G(\alpha)f\,. \qquad [A5]$$

The component T_2 values are estimated by non-linear regression

$$\hat{\alpha} = \arg\min_{\alpha} \left\| A(\theta)G(\alpha)\hat{f}(\alpha)-d \right\| \qquad [A6]$$

where

$$f(\alpha) = \arg\min_{f} \left\| A(\theta)G(\alpha)f-d \right\|,\ f \geq 0. \qquad [A7].$$

As above, θ is estimated by repeating the process over a range of flip angles.

3.7 REFERENCES

1. Bitsch A, Kuhlmann T, Stadelmann C, Lassmann H, Lucchinetti C, Brück W. A longitudinal MRI study of histopathologically defined hypointense multiple sclerosis lesions. Annals of Neurology 2001;49:793–796. doi: 10.1002/ana.1053.

2. Brück W, Bitsch A, Kolenda H, Brück Y, Stiefel M, Lassmann H. Inflammatory central nervous system demyelination: Correlation of magnetic resonance imaging findings with lesion pathology. Annals of Neurology 1997;42:783–793. doi: 10.1002/ana.410420515.

3. Bakshi, Thompson, Rocca, Pelletier. MRI in multiple sclerosis: current status and future prospects. 2008.

4. Fu, Matthews, Stefano D, Worsley, Narayanan, Francis, Antel, Wolfson, Arnold. Imaging axonal damage of normal-appearing white matter in multiple sclerosis. Brain 1998;121:103–113. doi: 10.1093/brain/121.1.103.

5. Horsfield M, Jones D. Applications of diffusion-weighted and diffusion tensor MRI to white matter diseases – a review. NMR in Biomedicine 2002;15:570–577. doi: 10.1002/nbm.787.

6. Larsson H, Frederiksen, Petersen, Nordenbo, Zeeberg, Henriksen, Olesen. Assessment of demyelination, edema, and gliosis by in vivo determination of T1 and T2 in the brain of patients with acute attack of multiple sclerosis. Magnetic Resonance in Medicine 1989;11:337–348. doi: 10.1002/mrm.1910110308.

7. Ebisu T, Naruse S, Horikawa Y, Ueda S, Tanaka C, Uto M, Umeda M, Higuchi T. Discrimination between different types of white matter edema with diffusion-weighted MR imaging. Journal of Magnetic Resonance Imaging 1993;3:863–868. doi: 10.1002/jmri.1880030612.

8. Smith, Weinstein, Modic. Magnetic resonance with marked T2-weighted images: improved demonstration of brain lesions, tumor, and edema. 1985.

9. Menon RS, Rusinko MS, Allen PS. Proton relaxation studies of water compartmentalization in a model neurological system. Magnetic Resonance in Medicine 1992;28:264–74. doi: 10.1002/mrm.1910280208.

10. Vasilescu V, Katona E, Simplâceanu V, Demco D. Water compartments in the myelinated nerve. III. Pulsed NMR result. Experientia 1978;34:1443–4. doi: 10.1007/BF01932339.

11. Mackay A, Whittall K, Adler J, Li D. In vivo visualization of myelin water in brain by magnetic resonance. Magnetic Resonance in Medicine 1994;31:673–7. doi: 10.1002/mrm.1910310614.

12. Gareau P, Rutt B, Bowen C, Karlik S, Mitchell JR. In vivo measurements of multi-component T2 relaxation behaviour in guinea pig brain. Magnetic Resonance Imaging 1999;17:1319–1325. doi: 10.1016/S0730-725X(99)00064-8.

13. Dula AN, Gochberg DF, Valentine HL, Valentine WM, Does MD. Multiexponential T2, magnetization transfer, and quantitative histology in white matter tracts of rat spinal cord. Magnetic Resonance in Medicine 2010;63:902–9. doi: 10.1002/mrm.22267.

14. Kozlowski, Raj, Liu, Lam. Characterizing white matter damage in rat spinal cord with quantitative MRI and histology. 2008. doi: 10.1089/neu.2007.0462.

15. McCreary C, Bjarnason T, Skihar V, Mitchell R, Yong W, Dunn J. Multiexponential T2 and magnetization transfer MRI of demyelination and remyelination in murine spinal cord.

NeuroImage 2009;45. doi: 10.1016/j.neuroimage.2008.12.071.

16. Does MD, Gore JC. Compartmental study of T1 and T2 in rat brain and trigeminal nerve in vivo. Magnetic Resonance in Medicine 2002;47:274–83. doi: 10.1002/mrm.10060.

17. Benveniste H, Blackband S. MR microscopy and high resolution small animal MRI: applications in neuroscience research. Progress in Neurobiology 2002;67:393420. doi: 10.1016/S0301-0082(02)00020-5.

18. D'Arceuil, de Crespigny. The effects of brain tissue decomposition on diffusion tensor imaging and tractography. 2007.

19. Johnson A, Cofer G, Fubara B, Gewalt S, Hedlund L, Maronpot R. Magnetic resonance histology for morphologic phenotyping. Journal of Magnetic Resonance Imaging 2002;16:423–429. doi: 10.1002/jmri.10175.

20. Poon C, Henkelman R. Practical T2 quantitation for clinical applications. J Magn Reson Im 1992;2:541–53. doi: 10.1002/jmri.1880020512.

21. Hennig. Echoes—how to generate, recognize, use or avoid them in MR-imaging sequences. Part I: Fundamental and not so fundamental properties of spin echoes. 1991. doi: 10.1002/cmr.1820030302.

22. Lebel MR, Wilman AH. Transverse relaxometry with stimulated echo compensation. Magnetic Resonance in Medicine 2010;64:1005–14. doi: 10.1002/mrm.22487.

23. Prasloski T, Mädler B, Xiang Q. Applications of stimulated echo correction to multicomponent T2 analysis. Magnetic Resonance in Medicine 2012;67:1803–14. doi: 10.1002/mrm.23157.

24. Anastasiou A, Hall. Optimisation of T2 and M0 measurements of bi-exponential systems. Magnetic resonance imaging 2004;22:67–80. doi: 10.1016/j.mri.2003.05.005.

25. Dula, Gochberg, Does. Optimal echo spacing for multi-echo imaging measurements of bi-exponential T 2 relaxation. 2009. doi: 10.1016/j.jmr.2008.11.002.

26. Dortch, Apker, Valentine. Compartment-specific enhancement of white matter and nerve ex vivo using chromium. 2010. doi: 10.1002/mrm.22460.

27. Whittall K, MacKay A. Quantitative interpretation of NMR relaxation data. Journal of Magnetic Resonance 1989;84:134–52. doi: 10.1016/0022-2364(89)90011-5.

28. Bonilla I, Snyder R. Transverse relaxation in rat optic nerve. NMR Biomed 2007;20:113–120. doi: 10.1002/nbm.1090.

29. Dortch RD, Harkins KD, Juttukonda MR, Gore JC, Does MD. Characterizing inter

compartmental water exchange in myelinated tissue using relaxation exchange spectroscopy. Magnetic resonance in medicine 2013;70:1450–59. doi: 10.1002/mrm.24571.

30. Lawson, Hanson. Solving least squares problems. 1974.

31. Golub, Heath, Wahba. Generalized cross-validation as a method for choosing a good ridge parameter. 1979. doi: 10.1080/00401706.1979.10489751.

32. De Graaf RA, Brown PB, McIntyre S, Nixon TW, Behar KL, Rothman DL. High magnetic field water and metabolite proton T1 and T2 relaxation in rat brain in vivo. Magnetic resonance in medicine 2006;56:386–94. doi: 10.1002/mrm.20946.

33. Gareau P, Rutt B, Karlik S, JR Mitchell. Magnetization transfer and multicomponent T2 relaxation measurements with histopathologic correlation in an experimental model of MS. Journal of Magnetic Resonance Imaging 2000;11:586–95. doi: 10.1002/1522-2586(200006)11:6<586::AID-JMRI3>3.0.CO;2-V.

34. Rohrer M, Bauer H, Mintorovitch J, Requardt M, Weinmann H-JJ. Comparison of magnetic properties of MRI contrast media solutions at different magnetic field strengths. Invest Radiol 2005;40:715–24. doi: 10.1097/00004424-200511000-00005.

35. Kolind SH, Mädler B, Fischer S, Li D, MacKay AL. Myelin water imaging: Implementation and development at 3.0T and comparison to 1.5T measurements. Magnetic Resonance in Medicine 2009;62:106–15. doi: 10.1002/mrm.21966.

36. Oh, Han, Pelletier, Nelson. Measurement of in vivo multi-component T2 relaxation times for brain tissue using multi-slice T2 prep at 1.5 and 3 T. 2006.

37. Dhenain M, Delatour B, Walczak C, Volk A. Passive staining: A novel ex vivo MRI protocol to detect amyloid deposits in mouse models of Alzheimer's disease. Magnetic Resonance in Medicine 2006;55:687–693. doi: 10.1002/mrm.20810.

38. Johnson AG, Cofer GP, Gewalt SL, Hedlund LW. Morphologic Phenotyping with MR Microscopy: The Visible Mouse. Radiology 2002;222:789–93. doi: 10.1148/radiol.2223010531.

39. Does M, Gore J. Complications of nonlinear echo time spacing for measurement of T2. NMR in Biomedicine 2000;13:1–7.

40. Crawley, Henkelman. Errors in T2 estimation using multislice multiple-echo imaging. Magnetic Resonance in Medicine 1987;4:34–47. doi: 10.1002/mrm.1910040105.

CHAPTER 4

DEVELOPMENT OF HISTOLOGY ANALYSIS METHODS

4.1 INTRODUCTION

Histology is the gold standard for validation of MRI parameters; however, there is no standard technique to quantitatively analyze electron microscopy images to obtain robust measures of features such as axon diameter and myelin thickness. This is exhibited by numerous groups utilizing different, independently written in-house code to analyze microscopy images (1–4). Generally, images can be segmented manually, semi-automatically or fully-automatically. Manual segmentation provides flexibility for variations in images but is time-consuming and user-dependent. Conversely, fully automatic segmentation requires no user-input but must be very robust to adapt to variability between image illumination, structure, etc. Instead, semi-automatic segmentation decreases user-dependency but provides some user-control to ensure proper segmentation.

Segmentation algorithms are based on one or a combination of a few different techniques: intensity thresholding, feature detection, morphological filtering, region accumulation, and deformable model fitting. Intensity thresholding assumes objects of interest are significantly different from the background. These are the simplest methods and remain a predominantly used segmentation technique. Feature detection utilizes a unique property such as a characteristic shape of the objects of interest to pick it out. Morphological filtering is generally

used as a pre- or post-processing step and uses operators such as erosion, dilation, etc. to edit the geometric properties of the image. Region accumulation begins at a seed point and depicts neighborhood regions with similar properties. Finally, deformable model fitting, such as snakes, minimizes the deformation energy based on *a priori* image information. Here, we use several of these techniques to analyze electron microscopy images via manual and semi-automatic methods to obtain a robust segmentation method (5).

4.2 MEASURING AXON DIAMETER (*d*)

4.2.1 Manual Measurement

We used a binary image defined manual global threshold, defined by the *nadir* of the image histogram as described below (See 4.4.1 Global Threshold). To measure axon diameter (*d*), we manually drew perpendicular line across the major and minor axes of the axon as shown by the blue lines in Fig 4.1. The axon diameter for each axon was the mean of these two measurements.

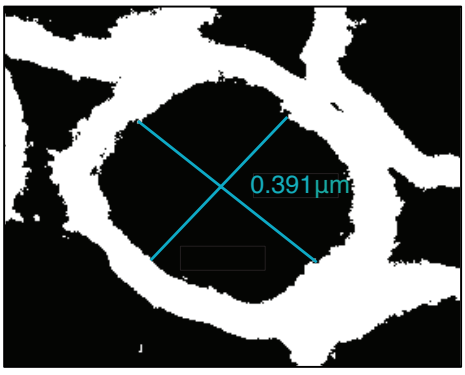

Figure 4.1. Manual axon diameter measurements. Two lines are manually draw across the major and minor axes of the axon (blue lines).

This method was very user dependent in the following ways: 1) the user determined which axes were the major and minor axes, which is even more difficult in irregularly-shaped axons, 2) measurements were dependent on how perpendicular the user drew lines, and 3) this method was time-intensive on the user.

4.2.2 Region-growing Method

To decrease user-dependency from manual measurements of *d*, we implemented a region-growing technique (6). The user selected a seed point within each axon on the threshold image and pixels = 1 inside axons but not deemed by the operator to be myelin were manually set = 0. After this, from the seed voxel the region growing algorithm (*regiongrowing*) grew. Each pixel was compared to the region mean intensity and grown until it reached a pixel with a difference larger than 0.1 as shown in Fig 4.2. The diameter of each axon (*d*) was then computed from its corresponding area (*a*) as $d_i = 2*\sqrt{a_i/\pi}$, where i = 1: number of axons. However, while this method was much more automatic and less user-dependent, it was still very time-dependent for the user. Since the region-growing algorithm can continue growing through pixel gaps, the user needed to ensure that every myelin edge from the threshold image was sealed to prevent a leak of the region-growing area which is very tedious and user-time-intensive.

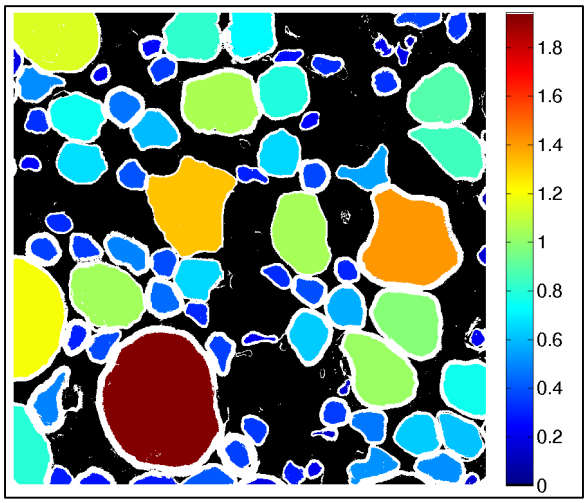

Figure 4.2. Region growing axon diameter measurements. Axon region is grown from a seed point in each axon, with colors displaying axon diameter (*d*).

4.2.3 Snakes (Active contour model) Method

To decrease the sensitivity of the region-growing algorithm, we implemented the *snakes* algorithm – *Snake2D* (7–9). Similar to region-growing, the input was a threshold image, the user selected seen points in each axon and pixels labeled = 1 but not deemed by the operator to be myelin were manually set = 0. However, now it was not necessary for the user to seal each myelin boundary. This is due to the character of the *snakes* model. Snakes or active contour models use a contour ($x(s,t)$; s = space (curve), t = time (iteration)) that deforms to image features by minimizing the potential energy of the curve. Potential energy (E_{snake}) is defined in as,

$$E_{snake} = \oint E_{internal}(x)ds + \oint E_{external}(x)ds + \oint E_{image}(x)ds \qquad [4.1]$$

where $E_{internal}$ defines the tension and stiffness of the contour line, $E_{external}$ controls attraction and repulsion forces and E_{image} is defined as,

$$E_{image} = w_{line} E_{line} + w_{edge} E_{edge} + w_{term} E_{term} \quad [4.2]$$

where E_{line}, E_{edge}, and E_{term} attracts the contour to light or dark regions, image edges, or image terminations (corners), respectively with weighting terms w_{line}, w_{edge}, and w_{term}.

In our case, we we want to guide the curves to the axon/myelin edge so we use a strong edge energy weighting (W_{edge} = 3), with some weighting to guide the contour to myelin, light regions (W_{line} = 0.2) and no terminal (corners) weighting (W_{term}=0). By controlling the tension and stiffness in $E_{internal}$ ($\alpha = 0.075$ and $\beta = 0.1$, respectively) we create a contour that can conform to the irregular shapes of axons but not escape breaks in the myelin.

After we run snakes on each axon, we can again compute the diameter, *d* for each axon by $d_i = 2*\sqrt{a_i/\pi}$ where *i* = 1: number of axons. Fig 4.3 displays the results from *Snakes*, showing good agreement with axon edges and the final contours. The colors represent the axon diameter calculated for each axon.

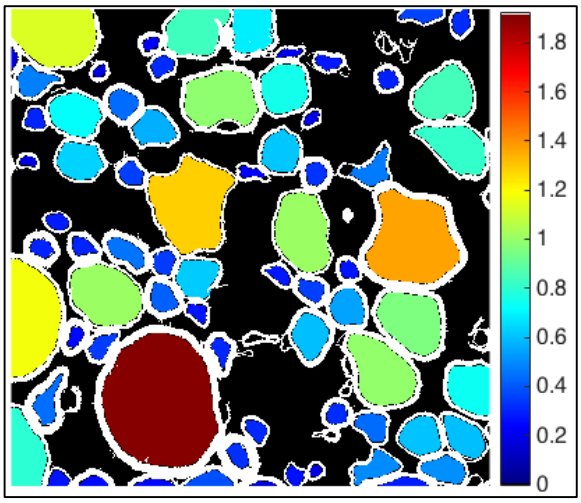

Figure 4.3. Snakes axon diameter measurements. Axon region is grown using snakes algorithm from a seed point in each axon, with colors displaying axon diameter (*d*).

4.2.4 Comparison of Methods

Next, we wanted to compare the sensitivity of d to various measurement techniques-- manual, region-growing, and snakes (active contour) methods. It is of note that the manual measurements were performed on only half of the data (n = 2135 axons), so we limited comparisons with manual measures to these data. First, we compare d from manual versus region-growing in Fig 4.4 and see a strong 1:1 relationship between measures with Pearson's ρ = 0.97 and mean-squared error (MSE) = 0.007.

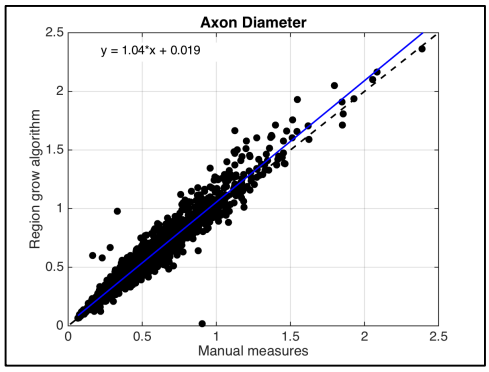

Figure 4.4. Comparison of manual and region-growing axon diameter techniques. Each point represents a single axon with axon diameter (d).

Next, we compare d from manual to snakes as show in Fig 4.5 and again see strong correlation with ρ = 0.97 and MSE = 0.006

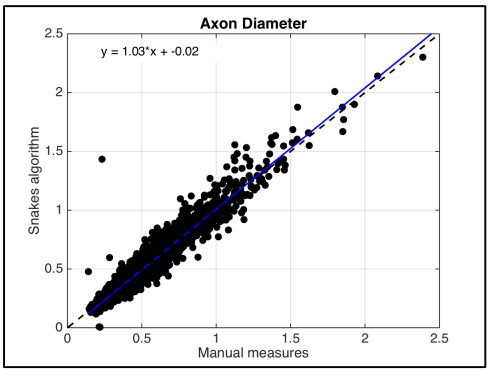

Figure 4.5. Comparison of manual and snakes axon diameter techniques. Each point represents a single axon with axon diameter (*d*).

Finally, we compare region-growing to snakes methods and see that these two techniques are extremely similar, as hoped, with $\rho = 0.99$ and MSE = 0.03 and almost all points lying on the line of unity (Fig 4.6). Therefore, we can conclude that snakes method is the best technique due to user-independence in measurements and decreases in user time-demand. We also see that axon diameter is a relatively insensitive measurement, with all three techniques providing similar results.

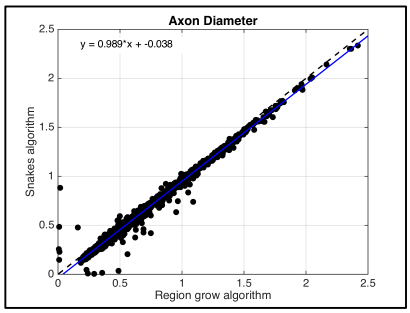

Figure 4.6. Comparison of region-growing and snakes axon diameter techniques. Each point represents a single axon with axon diameter (*d*).

4.3 MEASURING MYELIN THICKNESS (Δ)

4.3.1 Manual Measurement

We used a binary image defined by the *nadir* of the image histogram (*See* 4.4.1 Global Threshold). To measure myelin thickness (*⊿*), we manually drew perpendicular line across the myelin thickness at the major and minor axes of the axon as shown by the pink lines in Fig 4.7. The myelin thickness for each axon was the mean of these two measurements. However, this technique suffers from the same negatives as manual measurements of axon diameter– user-dependency and time intensive.

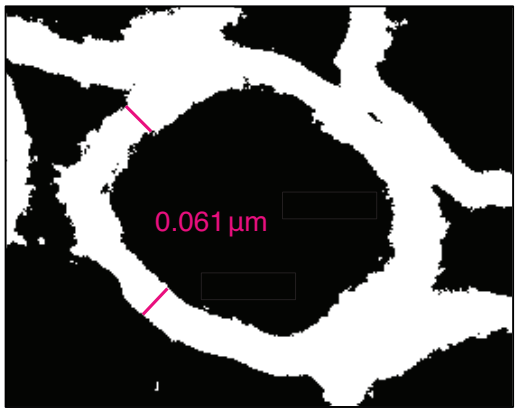

Figure 4.7. Manual myelin thickness measurements. Two lines are manually draw across the myelin (pink lines) at the major and minor axes of the axon (blue lines in Fig 4.1).

4.3.2 Radial Sampling

To increase reliability of Δ measures, we wanted an automatic approach that would radially sample the myelin thickness around the axon. Because the Otsu threshold resulted in uneven segmentation of the myelin (10), the myelin of each axon was independently segmented on the original histology image. The final boundary from the snakes axon segmentation was used as the starting contour (blue stars). Each contour was grown outward along lines normal to its tangent (~0.06µm between lines) until reaching a pixel intensity greater than the average intensity of pixels from the initial contour (green stars) displayed in Fig 4.8.

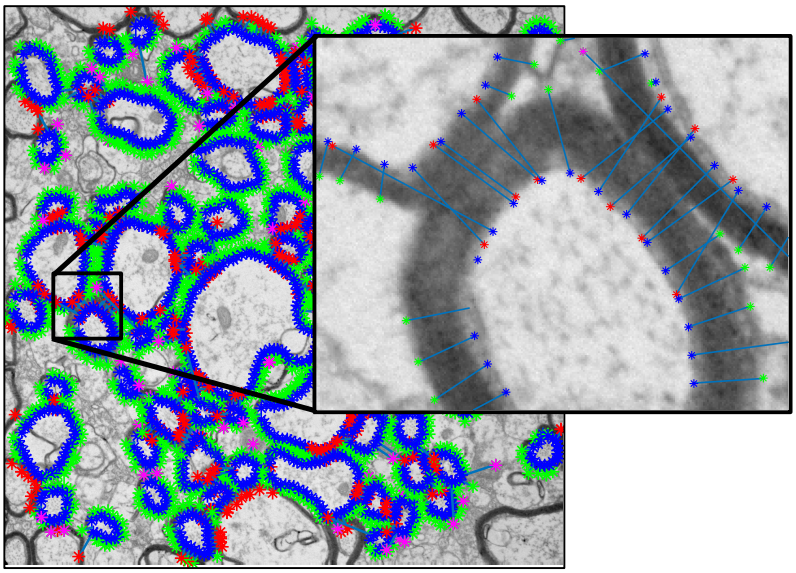

Figure 4.8. Radial sampling myelin thickness measurements. Lines are automatically grown radially perpendicular to the perimeter of the axon area with ~0.06μm between lines.

In order to reject normal lines that grew into the myelin of adjacent axons, a line was discarded if 1) its terminal point matched the location of an axon boundary defined above (red stars), or 2) length was greater than 3 times the median absolute deviation (magenta stars) (11). The median of the remaining lines defined the myelin thickness for that axon, Δ. Finally, myelin area for each axon was determined by uniformly growing the initial contour of each axon to a uniform thickness, Δ, as shown in Fig 4.9. The resulting binary image provided a measure of myelin volume fraction, $f_{\mathrm{M,Hist}} = \frac{a_{\mathrm{pixels=1}}}{a_{\mathrm{im}}}$ for each image, where $a_{\mathrm{pixels=1}}$ is the area of myelin pixels and a_{im} is the image area.

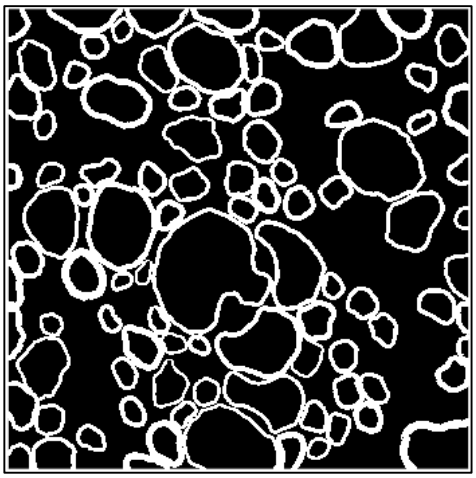

Figure 4.9. Segmented myelin image from radial sampling. The sum of pixels = 1 provides a myelin volume fraction, $f_{M,HIST}$.

While the technique performs well most of the time, we must still perform quality assurance. Fig 4.10 displays an example of how the technique fails when the myelin cannot be adequately sampled, in this case due to being surrounded by other axons (blue arrows). To overcome this, we acquire 2 manual measurements on the original image and use the mean value.

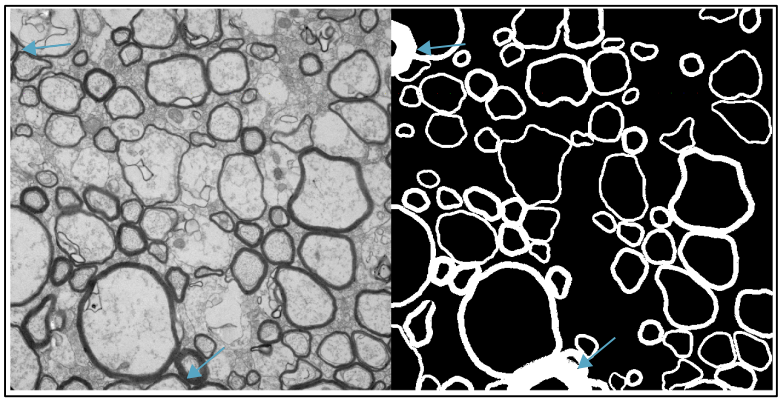

Figure 4.10. Breakdown in segmented myelin image from radial sampling. Blue arrows point to axons where radial sampling did not perform well and must be manually assessed.

4.3.3 Comparison of Methods

Next, we wanted to compare the sensitivity of Δ measurements to the measurement techniques– manual and radial sampling methods. The manual Δ measurements were performed on almost all of the data (n = 3447 axons). First, we compare Δ from manual versus radial sampling in Fig 4.11 below and see a strong linear relationship between measures with Pearson's ρ = 0.68 and root mean-squared error (RMSE) = 0.040. We can see that we are consistently getting larger myelin thickness measures from our radial grow technique. This is not surprising since we expected that we were underestimating myelin using our global thresholding technique. (*See* 4.4.1 Global Threshold).

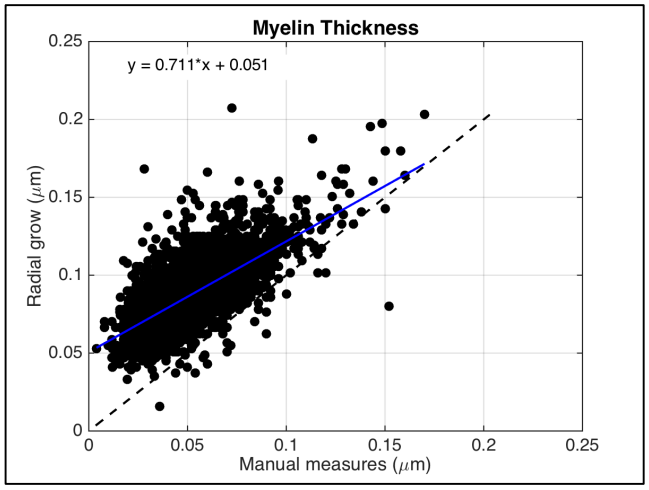

Figure 4.11. Myelin thickness from manual and radial sampling techniques. Each point represents one axon.

However, it is difficult to assess how "correct" our measures of myelin thickness are. To assess our technique we compared the results to a technique developed by Begin et al. for analyzing coherent anti-Stokes Raman scattering (CARS) microscopy images (12). Fig 4.12 shows and original EM image along with the segmented myelin image from the CARS technique and our radial growing technique. Qualitatively, the segmented images look similar. It is of note that the

CARS histology technique is not able to assess axons that do not lie fully in the image, which is important for our application. Additionally, the CARS technique smooths the axon perimeter more than the radial technique.

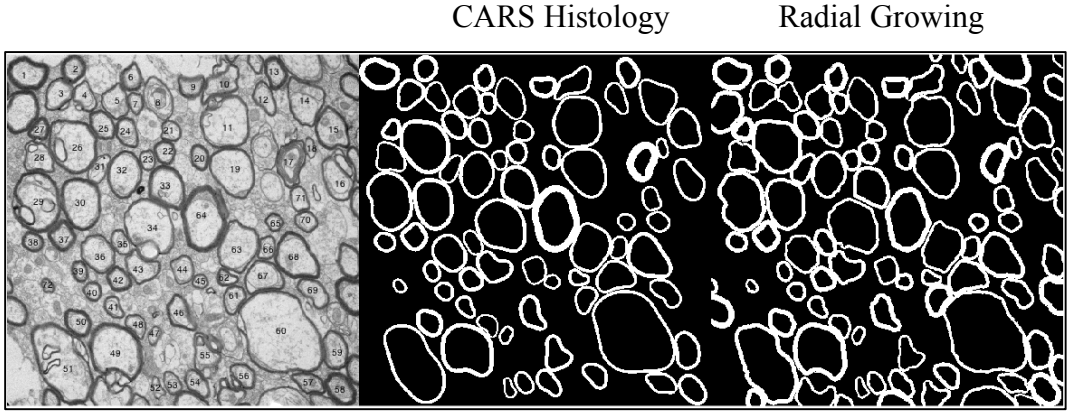

Figure 4.12. Comparison between CARS histology method and radial sampling for obtaining segmented myelin images.

If we quantitatively compare the two measures, we see a near 1:1 line of best fit and data points lying around the line of unity shown in Fig 4.13. There is a strong linear correlation (Pearson's ρ = 0.71) and a much lower root mean-squared error (RMSE) = 0.019 than the comparison to manual measurements.

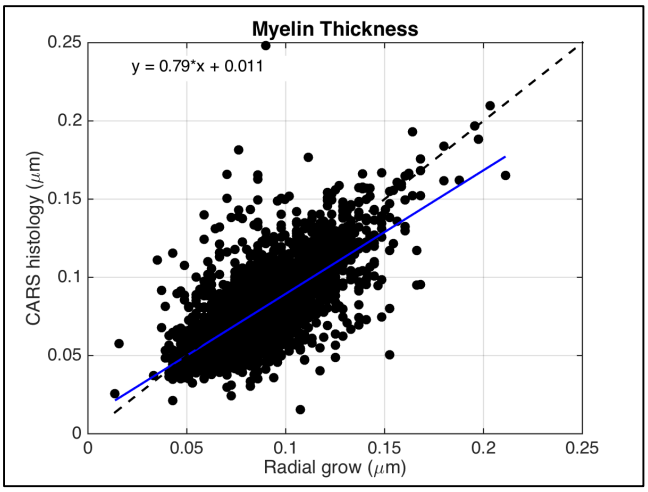

Figure 4.13. Myelin thickness from radial sampling and CARS histology techniques. Each point represents one axon.

From these analyses, we see that measures of Δ are much less robust than measures of axon diameter, due to its small size and blurry axon/myelin boundaries. However, if we use an automated technique, we can reduce the user-dependent error and assess each axon consistently.

4.4 MEASURING MYELIN VOLUME FRACTION ($f_{M,HIST}$)

4.4.1 Global Threshold

First, we wanted to assess the capability of a global threshold for segmentation of all electron microscopy images. To do this, a threshold was applied to each image based on the *nadir* of the histogram between the two peaks of myelin and non-myelin pixels. Since the myelin is stained, it is dark in the image and captured in the first signal peak as displayed below in Fig 4.14.

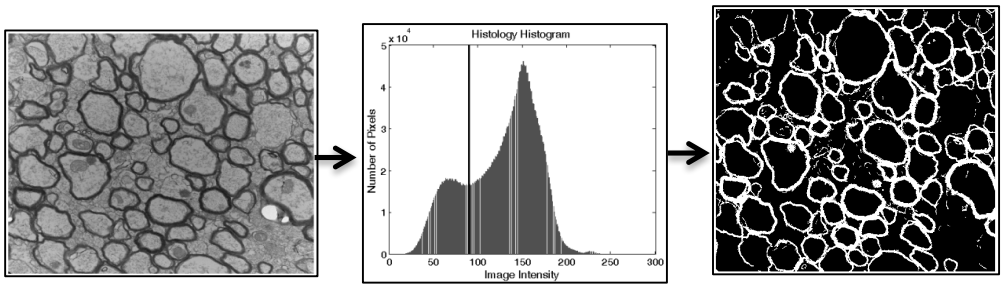

Figure 4.14. Flow chart to obtain a global threshold image using the intensity histogram *nadir*.

In the binary image, all pixels falling below the threshold = 1 and are considered myelin, while all pixels above the threshold = 0 and care onsidered non-myelin. From these binary images the $f_{M,HIST}$ was calculated as the number of pixels = 1 over the total number of image pixels. While this technique was a good start, it did not work consistently and needed manual correction often.

We also assessed other global thresholding techniques: Manual (as described above), Otsu (*multithresh*- 1 value; (10)), Reddi (*reddi;* (13)), Kittler (*kittler*) and Kittler 3-class (*kittlerMinimimErrorThresholding*; (14)), Otsu 3-class (*multithresh*- 2 values; (10)) and non-uniform-illumination-corrected Otsu (local Otsu- *adaptivethreshold* – described below). To qualitatively assess how different methods compared, I implemented a MATLAB GUI (*Threshold_segmentation*) shown in Fig 4.15. The GUI allows you choose an input image and displays the histogram of pixels in that image. You can then toggle between different threshold techniques. The GUI will display the threshold on the histogram and in value form below, the segmented imaged, and $f_{M,HIST}$ calculated. There is also a toggle for a built in bias field correction method (15) and the ability to remove stray pixels from the threshold image based on user-defined minimum number of connected pixels (*bwareaopen*). A screenshot of the GUI is displayed below using the Kittler 3-class technique.

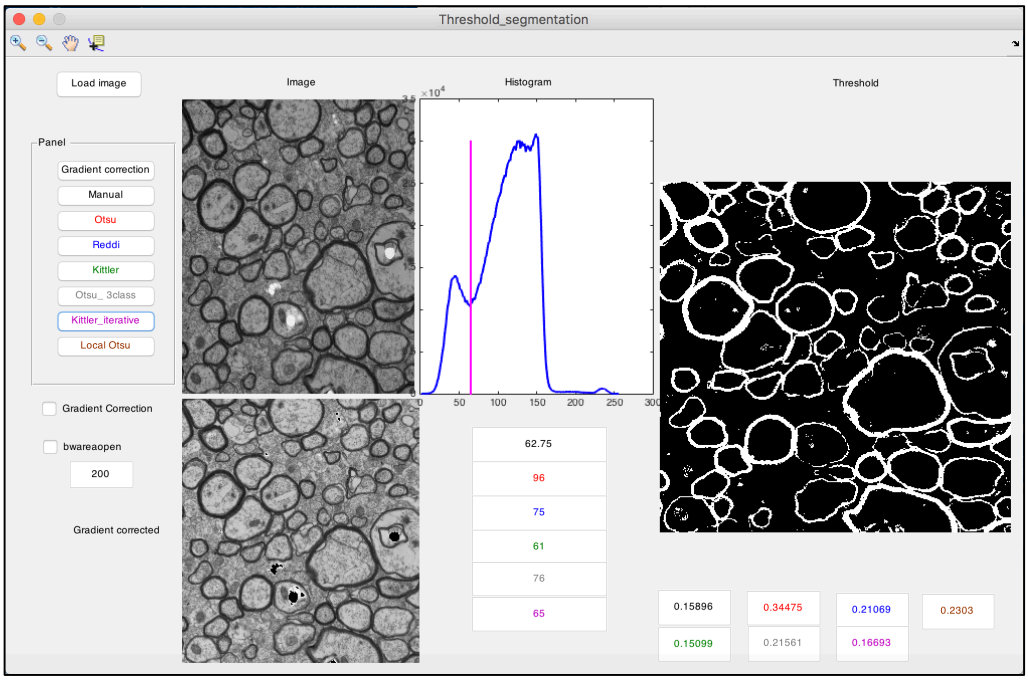

Figure 4.15. Demonstration of threshold segmentation GUI. The graphical user interface allows users to assess the ability of various threshold techniques to properly segment myelin.

While there are many techniques for global thresholding, in the end no global technique was consistent for all different images. Some images displayed non-uniform illumination, which made it difficult to find a global threshold value. Others (especially images from diseased mouse brain) had very little myelin, which created a nearly indiscernible peak from myelin tissue, which also created a challenge to find the correct threshold value globally.

4.4.2 Local Threshold

As opposed to global thresholding, local threshholding allows for correction from non-uniform illumination across the image. We used a local correction followed by 2-class Otsu method as displayed in Fig 4.16 below (*adaptivethreshold*; (10)). This approach calculates the mean pixel intensity using an averaging filter (*fspecial('average', pixelsize)*) across the user-defined pixel window region resulting in a smooth mean intensity image (mIM). We then subtract mIM from

the image to get an inverted uniform image. It is important that the pixel window region is large enough to contain image features and some background pixels but retain local changes in the image (pixel region = 500, displayed on the raw image). The mean subtraction allows for correction of background gradients in the image, exemplified in Fig 4.16 . Then, a 2-class global Otsu threshold is applied resulting in a binary image (myelin=1, non-myelin=0). In Fig 4.17 the comparison between the global Otsu method and the locally-corrected Otsu method is displayed, with more uniform segmentation using the local method.

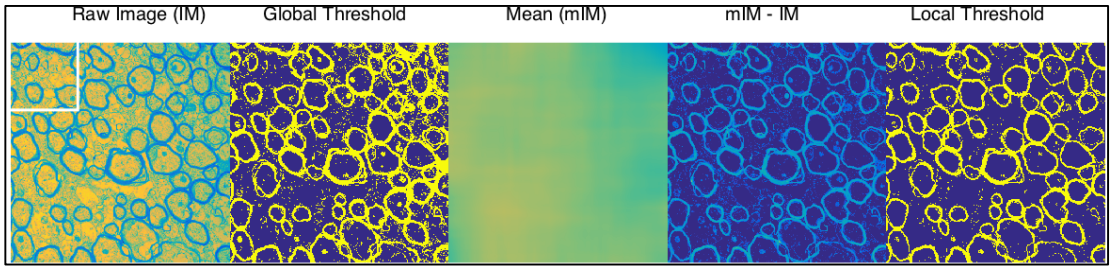

Figure 4.16. Demonstration of local Otsu threshold segmentation. A mean intensity value is defined for each pixel from a moving window average. The image intensity is subtracted from mean background intensity and global Otsu is used to segment myelin with a uniform background.

4.4.3 Radial Growing

While the local threshold performed more consistently than global techniques, we only used the local segmentation as a first pass for estimating myelin volume fraction. Overall, all threshold technqiues cannot distinguish between myelin and other dark, non-myelin features such as nuclei or other membranous structures. Instead, to obtain a more accurate value for $f_{M,HIST}$, we decided to use myelin measurements to create a segmented myelin image as described in section 4.3.2 to obtain a segmented myelin image.

4.4.4 Comparison of Methods

We assessed $f_{M,HIST}$ obtained from manual global threshold, local threshold and radial grow techniques. Figure 4.17 displays one example image using global, local and radial grow techniques. While all images qualitatively look similar, global threshold appears to non-uniformly depict myelin, with areas of myelin dropout. As expected, the local threshold more uniformly represents myelin but as stated above, non-myelin pixels are also incorporated into the segmentation. The radial grow technique displays a similar but much cleaner segmentation as it avoids the need for distinguishing myelin from non-myelin and is calculated on an axon-by-axon basis.

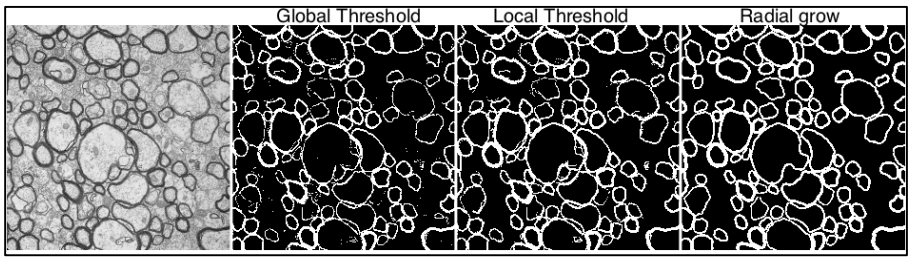

Figure 4.17. Demonstration of threshold segmentation methods. Global threshold suffers from non-uniforma illumination which is corrected using a local threshold. However, only the radial grow technique can consistently segment pure myelin.

Next, we quantitatively compared the three segmentation techniques image-by-image between control and 2 models of hypomyelination and 1 model of hypermyelination shown in Fig 4.18.

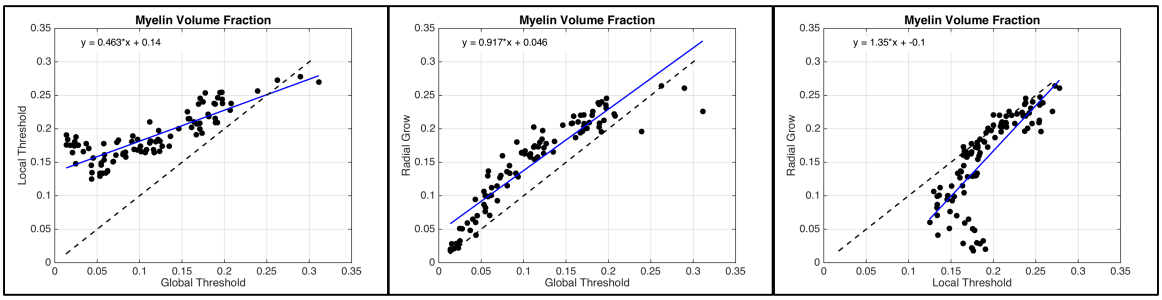

Figure 4.18. Comparison of $f_{M,HIST}$ from different threshold segmentation methods. Global threshold underestimates $f_{M,HIST}$. Local threshold overestimates $f_{M,HIST}$ due to non-myelin objects, especially in low $f_{M,HIST}$ images. Radial grow provides the most robust method for $f_{M,HIST}$.

From these comparisons, we see that —1) local threshold and region grow provides higher $f_{M,Hist}$ compared to global threshold in almost all cases, 2) global threshold and region grow are well correlated, and 3) local threshold and region grow are nearly identical except for cases where myelin content is very low. Observation #3 is demonstrated in Fig 4.19 below. While global threshold cannot distinguish all myelin pixels leading to lower $f_{M,HIST}$, local threshold finds extraneous pixels, leading to much higher $f_{M,HIST}$. Overall, radial grow technique provided the most consistent results using the positives from global and local threshold without the drawbacks.

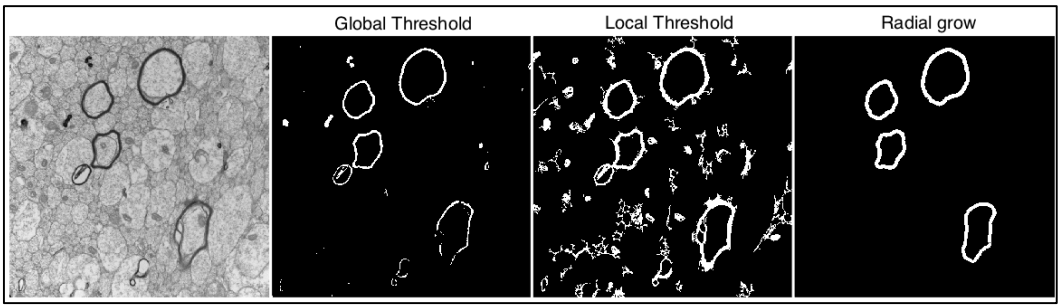

Figure 4.19. Comparison of $f_{M,HIST}$ from different threshold segmentation methods in hypomyelination model. Global threshold underestimates $f_{M,HIST}$, local threshold overestimates $f_{M,HIST}$ due to non-myelin objects, and radial grow provides the most robust method for $f_{M,HIST}$.

4.5 REFERENCES

1. Jelescu I, Zurek M, Winters K, et al. In vivo quantification of demyelination and recovery using compartment-specific diffusion MRI metrics validated by electron microscopy. Neuroimage 2016;132:104–14.

2. Stikov N, Campbell JS, Stroh T, Lavelée M, Frey S, Novek J, Nuara S, Ho M-K, Bedell BJ, Dougherty RF. In vivo histology of the myelin g-ratio with magnetic resonance imaging. NeuroImage 2015;118:397–405. doi: 10.1016/j.neuroimage.2015.05.023.

3. Dula AN, Gochberg DF, Valentine HL, Valentine WM, Does MD. Multiexponential T2, magnetization transfer, and quantitative histology in white matter tracts of rat spinal cord. Magnetic Resonance in Medicine 2010;63:902–9. doi: 10.1002/mrm.22267.

4. West K, Kelm N, Carson R, Does M. A revised model for estimating g-ratio from MRI. NeuroImage 2016;125:1155–8.

5. Meijering E. Cell Segmentation: 50 Years Down the Road . IEEE Signal Processing Magazine 2012;29:140–145. doi: 10.1109/MSP.2012.2204190.

6. Adams R, Bischof L. Seeded region growing. IEEE Transactions on pattern analysis and machine intelligence 1994;16:641–7.

7. Kass M, Witkin A, Terzopoulos D. Snakes: Active contour models. International Journal of Computer Vision 1988;1:321–31.

8. Ivins J, Porrill J. Everything you always wanted to know about snakes (but were afraid to ask). AIVRU Technical Memo 2000;83:1–35.

9. Xu C, Prince J. Snakes, shapes, and gradient vector flow. IEEE Transactions on image processing 1998;7:359–69. doi: 10.1109/83.661186.

10. Otsu N. A threshold selection method from gray-level histograms. IEEE Transactions on systems, man, and cybernetics 1979;9:62–6.

11. Leys C, Ley C, Klein O, Bernard P, Licata L. Detecting outliers: Do not use standard deviation around the mean, use absolute deviation around the median. Journal of Experimental Psychology 2013;49:764–6.

12. Bégin S, Dupont-Therrien O, Bélanger E, Daradich A, Laffray S, De Konick Y, Côt DC. Automated method for the segmentation and morphometry of nerve fibers in large-scale CARS images of spinal cord tissue. Biomedical Optics Express 2014;5:4145–61.

13. Reddi S, Rudin S, Keshavan H. An optimal multiple threshold scheme for image segmentation. IEEE Transactions on Systems, Man and Cybernetics 1984;14:661–5. doi: 10.1109/TSMC.1984.6313341.

14. Kittler J, Illingworth J. Minimum error thresholding. Pattern Recognition 1986;19:41–7.

15. Van Leemput K, Maes F, Vandermeulen D, Suetens P. Automated model-based bias field correction of MR images of the brain. IEEE Trasnactions on Medical Imaging 1999;18:885–96. doi: 10.1109/42.811268.

CHAPTER 5

MYELIN VOLUME FRACTION IMAGING WITH MRI

5.1 INTRODUCTION

There is a long-standing effort to develop MRI methods that are not just sensitive to myelin but report on changes in myelin with specificity. Recent interest in using MRI to measure the g-ratio (1–3) has raised the aims of myelin imaging a step further, beyond specificity to accuracy. That is, an ideal method for g-ratio imaging includes more than just a correlative measure of myelin content, but an absolute measure of myelin volume fraction (MVF). To date, two myelin imaging techniques have been particularly well studied: myelin water imaging (MWI) via multi-exponential T_2 (MET_2) analysis (4) and quantitative magnetization transfer (qMT) imaging (5). Both techniques have been shown to provide correlative measures of myelin content (6–9), but exactly how each relates to MVF remains unclear.

In the case of MWI, white matter is modeled as being comprised of two micro-anatomically separated water compartments with different transverse relaxation time constants (T_2): 1) water trapped between the lipid bilayers of myelin (myelin water, T_2 = 5 - 40 ms, depending on static field strength, B_0), and 2) water in both the intra- and extra-axonal spaces (i/e water, T_2 = 30-100 ms, depending on B_0). Given sufficient signal-to-noise ratio (SNR), multiple spin-echo amplitudes can be fitted to a model that distinguishes these water pools based on T_2, and the myelin water fraction (MWF) is typically reported as a measure of relative myelin content (4,10,11).

Measures of MWF have been shown to correlate with optical density in luxol fast blue stained sections of cadaver brain from MS patients (6) and with direct measures of myelin cross sectional area in electron microscopy of control and injured rat nerve (7,8). Also, Laule et al., used literature values of the composition of white matter to predict MWFs that were in close agreement with their observed values (12). However, none of these studies attempted to explicitly estimate and/or validate values of MVFs from MWF measures. The relationship between MWF and MVF depends on the relative water proton densities in the myelin and non-myelin compartments, but may also depend on the rate at which water exchanges between these compartments (13). Studies in rat spinal cord have indicated that variations in MWFs between different white matter tracts may be due to differences in water exchange rates, mediated by variations in axon diameter and myelin thickness (14,15). This effect has been postulated to exist in brain (16,17), but it remains unclear to what extent it effects observed MWF values.

Similar to MWI, the qMT method is based on a two-pool model of protons in white matter, but instead of two anatomically separated pools they are two pools of different molecular origins, water protons and protons bound to macromolecules. Although the bound proton signal is not typically measured directly, the exchange of magnetization between the bound and water protons results in contrast that depends on bound proton concentration (18,19). Thus, given an appropriate series of images with different MT contrast, the ratio of bound protons to total protons, or bound proton fraction (BPF), can be estimated. Note that, unlike the two-pool model used for MWI, this two-pool model: i) incorporates no anatomical information (both water and bound protons pools are assumed to be well mixed from one anatomical compartment, meaning that myelin is not explicitly part of the model), and ii) is predicated on the exchange of magnetization between the two pools (while the MWI model assumes no exchange of

magnetization between the two water pools) (5,20). The lack of anatomy in the model presents a problem in relating BPF to MVF because bound protons will exist in both myelin and non-myelin regions of the tissue, and there is no reason to believe that all bound protons exchange magnetization with water at the same rate. As in MWI, this raises the question of whether geometric characteristics of axons/myelin contribute to the measured BPF.

Similar to literature on MWF, measures of BPF (or similar/related quantities) have been demonstrated to linearly correlate with MVF as measured by histology in both human cadaver brain (9)and rodent brain and nerve (8,21–23). Stikov et al. have recently used such a linear correlation to estimate MVF from BPF (2), but otherwise, there has been limited effort in explicitly estimating MVF from estimates from qMT measures.

Using literature information on the composition of white matter, this study proposes analytical expressions for computing estimates of MVF from MET_2 and qMT data. These approaches are applied with high resolution 3D MRI protocols to excised and fixed mouse brains from control mice and three mouse models of abnormal myelination. MRI results are quantitatively evaluated with transmission electron microscopy.

5.2 THEORY

To derive myelin volume measures from MRI, a model of white matter tissue that uses volumes, not just populations, of the different proton pools is presented in Fig 5.1. The model includes four proton pools, with volumes of bound and water protons in the myelin ($V_{B,M}$ and $V_{W,M}$, respectively) and non-myelin ($V_{B,NM}$ and $V_{W,NM}$, respectively). The model assumes exchange of longitudinal magnetization between the bound and water protons, enabling qMT analysis, but no exchange of water or magnetization between myelin and non-myelin compartments.

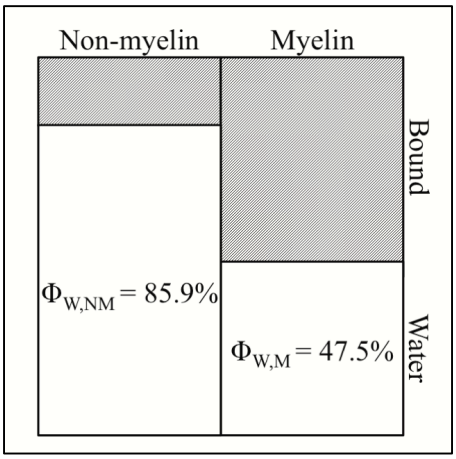

Figure 5.1. Volumetric model of white matter. Equations 5.8 and 5.12 are used to derive accurate myelin volume fractions ($f_{M,T2}$ and $f_{M,MT}$) from MWF and BPF, respectively.

The MVF (f_M) by definition is

$$f_M = \frac{V_{B,M} + V_{W,M}}{V_{B,NM} + V_{W,NM} + V_{B,M} + V_{W,M}}. \quad [5.1]$$

Using the simplifying assumption that molar concentration of protons is equal in all four compartments (see 5.7 Appendix), magnetization fractions are equal to volume fractions, which permits BPF measured by qMT to be expressed in terms of compartment volume fractions,

$$BPF = \frac{V_{B,NM} + V_{B,M}}{V_{B,NM} + V_{W,NM} + V_{B,M} + V_{W,M}}. \quad [5.3]$$

Similarly, the myelin water fraction (MWF) measured by MET_2 is

$$MWF = \frac{V_{W,M}}{V_{W,NM} + V_{W,M}} \quad [5.4]$$

From previous literature (see 5.7 Appendix), the volume fraction of water in myelin ($\Phi_{W,M}$) is estimated as

$$\Phi_{W,M} = \frac{V_{W,M}}{V_{B,M} + V_{W,M}} = 0.475 \frac{\text{ml } H_2O}{\text{ml tissue}}, \quad [5.5]$$

and for non-myelin is

$$\Phi_{W,NM} = \frac{V_{W,NM}}{V_{B,NM} + V_{W,NM}} = 0.859 \frac{\text{ml } H_2O}{\text{ml tissue}} \quad [5.6]$$

Combining Eqs 5.1, and 5.4-5.6, MWF can be written in terms of f_M

$$\text{MWF} = \frac{\Phi_{W,M} \times f_M}{\Phi_{W,NM} \times (1 - f_M) + \Phi_{W,M} f_M}. \quad [5.7]$$

which can then be solved to write f_M as a function of MWF,

$$f_{M,T2} = \frac{MWF \times \Phi_{W,NM}}{MWF \times \left(\Phi_{W,NM} - \Phi_{W,M}\right) + \Phi_{W,M}}, \quad [5.8]$$

with the additional "T2" subscript indicating that this is myelin volume fraction as estimated by MET_2 analysis.

For qMT analysis, there is an additional unknown: the volume fraction of the non-myelin bound proton pool, defined here as β.

$$\beta = \frac{V_{B,NM}}{V_{B,NM} + V_{W,NM} + V_{B,M} + V_{W,M}}. \quad [5.9]$$

Assuming that β were known, and from Eq 5.3,

$$\left[BPF - \beta\right] = \frac{V_{B,M}}{V_{B,NM} + V_{W,NM} + V_{B,M} + V_{W,M}}, \quad [5.10]$$

then combining Eqs 5.5 and 5.10, results in

$$\frac{V_{\mathrm{W,M}}}{V_{\mathrm{B,NM}}+V_{\mathrm{W,NM}}+V_{\mathrm{B,M}}+V_{\mathrm{W,M}}}=\frac{\Phi_{\mathrm{W,M}}}{1-\Phi_{\mathrm{W,M}}}\times\left[BPF-\beta\right]. \qquad [5.11]$$

The sum of Eqs 5.10 and 5.11 is the myelin volume fraction,

$$f_{\mathrm{M,MT}}=\left(1+\frac{\Phi_{\mathrm{W,M}}}{1-\Phi_{\mathrm{W,M}}}\right)\times\left[BPF-\beta\right], \qquad [5.12]$$

with the "MT" subscript indicating that this is myelin volume fraction as estimated by qMT analysis.

5.3 MATERIALS AND METHODS

5.3.1 Tissue Preparation

The Vanderbilt University Institutional Animal Care and Use Committee approved animal studies. Fifteen adult mice were anesthetized with isoflurane and sacrificed via transcardial perfusion. The perfusion consisted of 1X phosphate-buffered saline (PBS) wash followed by 2.5% glutaraldehyde + 2% paraformaldehyde (modified Karnovsky solution). Following perfusion, brains were quickly removed from skull and immersed in the fixative solution for 1 week. Brains were then washed with 1X PBS + 0.01% sodium azide, changing wash 4-5 times over 1 week to remove excess fixative. In all cases, 1.0 mM Gd-DTPA (Magnevist; Berlex, Montville, NJ) was included in the perfusate, immersion and wash solutions, resulting in relatively uniform distribution of Gd-DTPA throughout the brain.

This study used control animals (n=6) along with two previously described models of hypomyelination and one of hypermyelination (n = 3 for each model). All models utilized the *Olig2-Cre* driver to conditionally target proteins involved in PI3K/Akt signaling in

oligodendrocyte precursor cells. In the first model, the *Tsc2* gene is deleted (*Tsc2 CKO*–conditional knockout) and exhibits extreme loss of myelin (24). The second model targets *Rictor* (*Rictor CKO*), a key component of the mTORC2 complex, and also displays hypomyelination, but less severe than the *Tsc2* model and similar to the *Rictor* Emx1-Cre model shown previously (25). The third model results from the deletion of *Pten* (*Pten* CKO) leading to activation of the PI3K/Akt signaling pathway and subsequent hypermyelination (26).

5.3.2 Magnetic Resonance Imaging

All imaging was performed on a 15.2-T 11-cm horizontal bore Bruker (Rheinstetten, Germany) BioSpec scanner, using a 35-mm diameter Bruker quadrature volume coil for transmission and reception. To provide a signal-free background and prevent tissue dehydration, brains were placed in am MR-compatible tube filled with perfluoropolyether liquid (Fomblin, Solvay Solexis, Thorofarem NJ, USA). Both MET_2 and qMT scans were encoded with a matrix size of $128 \times 96 \times 72$ over a $1.92 \times 1.44 \times 1.08$ cm^3 FOV, providing 150 μm isotropic resolution.

For MET_2 imaging, a 3D multiple spin-echo sequence was used with non-selective excitation and refocusing pulses, 160 μs and 100 μs in duration, respectively. Each refocusing pulse was surrounded by 428 μs duration 6 G/cm amplitude crusher gradients, phase-encoding gradients were rewound after each echo, and a two-part (+X/-X) phase cycling scheme was used. With these constraints, secondary echoes that were not excited by the initial excitation pulse were removed, and the observed echo magnitudes could be computed with the extended phase graph (EPG) algorithm (27–29). Scan parameters were: repetition time (T_R) = 520 ms, echo time (T_E) = 5.8 ms, number of echoes (N_E) = 18, receiver bandwidth (BW) = 38.5 kHz, and number of excitations (N_{EX}) = 6. Total scan time was ≈ 6 hr.

For qMT imaging, a 3D selective inversion-recovery prepared fast spin echo sequence (20) was used with 8 collected echoes, 5-ms echo spacing and centric phase encoding. To ensure that the longitudinal magnetization (M_z) recovered from $M_z = 0$ at the start of every pre-delay period, 8 additional refocusing pulses, also with 5-ms echo spacing, followed the 8th echo. A 1-ms hard pulse was used to selectively invert the free water magnetization, while macromolecular spins were mostly unaffected. The sequence was repeated $N_I = 15$ times with inversion times (T_I) log-spaced from 3.5 to 2000 ms. A constant predelay (T_d) of 590 ms resulted in a scan time of ~ 3.5hr.

5.3.3 Data Analysis

All data analysis was performed using MATLAB R2015a (The Mathworks, Natick MA) and MET_2 analyses were performed using the freely available Multi Exponential Relaxation Analysis (MERA) toolbox (30). Prior to Fourier reconstruction, k-space data for all images were apodized using a 3D Tukey window with a 0.25 taper-to-window ratio and zero-padded 2×, resulting in 75μm nominal isotropic resolution.

For each voxel, the MET_2 analysis used a separable non-linear approach. The T_2 spectrum was estimated by linear inverse (31) using a non-negative least-squares fit (32) of the N_E echo magnitudes to the sum of 100 EPG-defined signals with T_2 values logarithmically spaced between $T_E/2$ as 500 ms. The linear model was augmented with minimum curvature constraint weighted at a constant and conservative level across all voxels ($\mu = 0.002$). This linear inverse was repeated to find the refocusing pulse flip angle (θ) by non-linear regression, similar to previous work (28,33). From all spectra, the myelin water fraction (MWF) was defined as the

fraction of signal with T_2 < 17 ms, based on previous work (see Chapter 3) and long T_2 component was defined as the T_2 from the largest fractional component > 17ms.

For qMT analysis, the N_I image magnitudes were fitted voxel-wise to the Bloch-McConnell equations describing longitudinal relaxation and magnetization transfer between water and macromolecular protons (20,34). The five fitted model parameters were: M_{0f}, M_{0b}, k_{mf}, R_{1f}, and S_f, where $M_{0f/b}$ are the equilibrium magnetizations of the free and bound pools, respectively, k_{bf} is the rate constant of magnetization transfer from the bound to free water pool, R_{1f} is the longitudinal relaxation rate of the free water pool, and S_f is the efficiency of the inversion pulse on the free water pool. The corresponding R_{1b} and S_b values were constrained to R_{1b} = 1s and S_b = 0.83 in accord with prior studies (20). The bound proton fraction (BPF) was then defined as BPF = M_{0b} / (M_{0b} + M_{0f}).

After MET_2 and qMT analysis, all parameter maps of a given model were co-registered in order to define closely comparable regions of interest (ROI) in each brain. For each mouse model, the first spin echo image of one brain was arbitrarily defined as the reference and the corresponding image from each other brain was registered to the reference using a rigid affine registration followed by a non-rigid deformable demons registration (35). The resulting deformation fields of this registration were then applied to parameter maps. Four ROIs were drawn corresponding to the four regions extracted for histology (below): 3 in the corpus callosum in the mid-sagittal slice (genu (GCC), mid-body (MidCC), and splenium (SCC)) and the other in the anterior commissure (AC). In addition, a cortical gray matter (GM) ROI was drawn in the sagittal slice for comparison. Each ROI was ~12.5voxels/ROI (~450 x 450 μm or 202.5 mm^2), which is similar to histologic ROIs and the ROI for each region was held constant

across brains. Mean ROI values from different parameter maps and values derived from histology were compared using two-sample *t*-tests ($\alpha = 0.05$) and Pearson's linear correlation.

5.3.4 Microscopy

For each brain, after MRI, a 1-2 mm thick sagittal section of tissue was cut from the left hemisphere beginning at the mid-brain. Subsequently, 4 regions of white matter were cut from the slice: the genu, mid-body, and splenium of the corpus callosum and the anterior commissure. Tissue samples were then processed for Transmission Electron Microscopy (TEM) in the Vanderbilt Cell Imaging Shared Resource-Research Electron Microscopy facility. Samples were placed in 1% osmium tetroxide in cacodylate buffer for 12 hours and dehydrated in graded ethanol. Tissue was then embedded in epoxy resin and thick sections (0.5-1 μm) were collected and stained with 1% toluidine blue. Subsequently, ultra-thin sections (~ 500 x 500 x 0.07 μm, see Fig 5.2b) were cut and collected on 300-mesh copper grids. Copper grids were stained at room temperature with 2% uranyl acetate (aqueous) for 15 minutes and then with lead citrate for 10 minutes.

Ultra-thin sections were imaged on the Philips/FEI Tecnai T12 electron microscope (FEI Company, Hillsboro, OR) at various magnifications and pictures were acquired with a side-mounted AMT CCD camera. For quantification of myelinated axon microstructure, 6-12 15,000× images were collected (~300 axons) per ROI per animal. Each image was analyzed semi-automatically to derive myelin volume fraction ($f_{M,HIST}$), axon volume fraction ($f_{A,HIST}$), as well as per axon measures of diameter (d_i) and myelin thickness (Δ_i) (subscript "i" indicating the i^{th} axon).

The histology pipeline was implemented using MATLAB 2015a (The Mathworks, Natick MA) and is shown in Fig 5.2. First, a local Otsu threshold was applied to each image, resulting in a binary image (myelin=1, non-myelin=0). In this binary image, the operator manually identified an intra-axonal point of each myelinated axon and corrected the labeling of pixels that were deemed to be erroneously identified as myelin. Beginning from each manually identified seed point, an active contour algorithm (36) was used to segment each individual axon. The resulting image (Fig 5.2d) provided per axon measures of area and diameter (a_i and $d_i = 2*\sqrt{a_i/\pi}$, respectively, for the i^{th} axon) and total axon volume fraction. (Note that only axons lying fully within the image frame were included in the per-axon measures, but all axon area contributed to the axon volume fraction.)

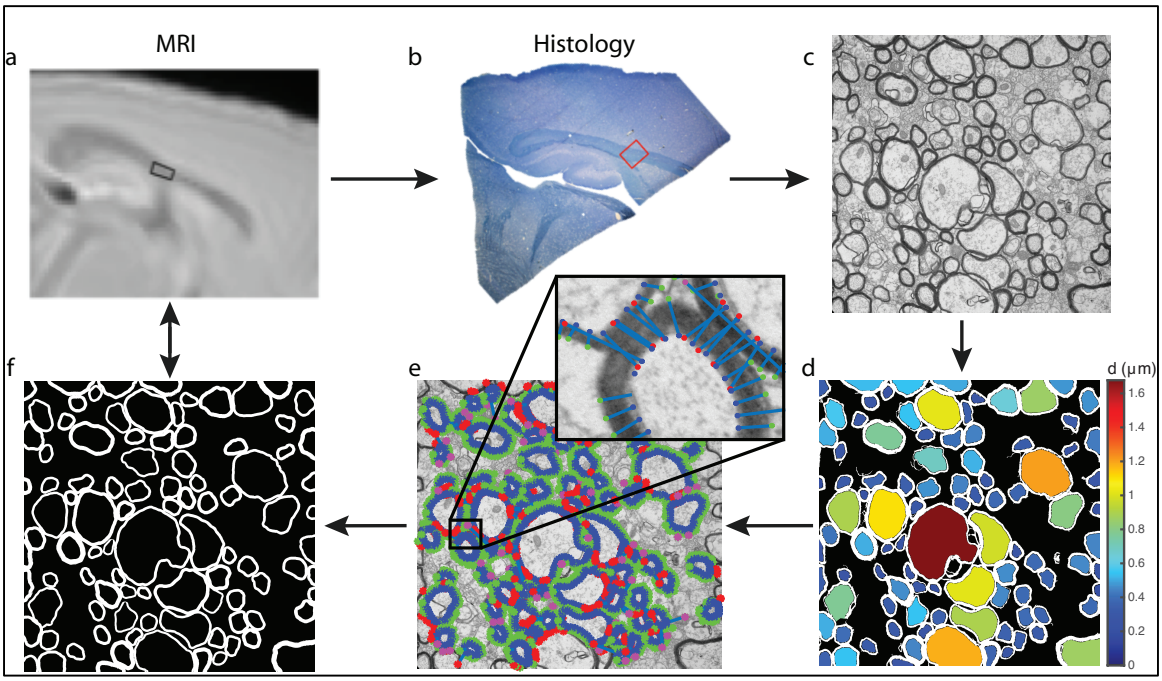

Figure 5.2. Histology flow chart. a) MRI T_2-weighted image with box drawn for ROI analysis. b) Histology thick slice where the red box signifies the location of ultra-thin sections. c) Transmission Electron Microscopy (TEM) 15,000X image. d) Output of region-growing algorithm with colorbar denoting axon diameter (d), and the fraction of area from all axons = $f_{A,HIST}$. e) For each axon, normal lines are grown from seeds from the region-growing axon edge (blue stars) until the image value is less than the mean image value in seeds to obtain a measures of myelin thickness (green stars). The measurement is disregarded if i) the end point lands in another axon space (red stars) or ii) if the line is > 3 times median absolute deviation (magenta stars). A median myelin thickness is calculated for each axon. f) Myelin is then grown using the median thickness from the region-growing axon boundary to obtain a segmented myelin image, with the fraction of area from all myelin = $f_{M,HIST}$.

Because the Otsu threshold resulted in uneven segmentation of the myelin, the myelin of each myelinated axon was independently segmented on the original histology image using the final boundary of the axon segmentation as the starting contour. Each contour was grown outward along lines normal to its tangent (lines spaced ~0.06 µm apart along the starting contour) until reaching a pixel intensity greater than the average intensity of pixels from the initial contour (Fig 5.2e). In order to reject normal lines that grew into the myelin of adjacent axons, a line was discarded if 1) its terminal point matched the location of an axon boundary defined above, or 2) its length was more than 3 times the median absolute deviation (37). The ends of the remaining

normal lines created a contour defining the outer myelin boundary, and the median length of these lines defined the myelin thickness for that axon, Δ_i. Finally, myelin area for each axon was determined by uniformly growing the initial contour of each axon to a uniform thickness = Δ_i, as shown in Fig 5.2f. The resulting binary image provided a measure of myelin volume fraction, $f_{\mathrm{M,HIST}}$, for each image. Across all images per mouse and brain region, mean values $\overline{f_{\mathrm{M,HIST}}}$, $\overline{f_{\mathrm{A,HIST}}}$, $\overline{d}$, and $\overline{\Delta}$ were calculated.

5.4 RESULTS

Representative TEM histology in Fig 5.3 demonstrates the abnormal myelination characteristics expected from these mouse models of tuberous sclerosis. The *Rictor* CKO and especially the *Tsc2* CKO mice exhibited loss of myelinated axons, consistent with previous literature (24,25). Similarly consistent with literature (26), the myelin in *Pten* CKO mice was noticeably thicker than in control mice. These variations in both myelin content and myelin thickness made these a useful combination of models for evaluating the specificity of MRI methods for reporting on myelin volume fraction.

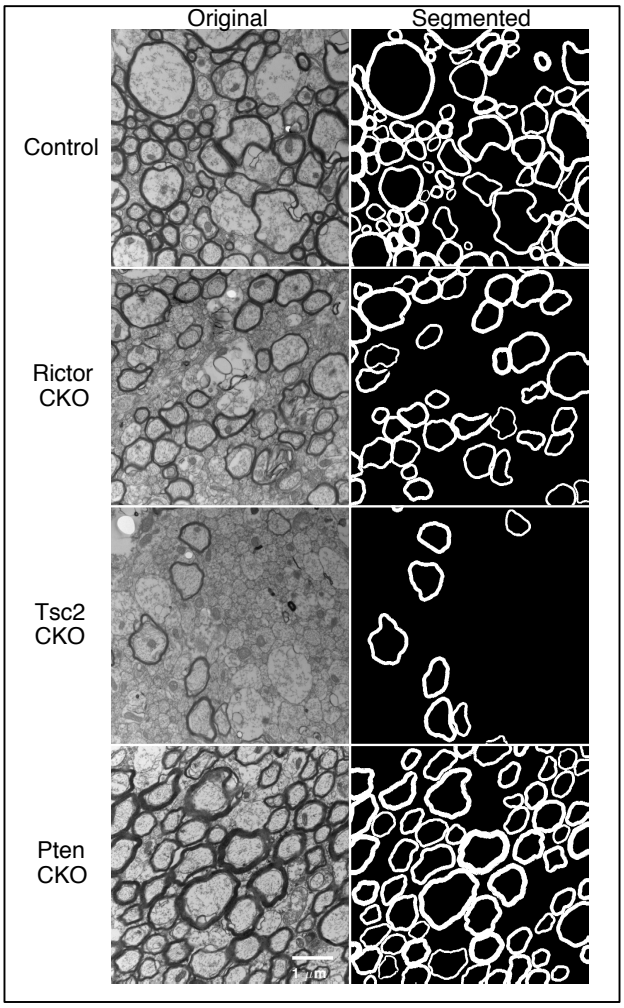

Figure 5.3. Representative histology images. Representative 15,000X (left) TEM Histology images and (right) segmented myelin images from (top-bottom) control, *Rictor CKO*, *Tsc2* CKO, and *Pten* CKO mice with scale bar = 1 μm.

A summary of the detailed quantitative evaluation of the TEM histology is presented in Fig 5.4. The mean ± SD (across animals) of three metrics ($\overline{f_{\mathrm{M,HIST}}}$, $\overline{f_{\mathrm{A,HIST}}}$, and $\overline{\Delta}$) are shown for each of the four white matter tracts and all four different mouse models. As expected from Fig 5.3, $f_{\mathrm{M,HIST}}$ is significantly reduced in both *Rictor* and *Tsc2* CKO compared to controls, and slightly higher in the SCC and AC regions of the *Pten* mice. Measures of $f_{\mathrm{A,HIST}}$ were similar between control, *Rictor*, and *Pten* CKO mice, but dramatically reduced in *Tsc2* CKO mice,

(although it is worth noting that the *Tsc2* histology did exhibit a large fraction of non-myelinated axons, but due to their small size are difficult to quantify accurately). The control and *Rictor* CKO mice showed similar myelin thickness, while $\overline{\Delta}$ was generally greater in Tsc2 CKO *Pten* CKO mice.

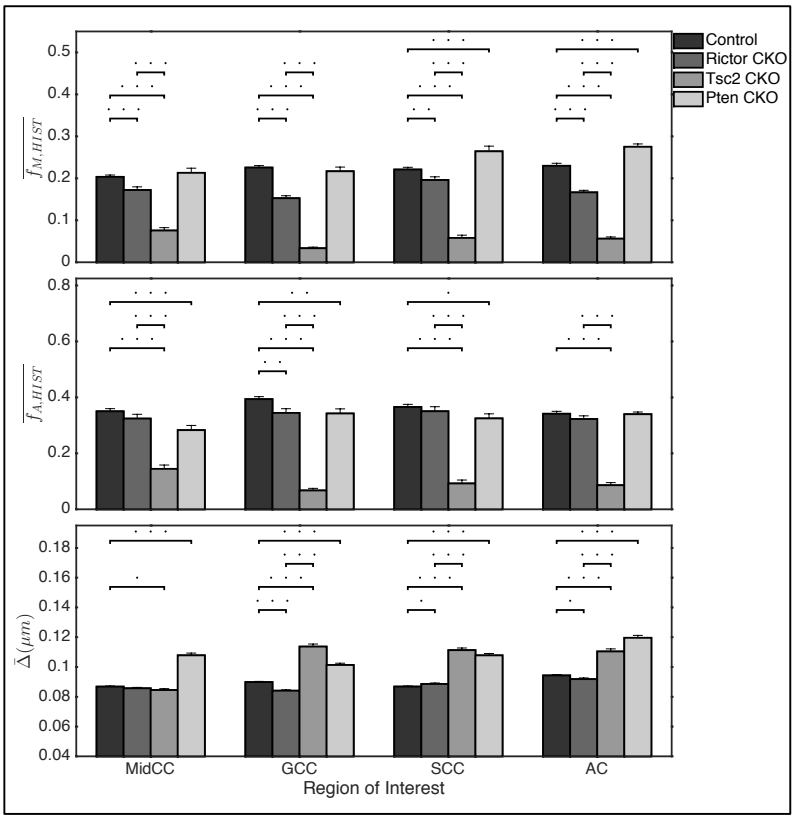

Figure 5.4. Region of interest (ROI) histology analysis. (top-bottom) mean myelin volume fraction ($f_{M,HIST}$), mean axon volume fraction ($f_{A,HIST}$), and mean myelin thickness (Δ) from (left-right) mid-body of corpus callosum (MidCC), genu of corpus callosum (GCC), splenium of corpus callosum (SCC), anterior commissure (AC) and cortical gray matter (GM) in control, *Rictor CKO*, *Tsc2* CKO, and *Pten* CKO mice. Dots above bars represent significant differences of (.) = $p < 0.05$, (. .) = $p < 0.01$, (…) = $p < 0.001$.

Representative MRI data from control and the three mouse models are shown in Fig 5.5—sagittal slices from a T_2-weighted image (T_E = 5.8 ms), long T_2 component value, MWF, and BPF parameter maps. As expected from histology (Fig 5.3 and 5.4), white matter regions are generally invisible in *Tsc2* CKO mice, reduced in contrast in *Rictor* CKO mice, and enhanced in

contrast in *Pten* CKO mice. A detailed summary of MRI measures is presented in Fig 5.6, which shows mean values (±SD across animals) of the long T_2, MWF, and BPF for controls, *Rictor*, *Tsc2*, and *Pten* CKO mice in the 4 white matter ROIs and the cortical gray matter ROI. Statistically significant differences in T_2, MWF, and BPF were found between controls and both models of hypomyelination (*Rictor* and *Tsc2* CKO), consistent with the loss of myelin observed by histology. Between the *Rictor* and *Tsc2* CKO mice, differences in all measures were consistent with less myelin in the *Tsc2* CKO mice, but only reached statistical significance for BPF in 3 of 4 ROIs and in 1 for MWF. Similarly, the *Pten* mice, expected to exhibit hypermyelination, had generally increased MWF and BPF and decreased T_2, although the BPF and T_2 differences were only statistically significant in the AC.

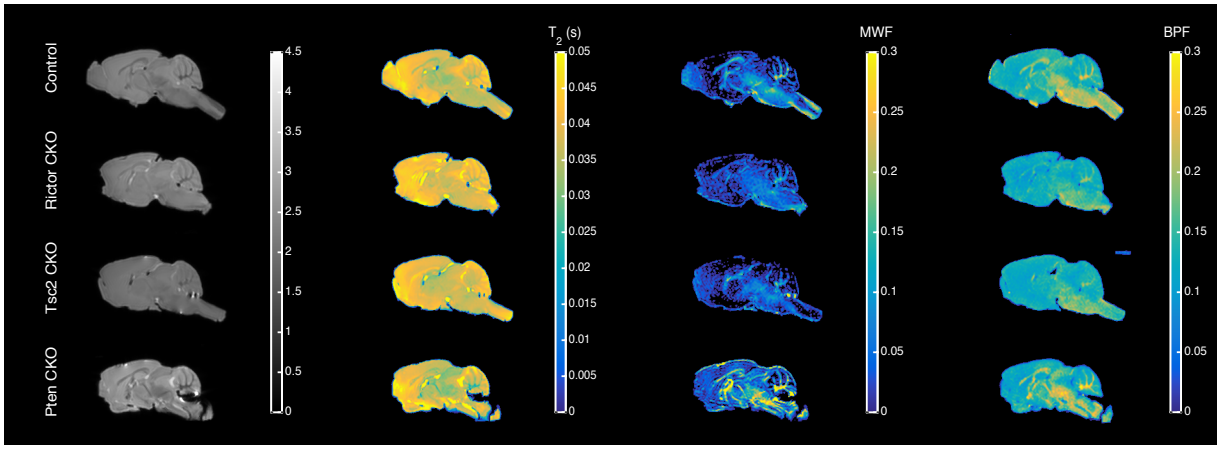

Figure 5.5. Representative MRI images. (left-right) T_2-weighted, long T_2 component, myelin water fraction (MWF), and bound pool fraction (BPF) parameter maps from (top-bottom) control, *Rictor CKO*, *Tsc2* CKO, and *Pten* CKO mice.

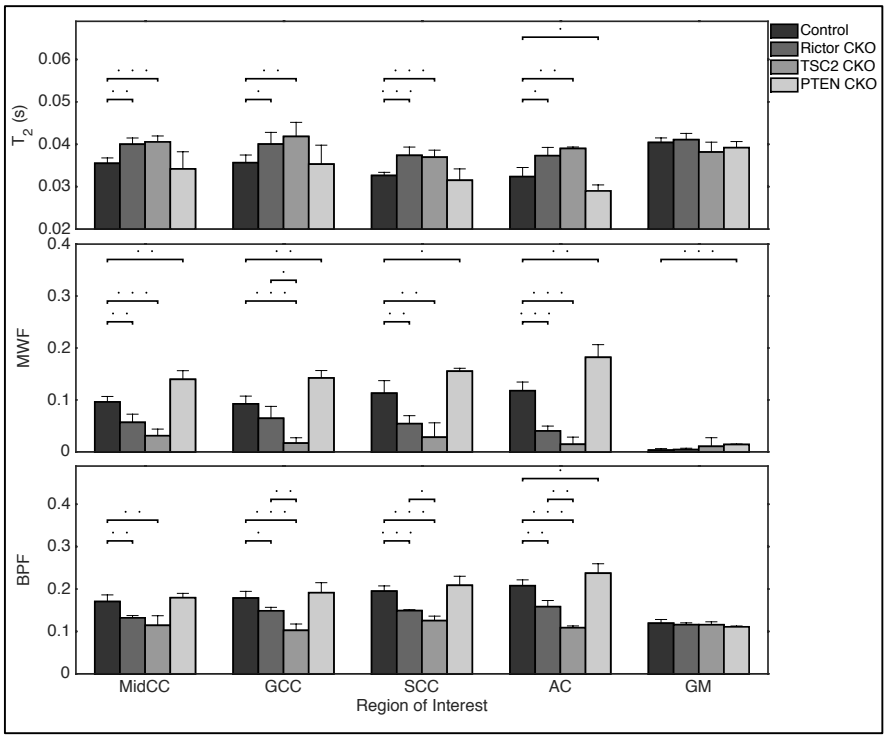

Figure 5.6. Region of interest (ROI) MRI analysis. (top-bottom) long T_2 component, myelin water fraction (MWF), and bound pool fraction (BPF) from (left-right) mid-body of corpus callosum (MidCC), genu of corpus callosum (GCC), splenium of corpus callosum (SCC), anterior commissure (AC) and cortical gray matter (GM) in control, *Rictor CKO*, *Tsc2* CKO, and *Pten* CKO mice. Dots above bars represent significant differences of (.) = $p < 0.05$, (. .) = $p < 0.01$, (…) = $p < 0.001$.

For the purpose of this study, more important than detecting differences in myelin between animals or brain regions, is the accuracy with which MRI can measure myelin content and how these measures are sensitive to myelin thickness. To this end, Fig 5.7 displays scatter plots of (top) MWF and BPF vs $f_{M,HIST}$. As expected from previous literature (6–9,22,23) both MWF and BPF show strong linear correlation with histological measures of MVF (r = 0.81, 0.84, respectively); however, neither measure is accurate (i.e., lines of best fit do not lie near line of unity). The offset in BPF (β) is also displayed visually and equals 0.086. Also shown in Fig 5.7 (bottom) are the two calibrated MRI measures of MVF, $f_{M,T2}$ and $f_{M,MT}$, vs $f_{M,HIST}$, which demonstrate the potential for both MET_2 and qMT to provide accurate, not just correlative (r =

0.82, 0.84 respectively), measures of MVF, with lines of best fit lying near the line of unity. Overall, $f_{M,T2}$ slightly underestimates $f_{M,HIST}$ and there is a noticeable variation between animal models, which may be due to the sensitivity of MET_2 to variations in myelin thickness. In contrast, the $f_{M,MT}$ estimates $f_{M,HIST}$ more accurately, although this is a somewhat misleading observation because the $f_{M,MT}$ data were calibrated at $f_{M,HIST} = 0$.

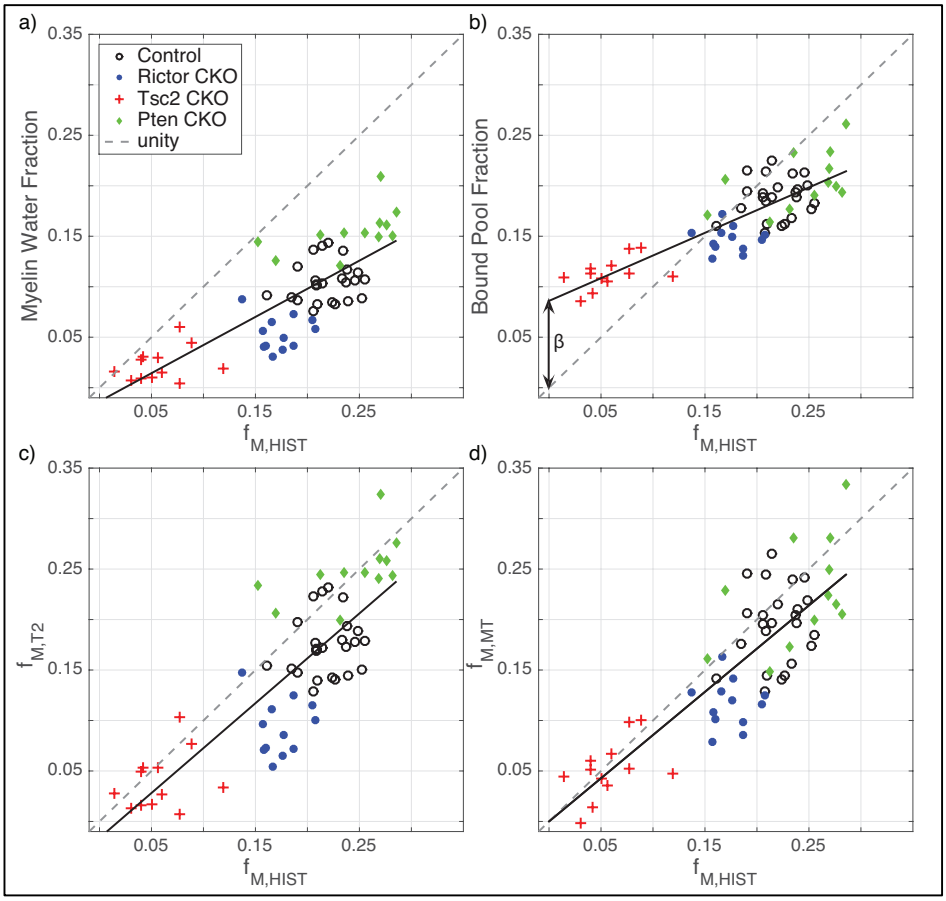

Figure 5.7. MRI versus histology scatter plots. (a,b) MWF and BPF versus $f_{M,HIST}$ with line of best fit and line of unity (gray, dashed). $r = 0.81$ and 0.84, respectively. Mean standard errors from MWF and BPF are 0.007 and 0.004, respectively. (c,d) $f_{M,T2}$ and $f_{M,MT}$ versus $f_{M,HIST}$ with line of best fit and line of unity (gray, dashed). $r = 0.82$ and 0.84, respectively.

5.5 DISCUSSION

For the purpose of establishing MRI methods for measuring MVF, this paper presents MRI data and quantitative histology acquired in excised and fixed mouse brains with normal and abnormal myelination. One of the current goals of the authors' lab is to develop robust MRI assays for routine use in rodent brain studies, and to that end the findings here demonstrate that both MET_2 and qMT methods have the potential to provide both specific and accurate whole brain maps of MVF.

Looking beyond excised tissues to *in vivo* imaging of animals or humans, there are a number of important factors to consider. Previous studies have investigated the effects of chemical fixation on qMT in post-mortem human tissues (38) and found differences in absolute values but similar predictive value of myelin content. Similarly, previous MET_2 studies have shown a close correspondence in the T_2 spectrum between fixed and in vivo human white matter (6) and between fixed (14) and in vivo (39) rat spinal cord. However, there is a noticeable absence of in vivo MET_2 data from rat or mouse brain in the literature and even evidence suggesting it cannot be measured (40). This limit may be due to SNR at the resolution necessary for rodent brain imaging, or it may reflect the consequences of more rapid water exchange between myelin and non-myelin compartments in these particular tissues at physiological temperatures in rats and mice. In addition to the tissues being excised and fixed, this study also utilized the addition of Gd-DTPA to boost SNR efficiency (41). To assess the effect of the Gd-DTPA on the MET_2 and qMT data, independent scans were run on a control brain that was prepared without the added Gd-DTPA. These scans required a longer T_R but were otherwise identical and resulted in similar (< 10% different, not shown) measures of MWF and BPF to those found in the Gd-DTPA loaded brains. Although this was not a thorough investigation, it indicated that loading the tissue with 1

mM Gd-DTPA had no more than small effects on the quantitative myelin measures, and presumably little effect on their relationships to myelin content.

The observations that MWF and BPF correlate strongly with histological measures of myelin content is not novel, having been demonstrated in several previous studies (6–9,22,23). However, it is worth noting that with the exception of a recent study of the corpus callosum in cuprizone-fed mice (23), previous studies that involved brain tissue, as opposed to peripheral nerve, made independent measures of myelin content by optical densitometry of luxol-fast-blue stained histology. Optical densitometry is a practical approach for measuring myelin content over large sections of histology, but it presents challenges with calibration. That is, relating a densitometry measure to MVF itself requires calibration and is sensitive to the extent and spatial uniformity of staining. The Thiessen study included measures akin to MVF and found a strong correlation with BPF, but their MRI measurements did not include MWF. Thus, the present study, which involved direct visualization of myelin and quantitative analysis of approximately 500 TEM images, is unique in providing objective measures of MVF in brain to compare with both MWF and BPF. The TEM analysis also provided measures of myelin thickness, which cannot be extracted from large field optical densitometry studies.

Of course, all histology suffers from changes in tissue during the embedding process, and small-field-of-view TEM presents the potential for sampling bias. In this study, total tissue shrinkage < 10% is expected (42,43), and errors in MVF result only from the difference in shrinkage between myelin and non-myelin regions. If we postulate that the extent of shrinkage in different compartments is proportional to water density, then the effect of tissue shrinkage on MVF may be just a few percent—small compared to the variance in $f_{M,HIST}$. The area of ultra-thin sections is on the order of our MRI ROIs (*See* Fig 5.2a,b) but for high-resolution analysis, we are

limited to sampling ~1% of the area. However, by one-way ANOVA across all control sections, we see that variance between brains and ROIs is significantly higher than within a region, suggesting there were minimal effects from sampling bias. Histology also relies on an accurate analysis technique, which has no standard and is quite challenging. While our method generally performed well, in cases of poorly defined myelin to non-myelin boundaries we chose to err on the side of slightly overestimating myelin.

In terms of evaluating and comparing the two MRI methods studied here—MET_2 and qMT—the most obvious difference is that the calculation of $f_{M,T2}$ required a priori information about the volume fractions of water in myelin and non-myelin compartments of white matter, while $f_{M,MT}$ required the same and a calibration value of BPF when MVF = 0, i.e., β in Eqs [5.9]-[5.12]. Here, β was estimated from the linear regression of BPF vs $f_{M,HIST}$ (Fig 5.7b), which makes the evaluation of $f_{M,MT}$ vs $f_{M,HIST}$ somewhat circular. Ideally, the value of β measured here will be applicable to future MRI studies of myelin in excised and fixed mouse brains at 15.2T, but how effectively one can generalize the intercept of BPF and $f_{M,HIST}$ is unclear. There is evidence that BPF changes between fresh and fixed tissue (38); it may also differ between *in vivo* and *ex vivo* tissue states, and perhaps between different white matter tracts and/or species. Moreover, even within a given type/state of tissue, the literature values of BPF vary widely, which is likely due to the wide variety of qMT methods in use.

Nonetheless, it may be possible to generalize the offset term, β, by normalizing white matter BPF values to those from cortical gray matter, which contains relatively little myelin. For example, in this study, the relative amplitude of β and BPF in cortical gray matter is 0.72, and similar ratios, 0.76 and 0.77, can be drawn from the data in two previous studies, Janve et al. (Janve et al. 2013) and Thiessen et al. (23), respectively. The Thiessen et al. study also involved

fixed excised mouse brains but a very different qMT protocol, suggesting that a standard β might work for these samples, independently of the qMT protocol. From rat brain *in vivo* (22), the results were somewhat different with a ratio of 0.62, but this is to be expected given a previous study that showed a greater relative effect of chemical fixation on BPF for normal appearing white matter and multiple sclerosis lesions (38). Nonetheless, this meta-analysis suggests potential for this approach to estimating β without histology driven calibration.

Unlike $f_{M,MT}$, $f_{M,T2}$ does not require an offset term because MWF goes to 0 in the absence of myelin. However, previous studies in rat spinal cord (14,15) and rat optic nerve (44) have shown that MWF may be affected by inter-compartmental water exchange. Thus, smaller axons with thinner myelin may result in lower MWF relative to the MVF. This phenomenon may be responsible for the systematic deviation between animal models from the overall linear fit in Fig 5.7c. That is, all data points from the *Pten* CKO mice, which exhibited generally thicker myelin, fall above the linear fit line, while 11 of 12 points from the *Rictor* CKO mice, which exhibited generally thinner myelin, fall below. This additional variance between models may also reflect differences in water densities in myelin and non-myelin regions ($\Phi_{W,M}$ and $\Phi_{W,NM}$), but the effect is the same—MWF is not simply a function of MVF. That said, the effect in this study is relatively small. It may be that *in vivo* and/or at lower magnetic fields (where transverse relaxation rates are slower and, therefore, more sensitive to the rate of water exchange) this effect is more significant and more problematic. While one might speculate that BPF should also be sensitive to the thickness of myelin, since macromolecular protons from deep within myelin may not exchange as effectively with the bulk intra-/extra-axonal water, the effect is not apparent in Fig 5.7d, which agrees with previous simulation studies (45).

Beyond MET_2 and qMT, there are a number of other MRI methods that aim to image myelin content, which raises the question of why the present study involved only MET_2 and qMT. Similar to MET_2, one can image myelin with multi-exponential T_2* which permits use of spoiled gradient echo rather than spin echo acquisitions at the cost of introducing a new unknown (the additional dephasing of transverse magnetization). While this approach shows promise (46–48) it is not at the point of providing accurate measures of MVF and, in the authors' experience, is especially challenging at the high magnetic fields used for small animal imaging. Other approaches that use steady state gradient echo are thus far uninterpretable at practical SNR, even for animal imaging (49).

Exploiting T_1 differences between myelin and non-myelin water to selectively excite only myelin water has been used in nerve (50) and white matter (40), but again, not for accurate MVF measures because additional unknowns come into play (T_1s and water exchange rates). Directly measuring multi-exponential T_1 has been proposed (51) but this is complicated not just by water exchange rates but also magnetization transfer. In fact, the qMT method used here is effectively a bi-exponential measurement of longitudinal relaxation. Because qMT already requires calibration, if the fast relaxing component is due to a combination of MT and multi-exponential T_1 (MET_1), there is no additional cost in specificity. However, attempting to interpret a bi-exponential recovery of longitudinal relaxation as being specifically a measure of myelin and non-myelin water pools will likely be inaccurate.

Finally, a few simpler approaches have also been proposed, such as a mono-exponential T_1 measurement (52) and measures of the proton density (53). These and similar approaches are essentially a sensitive but not specific measure of myelin, since numerous factors beyond MVF can alter their measurement. That said, from a practical perspective for human imaging, being

fast, reproducible, and quantitative measure has obvious advantages. For white matter imaging, the simplest model and, correspondingly, the greatest potential specificity comes from the proton density measurement. For example, in this study, integrating the T_2 spectrum and normalizing the amplitude to that of a cortical gray matter voxel results in a measure that correlates strongly with $f_{M,HIST}$ (Fig 5.8). An interesting feature of this method is that it will be independent of water exchange between myelin and non-myelin compartments. Indeed, variance in $f_{M,T2}$ between animal models seen above and attributed to water exchange (Fig 5.7c) is not apparent in Fig 5.8. In fact, considering a model where MVF is the only determinant of proton density variation in white matter, then a full T_2 spectrum with amplitude calibrated to a known water concentration provides enough information to estimate both MVF and water exchange rates, which may in-turn offer an alternative approach to measuring myelin thickness.

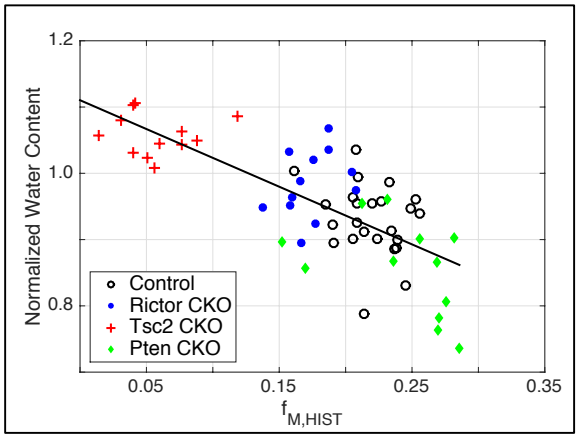

Figure 5.8. Normalized water content scatter plot. Normalized water content versus $f_{M,HIST}$ in control, *Rictor CKO*, *Tsc2* CKO, and *Pten* CKO mice, (r = -0.74).

5.6 CONCLUSION

Here, we assess MRI measures of myelin in control and 3 different models of white matter disease in mouse brain. Both MWF (from MET_2) and BPF (from qMT) show strong correlations

to quantitative histology. Using a volumetric model of white matter, MWF and BPF were converted to absolute measures of MVF, and displayed strong agreement with histologic myelin volume fraction. Using MET_2, MVF measures were derived independently from histology but may be affected by inter-compartmental water exchange depending on myelin microstructure. Using qMT provides a somewhat more accurate estimate of MVF that exhibits less dependence on other microstructure characteristics, but requires calibration, here using histology. This work also provides promise for quantification of g-ratio from MRI where obtaining absolute measures of MVF is important.

ACKNOWLEDGMENTS

The authors would like to thank Brittany Parker for assistance with tissue preparation; Vaibhav Janve for supporting data; Julien Cohen-Adad and Tanguy Duval for useful discussions relating to quantitative TEM analysis; and Janice Williams, Mary Dawes, and Maria Vinogradova for help with electron microscopy which was performed through the use of VUMC Cell Imaging Shared Resource (supported by NIH grants CA68485, DK20593, DK58404, DK59637 and EY08126).

5.7 APPENDIX

The relationship between equilibrium magnetization ($M_{0,x}$) and volume (V_x) for compartment x, is determined by the molar concentration of protons in each compartment, C_x,

$$\frac{M_{0,\mathrm{x}}}{V_x} = kC_{\mathrm{x}}, \qquad [5.A1]$$

where k is a constant converting mol ^{1}H to magnetization, C_x = molar concentration of pool x (mol ^{1}H / ml), and V_x = volume of pool x (ml). Further, the concentration, C_x, can be expressed as

$$C_x = \rho_x / \zeta_x \,, \qquad [5.A2]$$

where ρ_x = mass density of x (g/ml) and ζ_x = molar mass of ^1H in x (g/ mol ^{1}H).

For both water compartments, knowing $\rho_W = 1\ g_{H_2O}\ /\ ml_{H_2O}$, ζ_W is

$$\zeta_W = \frac{18.02\ \text{g}}{1\ \text{mol}\ H_2O} \times \frac{1\ \text{mol}\ H_2O}{2\ \text{mol}\ ^1\text{H}} = 9.01 \frac{\text{g}}{\text{mol}\ ^1\text{H}} \,, \qquad [5.A3]$$

and using ρ_W and ζ_W in Eq. 5.A2, C_W is

$$C_W = \frac{1\ \text{g}\ H_2O}{1\ \text{ml}\ H_2O} \times \frac{1\ \text{mol}\ ^1\text{H}}{9.01\ \text{g}\ H_2O} = 0.111\ \frac{\text{mol}\ ^1\text{H}}{\text{ml}\ H_2O} \,. \qquad [5.A4]$$

For the bound proton compartments, $C_{B,M}$ and $C_{B,NM}$, were considered to be the concentration of methylene protons in myelin and non-myelin compartments, respectively. These values were estimated by first estimating average values of $\zeta_{B,M}$, $\zeta_{B,NM}$, $\rho_{B,M}$ and $\rho_{B,NM}$. The average ζ, for each compartment was computed as the weighted average of molar proton masses of each of the most abundant lipids and proteins as,

$$\zeta_{B,x} = \sum_{i=1}^{n} w_{i,x} \times \zeta_i \qquad [5.A5]$$

where, x indicates either myelin or non-myelin, and n is the number of different molecules.

For example, cholesterol, [$C_{27}H_{46}O$], has 45 methylene protons and a molar mass of 386.65 g/mol, making the molar proton (methylene) mass of cholesterol $\zeta_{cholesterol}$ = 8.59 g/mol ^{1}H. In myelin and non-myelin, the dry mass fraction of cholesterol was estimated as, $w_{cholesterol,M}$

= 0.216 and $w_{cholesterol,NM}$ = 0.108, respectively. Similarly, ζ, $w_{i,M}$ and $w_{i,NM}$ were estimated for all constituent molecules as shown in Table 5.1 (54,55).

Table 5.2. Molar concentrations and mass fractions for constituents of myelin and non-myelin macromolecules.

Constituent	ζ_i (g/mol ^{1}H)	$w_{i,M}$	$w_{i,NM}$
Lipid		0.80	0.43
Cholesterol	8.59	0.216	0.108
Ganglioside	13.94	0.208	0
Phosphotidyl ethanolamine	9.75	0.160	0.095
Phosphotidyl choline	9.18	0.080	0.108
Phosphotidyl serine	10.51	0.068	0.043
Sphingomyelin	9.19	0.068	0.077
Protein		0.20	0.57
Myelin basic protein	20.64	0.075	0.214
Proteolipid protein	18.19	0.125	0.356

To calculate $\rho_{B,M}$ and $\rho_{B,NM}$, first, water mass fractions of myelin and non-myelin tissue ($w_{W,M}$ and $w_{W,NM}$) were converted to volume fractions ($\Phi_{W,M}$ and $\Phi_{W,NM}$) using literature values of ρ_W, ρ_M, and ρ_{NM} (12) as,

$$\Phi_{W,x} = w_{W,x} \times \frac{\rho_x}{\rho_W} \qquad [5.A6]$$

where x indicates either myelin or non-myelin.

Using ρ_M, ρ_{NM}, $\Phi_{W,M}$, and $\Phi_{W,NM}$, the mass densities of bound protons in myelin and non-myelin tissues ($\rho_{B,M}$ and $\rho_{B,NM}$, respectively) were determined from,

$$\rho_{B,x} = \frac{\rho_x - \left(\Phi_{W,x} \times \rho_{W,x}\right)}{\left(1 - \Phi_{W,x}\right)}\ , \qquad [5.A7]$$

where x indicates either myelin or non-myelin. Then, with $\zeta_{B,M}$, $\zeta_{B,NM}$, $\rho_{B,M}$ and $\rho_{B,NM}$, and Eq. 5.A2, $C_{B,M}$ and $C_{B,NM}$ are,

$$C_{\mathrm{B,M}} = \frac{\rho_{\mathrm{B,M}}}{\zeta_{\mathrm{B,M}}} = 0.095 \frac{\text{mol } ^1\text{H}}{\text{mL bound}}$$

$$C_{\mathrm{B,NM}} = \frac{\rho_{\mathrm{B,NM}}}{\zeta_{\mathrm{B,NM}}} = 0.090 \frac{\text{mol } ^1\text{H}}{\text{mL bound}} \qquad [5.A8]$$

Thus, the molar concentrations of ^{1}H in the macromolecule compartments of myelin and non-myelin (0.095, and 0.090 mol ^{1}H / ml, respectively) are estimated to be 15-20% lower than that of free water. For simplicity of modeling, we treat all four compartment molar proton concentrations as equal, making magnetization ($M_{0,\mathrm{x}}$) (and, therefore, signal) directly proportional to volume (V_{x}) (Eq [5.A1]).

5.8 REFERENCES

1. Stikov N, Perry L, Mezer A, Rykhlevskaia E, Wandell B, Pauly J, Dougherty R. Bound pool fractions complement diffusion measures to describe white matter micro and macrostructure. NeuroImage 2010;54. doi: 10.1016/j.neuroimage.2010.08.068.

2. Stikov N, Campbell JS, Stroh T, Lavelée M, Frey S, Novek J, Nuara S, Ho M-K, Bedell BJ, Dougherty RF. In vivo histology of the myelin g-ratio with magnetic resonance imaging. NeuroImage 2015;118:397–405. doi: 10.1016/j.neuroimage.2015.05.023.

3. West K, Kelm N, Carson R, Does M. A revised model for estimating g-ratio from MRI. NeuroImage 2016;125:1155–8.

4. Mackay A, Whittall K, Adler J, Li D. In vivo visualization of myelin water in brain by magnetic resonance. Magnetic Resonance in Medicine 1994;31:673–7. doi: 10.1002/mrm.1910310614.

5. Sled JG, Pike BG. Quantitative imaging of magnetization transfer exchange and relaxation properties in vivo using MRI. Magnetic Resonance in Medicine 2001;46:923–31. doi: 10.1002/mrm.1278.

6. Laule C, Leung E, Li D, Traboulsee A. Myelin water imaging in multiple sclerosis: quantitative correlations with histopathology. Multiple Sclerosis 2006;12:747–53.

7. Webb S, Munro C, Midha R, Stanisz GJ. Is multicomponent T2 a good measure of myelin content in peripheral nerve? Magnetic Resonance in Medicine 2003;49:638–45. doi: 10.1002/mrm.10411.

8. Odrobina E, Lam T, Pun T, Midha R. MR properties of excised neural tissue following experimentally induced demyelination. NMR in Biomedicine 2005;18:277–84. doi: 10.1002/nbm.951.

9. Schmierer K, Tozer DJ, Scaravilli F, Altmann DR, Barker GJ, Tofts PS, Miller DH. Quantitative magnetization transfer imaging in postmortem multiple sclerosis brain. Journal of Magnetic Resonance Imaging 2007;26:41–51. doi: 10.1002/jmri.20984.

10. Menon RS, Rusinko MS, Allen PS. Proton relaxation studies of water compartmentalization in a model neurological system. Magnetic Resonance in Medicine 1992;28:264–74. doi: 10.1002/mrm.1910280208.

11. Whittall K, Mackay A, Graeb D, Nugent R, Li DK, Paty D. In vivo measurement of T2 distributions and water contents in normal human brain. Magnetic Resonance in Medicine 1997;37:34–43. doi: 10.1002/mrm.1910370107.

12. Laule C, Vavasour I, Moore G, Oger J, Li D, Paty D, MacKay A. Water content and myelin water fraction in multiple sclerosis. Journal of Neurology 2004;251:284–93. doi: 10.1007/s00415-004-0306-6.

13. Zimmerman J, Brittin W. Nuclear Magnetic Resonance Studies in Multiple Phase Systems: Lifetime of a Water Molecule in an Adsorbing Phase on Silica Gel. The Journal of Physical Chemistry 1957;61:1328–33. doi: 10.1021/j150556a015.

14. Dula AN, Gochberg DF, Valentine HL, Valentine WM, Does MD. Multiexponential T2, magnetization transfer, and quantitative histology in white matter tracts of rat spinal cord. Magnetic Resonance in Medicine 2010;63:902–9. doi: 10.1002/mrm.22267.

15. Harkins K, Dula A, Does M. Effect of intercompartmental water exchange on the apparent myelin water fraction in multiexponential T2 measurements of rat spinal cord. Magnetic Resonance in Medicine 2012;67:793–800. doi: 10.1002/mrm.23053.

16. Sled JG, Levesque I, Santos AC, Francis SJ, Narayanan S, Brass SD, Arnold DL, Pike GB. Regional variations in normal brain shown by quantitative magnetization transfer imaging. Magnetic Resonance in Medicine 2004;51:299–303. doi: 10.1002/mrm.10701.

17. Russell-Schulz B, Laule C, Li D, MacKay A. What causes the hyperintense T 2-weighting and increased short T 2 signal in the corticospinal tract? Magnetic Resonance Imaging 2013;31:329–35.

18. Henkelman MR, Huang X, Xiang Q, Stanisz G, Swanson SD, Bronskill MJ. Quantitative interpretation of magnetization transfer. Magnetic Resonance in Medicine 1993;29:759–66. doi: 10.1002/mrm.1910290607.

19. Wolff SD, Balaban RS. Magnetization transfer contrast (MTC) and tissue water proton relaxation in vivo. Magnetic Resonance in Medicine 1989;10:135–44. doi: 10.1002/mrm.1910100113.

20. Gochberg DF, Gore JC. Quantitative magnetization transfer imaging via selective inversion recovery with short repetition times. Magnetic Resonance in Medicine 2007;57:437–41.

doi: 10.1002/mrm.21143.

21. Janve VA, Zu Z, Yao S-Y, Li K, Zhang FL, Wilson KJ, Ou X, Does MD, Subramaniam S, Gochberg DF. The radial diffusivity and magnetization transfer pool size ratio are sensitive markers for demyelination in a rat model of type III multiple sclerosis (MS) lesions. NeuroImage 2013;74:298–305. doi: 10.1016/j.neuroimage.2013.02.034.

22. Underhill HR, Rostomily RC, Mikheev AM, Yuan C, Yarnykh VL. Fast bound pool fraction imaging of the in vivo rat brain: Association with myelin content and validation in the C6 glioma model. NeuroImage 2011;54:2052–65. doi: 10.1016/j.neuroimage.2010.10.065.

23. Thiessen JD, Zhang Y, Zhang H, Wang L, Buist R, Bigio MR, Kong J, Li X, Martin M. Quantitative MRI and ultrastructural examination of the cuprizone mouse model of demyelination. NMR in Biomedicine 2013;26:1562–81. doi: 10.1002/nbm.2992.

24. Carson R, Kelm N, West K, Does M, Fu C, Weaver G, McBrier E, Parker B, Grier M, Ess K. Hypomyelination following deletion of Tsc2 in oligodendrocyte precursors. Annals of Clinical Translational Neurology 2015;2:1041–54. doi: 10.1002/acn3.254.

25. Carson RP, Fu C, Winzenburger P, Ess KC. Deletion of Rictor in neural progenitor cells reveals contributions of mTORC2 signaling to tuberous sclerosis complex. Human Molecular Genetics 2013;22:140–52. doi: 10.1093/hmg/dds414.

26. Harrington EP, Zhao C, Fancy SP, Kaing S, Franklin RJ, Rowitch DH. Oligodendrocyte PTEN is required for myelin and axonal integrity, not remyelination. Annals of Neurology 2010;68:703–16. doi: 10.1002/ana.22090.

27. Hennig J. Echoes—how to generate, recognize, use or avoid them in MR-imaging sequences. Part II: Echoes in imaging sequences. Concepts in Magnetic Resonance 1991;3:179–92. doi: 10.1002/cmr.1820030402.

28. Lebel MR, Wilman AH. Transverse relaxometry with stimulated echo compensation. Magnetic Resonance in Medicine 2010;64:1005–14. doi: 10.1002/mrm.22487.

29. Prasloski T, Mädler B, Xiang Q. Applications of stimulated echo correction to multicomponent T2 analysis. Magnetic Resonance in Medicine 2012;67:1803–14. doi: 10.1002/mrm.23157.

30. Does MD. Multi-Exponential Relaxation Analysis (MERA) Toolbox, Version 2, http://www.vuiis.vanderbilt.edu/~doesmd/MERA/MERA_Toolbox.html. 2014.

31. Whittall K, MacKay A. Quantitative interpretation of NMR relaxation data. Journal of Magnetic Resonance 1989;84:134–52. doi: 10.1016/0022-2364(89)90011-5.

32. Lawson, Hanson. Solving least squares problems. 1974.

33. McPhee KC, Wilman AH. Transverse relaxation and flip angle mapping: Evaluation of simultaneous and independent methods using multiple spin echoes. Magnetic Resonance in Medicine. 2016. doi: 10.1002/mrm.26285.

34. Li K, Zu Z, Xu J, Janve V, Gore J, Does M, Gochberg D. Optimized inversion recovery sequences for quantitative T1 and magnetization transfer imaging. Magnetic Resonance in Medicine 2010;64:491–500. doi: 10.1002/mrm.22440.

35. Thirion J-P. Image matching as a diffusion process: an analogy with Maxwell's demons. Medical Image Analysis 1998;2:243–60. doi: 10.1016/S1361-8415(98)80022-4.

36. Kass M, Witkin A, Terzopoulos D. Snakes: Active contour models. International Journal of Computer Vision 1988;1:321–31.

37. Leys C, Ley C, Klein O, Bernard P, Licata L. Detecting outliers: Do not use standard deviation around the mean, use absolute deviation around the median. Journal of Experimental Psychology 2013;49:764–6.

38. Schmierer K, Wheeler-Kingshott C, Tozer DJ, Boulby PA, Parkes HG, Yousry TA, Scaravilli F, Barker GJ, Tofts PS, Miller DH. Quantitative magnetic resonance of postmortem multiple sclerosis brain before and after fixation. Magnetic Resonance in Medicine 2008;59:268–77. doi: 10.1002/mrm.21487.

39. Harkins K, Valentine W, Gochberg D, Does M. In-vivo multi-exponential T 2, magnetization transfer and quantitative histology in a rat model of intramyelinic edema. NeuroImage: Clinical 2013:810–17. doi: 10.1016/j.nicl.2013.06.007.

40. Does MD, Gore JC. Compartmental study of T1 and T2 in rat brain and trigeminal nerve in vivo. Magnetic Resonance in Medicine 2002;47:274–83. doi: 10.1002/mrm.10060.

41. Johnson AG, Cofer GP, Gewalt SL, Hedlund LW. Morphologic Phenotyping with MR Microscopy: The Visible Mouse. Radiology 2002;222:789–93. doi: 10.1148/radiol.2223010531.

42. Tang Y, Nyengaard JR. A stereological method for estimating the total length and size of myelin fibers in human brain white matter. Journal of neuroscience methods 1997;73:193–200.

43. Denef JF, Cordier AC, Mesquita M, Haumont S. The influence of fixation procedure, embedding medium and section thickness on morphometric data in thyroid gland. Histochemistry 1979;63:163–71.

44. Dortch RD, Harkins KD, Juttukonda MR, Gore JC, Does MD. Characterizing inter compartmental water exchange in myelinated tissue using relaxation exchange spectroscopy. Magnetic resonance in medicine 2013;70:1450–59. doi: 10.1002/mrm.24571.

45. Levesque I, Pike G. Characterizing healthy and diseased white matter using quantitative magnetization transfer and multicomponent T2 relaxometry: A unified view via a four-pool model. Magnetic Resonance in Medicine 2009;62:1487–96. doi: 10.1002/mrm.22131.

46. Hwang D, Kim D, Du Y. In vivo multi-slice mapping of myelin water content using T 2* decay. Neuroimage 2010;52:198–204.

47. Lenz C, Klarhöfer M, Scheffler K. Feasibility of in vivo myelin water imaging using 3D multigradient-echo pulse sequences. Magnetic Resonance in Medicine 2012;68:523–8. doi: 10.1002/mrm.23241.

48. Alonso-Ortiz E, Levesque IR, Paquin R, Pike GB. Field inhomogeneity correction for gradient echo myelin water fraction imaging. Magnetic resonance in medicine 2016. doi: 10.1002/mrm.26334.

49. Lankford CL, Does MD. On the inherent precision of mcDESPOT. Magnetic Resonance in Medicine 2013;69:127–36. doi: 10.1002/mrm.24241.

50. Travis AR, Does MD. Selective excitation of myelin water using inversion-recovery-based preparations. Magnetic resonance in medicine 2005;54:743–7. doi: 10.1002/mrm.20606.

51. Labadie C, Lee J, Rooney W, Jarchow S, Aubert-Frecon M, Springer, Jr. C, Moller H. Myelin water mapping by spatially regularized longitudinal relaxographic imaging at high magnetic fields. Magnetic Resonance in Medicine 2014;71:375–87. doi: 10.1002/mrm.24670.

52. Koenig S, Brown R, Spiller M, Lundbom N. Relaxometry of brain: Why white matter appears bright in MRI. Magnetic Resonance in Medicine 1990;14:482–95. doi: 10.1002/mrm.1910140306.

53. Mezer A, Yeatman J, Stikov N, et al. Quantifying the local tissue volume and composition in individual brains with magnetic resonance imaging. Natue Medicine 2013;19:1667–71. doi: 10.1038/nm.3390.

54. Gennis R. Biomembranes: molecular structure and function. New York: Springer-Verlag; 1989.

55. Horch AR, Gore JC, Does MD. Origins of the ultrashort T21H NMR signals in myelinated nerve: A direct measure of myelin content? Magnetic Resonance in Medicine 2011;66:24–31. doi: 10.1002/mrm.22980.

CHAPTER 6

MYELIN VOLUME FRACTION IMAGING IN DEVELOPING MOUSE BRAIN

6.1 INTRODUCTION

Chapter 5 displayed the ability of MET_2 and qMT to assess myelin content in normal and abnormal mature mice. However, it would also be beneficial to use these techniques during development to monitor myelination. Based on previous studies, myelin content and the estimated rate of myelin production in rats is shown in Fig 6.1. From this figure, it can be seen that myelin formation begins around postnatal days 10-12 (P10-P12). Around P20, ~15% of total myelin content exists, which is also the peak rate of myelin formation. While myelin production continues through maturation, the rate of myelin production greatly declines by P60, when rats are considered to be mature (1,2) .

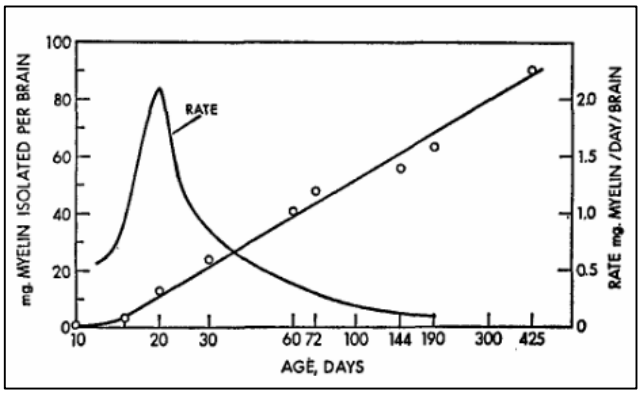

Figure 6.1. The accumulation of myelin plotted as a function of the logarithm of postnatal age. The circles (o) represent actual yields of myelin in mg/brain (left ordinate). The rate of accumulation is plotted as a smooth curve, with the maximum of 2.1 mg myelin day^{-1} $brain^{-1}$ (right ordinate) occurring at 20 days (1) .

Diffusion-weighted imaging (DWI) and diffusion tensor imaging (DTI) techniques have been used to study various normal and abnormal models of myelin development (3–5); however diffusion parameters are not a specific measure of myelin content. This is exemplified by groups observing changes in diffusion parameters prior to postnatal day 10, the start of myelin formation (6,7). Since diffusion is sensitive to axonal development in addition to myelination, DTI provides valuable information about development, but is not specific to myelin development. On the other hand, relaxation measures (MWF and BPF) may provide a more specific predictor of myelin, but have yet to be evaluated. In the present study, control mice at P10, P20, P30 and P60 are evaluated using MET_2 and qMT methods to obtain MWF and BPF and myelin volume measures, $f_{M,T2}$ and $f_{M,MT}$.

6.2 MATERIALS AND METHODS

6.2.1 Tissue Preparation

The Vanderbilt University Institutional Animal Care and Use Committee approved animal studies. Twenty-seven control mice (P10 (n=3), P20 (n=9), P30 (n=9), P60 (n=6)) were anesthetized with isoflurane and sacrificed via transcardial perfusion. The perfusion consisted of 1X phosphate-buffered saline (PBS) wash followed by 2.5% glutaraldehyde + 2% paraformaldehyde (modified Karnovsky solution). Following perfusion, brains were quickly removed from skull and immersed in the fixative solution for 1 week. Brains were then washed with 1X PBS + 0.01% sodium azide, changing wash 4-5 times over 1 week to remove excess fixative. In all cases, 1.0 mM Gd-DTPA (Magnevist; Berlex, Montville, NJ) was included in the perfusate, immersion and wash solutions, resulting in relatively uniform distribution of Gd-DTPA throughout the brain.

6.2.2 Magnetic Resonance Imaging

All imaging was performed on a 15.2-T 11-cm horizontal bore Bruker (Rheinstetten, Germany) BioSpec scanner, using a 35-mm diameter Bruker quadrature volume coil for transmission and reception. Both MET_2 and qMT scans were encoded with a matrix size of $128 \times 96 \times 72$ over a $1.92 \times 1.44 \times 1.08$ cm^3 FOV, providing 150 μm isotropic resolution.

For MET_2 imaging, a 3D multiple spin-echo sequence was used with non-selective excitation and refocusing pulses, 160 μs and 100 μs in duration, respectively. Each refocusing pulse was surrounded by 428 μs duration 6 G/cm amplitude crusher gradients, phase-encoding gradients were rewound after each echo, and a two-part (+X/-X) phase cycling scheme was used. With these constraints, secondary echoes that were not excited by the initial excitation pulse were removed, and the observed echo magnitudes could be computed with the extended phase graph (EPG) algorithm (8–10) . Scan parameters were: repetition time (T_R) = 520 ms, echo time (T_E) = 4.5 ms, number of echoes (N_E) = 24, receiver bandwidth (BW) = 75 kHz, and number of excitations (N_{EX}) = 8. Total scan time was ≈ 8 hr.

For qMT imaging, a 3D selective inversion-recovery prepared fast spin echo sequence (11) was used with 8 collected echoes, 5-ms echo spacing and centric phase encoding. To ensure that the longitudinal magnetization (M_z) recovered from $M_z = 0$ at the start of every pre-delay period, 8 additional refocusing pulses, also with 5-ms echo spacing, followed the 8th echo. A 1-ms hard pulse was used to selectively invert the free water magnetization, while macromolecular spins were mostly unaffected. The sequence was repeated $N_I = 15$ times with inversion times (T_I) log-spaced from 3.5 to 2000 ms. A constant predelay (T_d) of 590 ms resulted in a scan time of ~ 3.5hr.

6.2.3 Data Analysis

All data analysis was performed using MATLAB R2015a (The Mathworks, Natick MA) and MET_2 analyses were performed using the freely available Multi Exponential Relaxation Analysis (MERA) toolbox (12) . Prior to Fourier reconstruction, k-space data for all images were apodized using a 3D Tukey window with a 0.25 taper-to-window ratio and zero-padded 2×, resulting in 75 μm nominal isotropic resolution.

For each voxel, the MET_2 analysis used a separable non-linear approach. The T_2 spectrum was estimated by linear inverse (13) using a non-negative least-squares fit (14) of the N_E echo magnitudes to the sum of 100 EPG-defined signals with T_2 values logarithmically spaced between $T_E/2$ as 500 ms. The linear model was augmented with minimum curvature constraint weighted at a constant and conservative level across all voxels ($\mu = 0.002$). This linear inverse was repeated to find the refocusing pulse flip angle (θ) by non-linear regression, similar to previous work (9,10) . From all spectra, the myelin water fraction (MWF) was defined as the fraction of signal with $T_2 < 17$ ms.

For qMT analysis, the N_I image magnitudes were fitted voxel-wise to the Bloch-McConnell equations describing longitudinal relaxation and magnetization transfer between water and macromolecular protons (11,15). The five fitted model parameters were: M_{0f}, M_{0b}, k_{mf}, R_{1f}, and S_f, where $M_{0f/b}$ are the equilibrium magnetizations of the free and bound pools, respectively, k_{bf} is the rate constant of magnetization transfer from the bound to free water pool, R_{1f} is the longitudinal relaxation rate of the free water pool, and S_f is the efficiency of the inversion pulse on the free water pool. The corresponding R_{1b} and S_b values were constrained to $R_{1b} = 1$s and $S_b = 0.83$ in accord with prior studies (11) . The bound proton fraction (BPF) was then defined as $BPF = M_{0b} / (M_{0b} + M_{0f})$.

After MET_2 and qMT analysis, all parameter maps of a given model were co-registered in order to define closely comparable regions of interest (ROI) in each brain. For each mouse model, the first spin echo image of one brain was arbitrarily defined as the reference and the corresponding image from each other brain was registered to the reference using a rigid affine registration followed by a non-rigid deformable demons registration (16) . The resulting deformation fields of this registration were then applied to parameter maps. Four ROIs were drawn corresponding to the four regions extracted for histology (below): 3 in the corpus callosum in the mid-sagittal slice (genu (GCC), mid-body (MidCC), and splenium (SCC)) and the other in the anterior commissure (AC). In addition, a cortical gray matter (GM) ROI was drawn in the sagittal slice for comparison. Mean ROI values from different parameter maps and values derived from histology were compared using two-sample *t*-tests ($\alpha = 0.05$) and Pearson's linear correlation.

6.3 RESULTS AND DISCUSSION

Figure 6.2 displays representative T_2-weighted images ($N_E = 1$) along with parameter maps of long T_2 component, MWF, and BPF from P10, P20, P30 and P60 animals. There is an increase in T_2-weighted image contrast and long T_2 component between white and gray matter with development as expected with increasing myelin. Similarly, MWF and BPF display higher fractions in white matter with age.

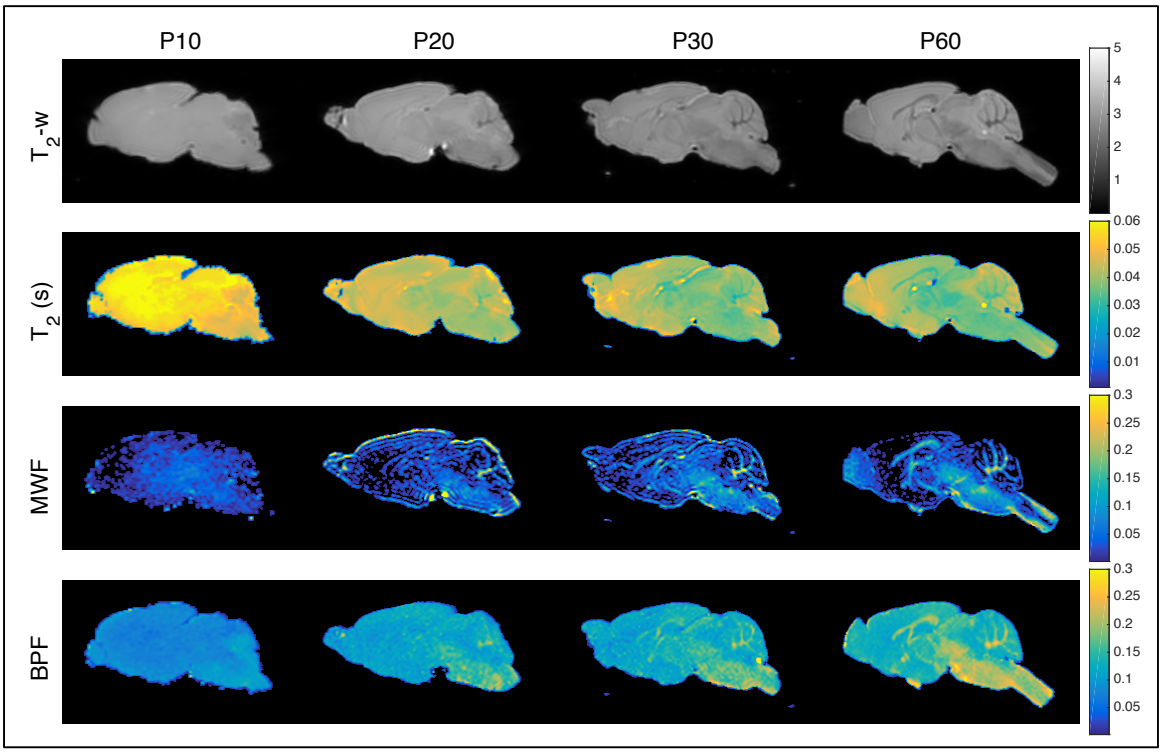

Figure 6.2. Representative images and parameter maps. (top to bottom) T_2-weighted images and long T_2, MWF and BPF maps from (left to right) P10, P20, P30, and P60 control mice.

Fig 6.3 displays quantitative analysis of parameters in four white matter (WM) regions of interest (ROIs) – midbody, genu and splenium of the corpus callosum (MidCC, GCC, SCC, respectively) and the anterior commissure (AC) – along with one cortical gray matter (GM) ROI. As expected, there is a decrease in long T_2 and an increase in MWF and BPF from P10 to P60 across all WM ROIs. There are significant decreases in long T_2 and increases BPF between each age in all WM ROIs but one. MWF is significantly different between P20 and P30 in all ROIs and between P30 and P60 in 3 out of 4 ROIs. Additionally, there are significant changes in T_2 and BPF in GM through P30, while MWF is consistently near zero.

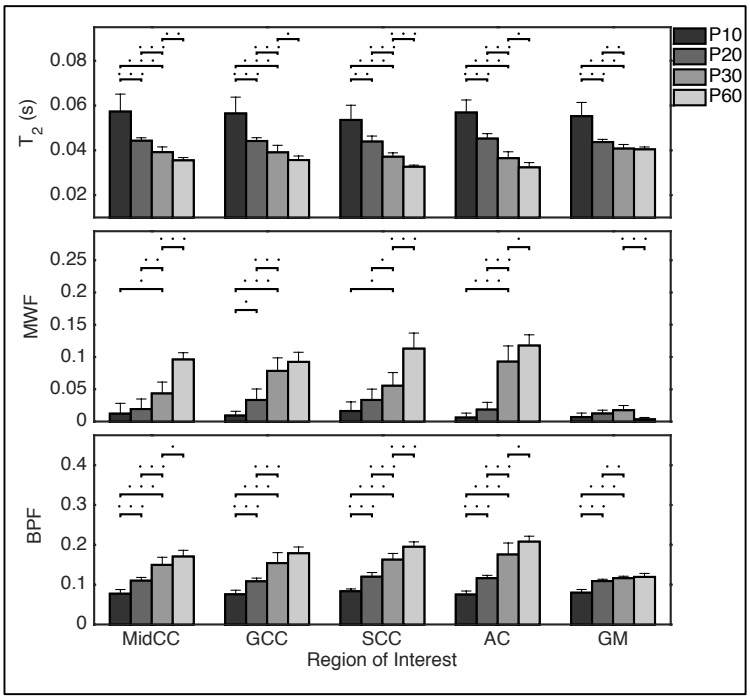

Figure 6.3. Region of Interest (ROI) MRI analysis. Mean + standard deviation (top to bottom) long T_2, MWF and BPF maps. Values are shown from 4 WM regions of interest and one gray matter region from P10, P20, P30, and P60 control mice where bars represent statistically significant differences ($\alpha = 0.05$). (• = $p < 0.05$, •• = $p < 0.01$, ••• = $p < 0.001$).

Fig 6.4 displays correlation between MWF and BPF showing strong linear correlation ($\rho = 0.85$), but the relationship is clearly not 1:1. Next, measures of myelin volume fraction (MVF) are calculated (See Chapter 5) from MWF ($f_{M,T2}$) and BPF ($f_{M,MT}$). While conversion from MWF to $f_{M,T2}$ is straightforward, calculating $f_{M,MT}$ requires a calibration factor, β. Since calibration from histology is not available, Chapter 5 proposed to use β =72% of BPF in gray matter. Using that guideline, we obtain β values shown in Table 6.1 From these, $f_{M,MT}$ is calculated and Fig 6.4 displays strong correlation between $f_{M,T2}$ and $f_{M,MT}$ ($\rho = 0.85$), with points lying around the line of unity.

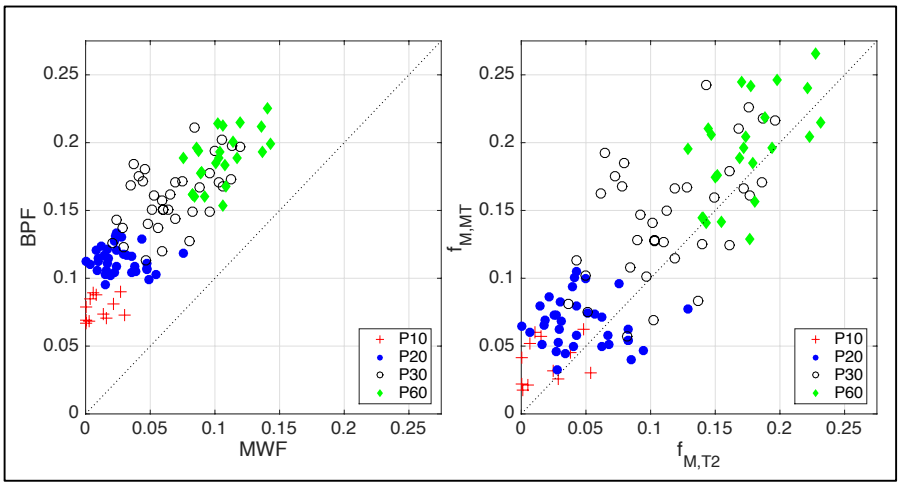

Figure 6.4. MRI scatter plots. (left) BPF versus MWF and line of unity (gray, dashed). $\rho = 0.85$. Mean standard errors from MWF and BPF are 0.0066 and 0.0032, respectively. (right) $f_{M,MT}$ versus $f_{M,T2}$ and line of unity (gray, dashed). $\rho = 0.85$.

Table 6.1. β offset values from gray matter BPF at each age.

Age	β	% β_{P60}
P10	0.0574	66.8%
P20	0.0784	91.3%
P30	0.0836	97.3%
P60	0.0859	100%

Fig 6.5 shows representative $f_{M,T2}$ and $f_{M,MT}$ maps from P10, P20, P30 and P60 animals displaying good qualitative agreement Gray matter values in $f_{M,MT}$ are closer to zero compared to BPF and remain consistent between ages. This displays the ability to detect changes specific to myelin with MRI myelin volume imaging. Previous works have largely used diffusion-weighted imaging and/or T_1 and T_2 imaging to assess development (17). While these techniques are sensitive to myelin changes, they are also sensitive to other aspects of brain growth and maturity such as gliosis and axon development. This is exemplified by a 'pre-myelination' state where changes in diffusion parameters precede the presence of myelin determined by myelin basic

protein and proteolipid protein histology staining (18,19). In addition, studies have also shown that unmyelinated nerves also display similar diffusion anisotropy (20). While myelin will contribute to anisotropy, this study and others demonstrates the sensitivity of DTI to changes in cytoskeletal development, but lack specificity to myelin development (21) .

In fact, BPF from qMT will also be sensitive to axonal and cytoskeleton development. To calculate myelin volume fraction, $f_{M,MT}$, the contribution from non-myelin macromolecules, β, must be removed. Previous work in rodents has shown that peak brain growth is ~P7-10 with gliogenesis and increasing axon and dendritic density. By P20, the brain has reached ~90-95% of its adult size and myelin growth takes over (22). Our values in Table 6.1 reflect this expected growth. This suggests that our applied calibration found from histology in Chapter 5 is reliable. Additionally, this reiterates the specificity that only MWF, $f_{M,T2}$, and $f_{M,MT}$ can provide to myelin development.

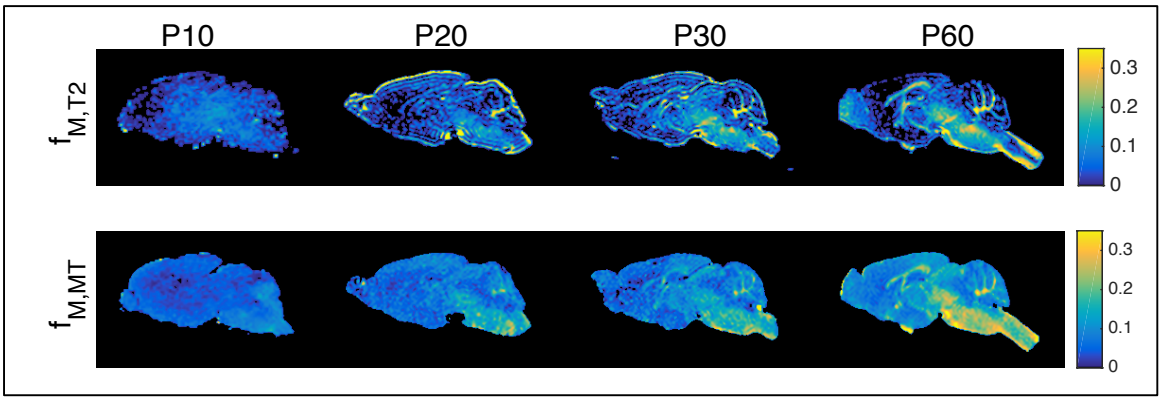

Figure 6.5. Group mean myelin volume fraction maps. Group mean $f_{M,T2}$ and $f_{M,MT}$ maps from (left to right) P10, P20, P30, and P60 control mice.

6.4 CONCLUSIONS

Development is a critical time for future neuronal health. However, in the first 30 days of rodent life there is much growth and development beyond myelin; so, it is important to have a measure that can tease out absolute changes in myelin content. We show that BPF suffers from non-myelin contributions of axons and cytoskeleton similar to DTI. However, myelin volume imaging allows for specific monitoring of myelin during development.

6.5 REFERENCES

1. Norton W, Poduslo S. MYELINATION IN RAT BRAIN: CHANGES IN MYELIN COMPOSITION DURING BRAIN MATURATION1. Journal of Neurochemistry 1973;21:759–73. doi: 10.1111/j.1471-4159.1973.tb07520.x.

2. Quarles RH, Macklin WB, Morell P. Myelin formation, structure and biochemistry. 2006.

3. Bockhorst KH, Narayana PA, Liu R, et al. Early postnatal development of rat brain: In vivo diffusion tensor imaging. Journal of Neuroscience Research 2008;86:1520–8. doi: 10.1002/jnr.21607.

4. Cheung MM, Hui ES, Chan KC, Helpern JA, Qi L, Wu EX. Does diffusion kurtosis imaging lead to better neural tissue characterization? A rodent brain maturation study. NeuroImage 2009;45:386–92. doi: 10.1016/j.neuroimage.2008.12.018.

5. Harsan LA, Poulet P, Guignard B, Steibel J, Parizel N, de Sousa PL, Boehm N, Grucker D, Ghandour MS. Brain dysmyelination and recovery assessment by noninvasive in vivo diffusion tensor magnetic resonance imaging. Journal of neuroscience research 2006;83:392–402. doi: 10.1002/jnr.20742.

6. Larvaron P, Boespflug-Tanguy O, Renou J-PP, Bonny J-MM. In vivo analysis of the post-natal development of normal mouse brain by DTI. NMR in biomedicine 2007;20:413–21. doi: 10.1002/nbm.1082.

7. Mori S, Itoh R, Zhang J, Kaufmann WE, van Zijl P, Solaiyappan M, Yarowsky P. Diffusion tensor imaging of the developing mouse brain. Magnetic Resonance in Medicine 2001;46:18–23. doi: 10.1002/mrm.1155.

8. Hennig J. Echoes—how to generate, recognize, use or avoid them in MR-imaging sequences. Part II: Echoes in imaging sequences. Concepts in Magnetic Resonance 1991;3:179–92. doi: 10.1002/cmr.1820030402.

9. Lebel MR, Wilman AH. Transverse relaxometry with stimulated echo compensation. Magnetic Resonance in Medicine 2010;64:1005–14. doi: 10.1002/mrm.22487.

10. Prasloski T, Mädler B, Xiang Q. Applications of stimulated echo correction to multicomponent T2 analysis. Magnetic Resonance in Medicine 2012;67:1803–14. doi: 10.1002/mrm.23157.

11. Gochberg DF, Gore JC. Quantitative magnetization transfer imaging via selective inversion recovery with short repetition times. Magnetic Resonance in Medicine 2007;57:437–41. doi: 10.1002/mrm.21143.

12. Does MD. Multi-Exponential Relaxation Analysis (MERA) Toolbox, Version 2, http://www.vuiis.vanderbilt.edu/~doesmd/MERA/MERA_Toolbox.html. 2014.

13. Whittall K, MacKay A. Quantitative interpretation of NMR relaxation data. Journal of Magnetic Resonance 1989;84:134–52. doi: 10.1016/0022-2364(89)90011-5.

14. Lawson, Hanson. Solving least squares problems. 1974.

15. Li K, Zu Z, Xu J, Janve V, Gore J, Does M, Gochberg D. Optimized inversion recovery sequences for quantitative T1 and magnetization transfer imaging. Magnetic Resonance in Medicine 2010;64:491–500. doi: 10.1002/mrm.22440.

16. Thirion J-P. Image matching as a diffusion process: an analogy with Maxwell's demons. Medical Image Analysis 1998;2:243–60. doi: 10.1016/S1361-8415(98)80022-4.

17. Paus T, Collins D, Evans A, Leonard G, Pike B, Zijdenbos A. Maturation of white matter in the human brain: a review of magnetic resonance studies. Brain Research Bulletin 2001;54:255–66.

18. Hamano, Takeya, Iwasaki, Nakayama, Ohto, Okada. A quantitative study of the progress of myelination in the rat central nervous system, using the immunohistochemical method for proteolipid protein. Brain research. Developmental brain research 1998;108:287–93. doi: 10.1016/S0165-3806(98)00063-7.

19. Wimberger DM, Roberts TP, Barkovich AJ, Prayer LM, Moseley ME, Kucharczyk J. Identification of "Premyelination" by Diffusion-Weighted MRI . Journal of Computer Assisted Tomography 1995;19:28–33.

20. Beaulieu C, Allen P. Determinants of anisotropic water diffusion in nerves. Magnetic Resonance in Medicine 1994;31:394–400. doi: 10.1002/mrm.1910310408.

21. Beaulieu C. The basis of anisotropic water diffusion in the nervous system–a technical review. NMR in Biomedicine 2002;15:435–455.

22. Semple BD, Blomgren K, Gimlin K, Ferriero DM, Noble-Haeusslein LJ. Brain development in rodents and humans: Identifying benchmarks of maturation and vulnerability to injury across species. Prog. Neurobiol. 2013;106-107:1–16. doi: 10.1016/j.pneurobio.2013.04.001.

CHAPTER 7

A REVISED MODEL FOR ESTIMATING G-RATIO FROM MRI

7.1. INTRODUCTION

Myelin is a critical component of white matter, increasing speed of action potential conduction along axons and improving neurological function. It has been shown that there is a range of values between axon size and myelin thickness for optimal efficiency in healthy tissue (1,2). The g-ratio describes the relationship between axon size and myelin thickness, and deviations in the g-ratio are thought to be involved in abnormal development and disease (3–6). However, currently, the only way to assess properties of tissue microstructure such as axon diameter, myelin thickness, and g-ratio is through quantitative histology, such as electron microscopy. Such methods are time consuming, expensive, and destructive to the tissue. Magnetic resonance imaging (MRI) methods to measure these microstructural characteristics would be useful to more efficiently study white matter disease processes and treatments and, further, provide the potential for *in vivo* assessment.

Recently, it has been proposed that two quantitative MRI measures can be combined and interpreted with a geometric model of white matter to provide quantitative estimates of the g-ratio (7,8). Specifically, Stikov and colleagues have suggested that using MRI estimates of 1) myelin volume fraction (from, for example, quantitative magnetization transfer measurements), and 2) axon or fiber volume fraction (from, for example, suitable analysis of diffusion-weighted imaging) can be used to estimate the g-ratio. These estimates were termed an “aggregate g-ratio” because the method is predicated on the assumption that the g-ratio is constant for all axons within a voxel, which is known not to be the case in both peripheral nerve (1,9) and central white

matter (10,11). Here we extend their model to a more general one that makes no assumption about the distribution of g-ratio values within an imaging voxel, and we demonstrate the model in principal using quantitative evaluations of electron microscopy of the corpus callosum of control and hypomyelinated mice.

7.2 THEORY

Consider an ensemble of N myelinated fibers with the radius and g-ratio of the i^{th} fiber being R_i and g_i, respectively, and axon radius being r_i (hence, $g_i = r_i/R_i$, see Fig 1e). The total cross-sectional areas of fibers, axons, and myelin, are, respectively,

$$\begin{aligned} A_{\mathrm{F}} &= \pi \sum_{i=1}^{N} R_i^2 \\ A_{\mathrm{A}} &= \pi \sum_{i=1}^{N} g_i^2 R_i^2 = \pi \sum_{i=1}^{N} r_i^2 \\ A_{\mathrm{M}} &= \pi \sum_{i=1}^{N} R_i^2 \left(1 - g_i^2\right) \end{aligned} \quad . \qquad [7.1]$$

From here, the ratio of myelin to fiber areas is

$$\frac{A_{\mathrm{M}}}{A_{\mathrm{F}}} = \frac{\sum_{i=1}^{N} R_i^2 \left(1 - g_i^2\right)}{\sum_{i=1}^{N} R_i^2} \quad . \qquad [7.2]$$

In the case that $g_i = g$ for all $i = 1$ to N, as assumed in the model presented by Stikov et al. (7,8), this ratio reduces to

$$\frac{A_{\mathrm{M}}}{A_{\mathrm{F}}} = 1 - g^2 \quad . \qquad [7.3]$$

Assuming one can measure myelin volume fraction (*MVF*) and fiber volume fraction (*FVF*) with MRI, the ratio $A_{\mathrm{M}}/A_{\mathrm{F}}$ can be replaced with *MVF*/*FVF*, and the resulting MRI-measured g-ratio is then

$$g_{\mathrm{MRI}} \equiv \sqrt{1 - MVF/FVF}\,, \qquad [7.4]$$

as previously presented (7,8).

By starting with the ratio A_M/A_A, a similar relationship is found, $g_{\mathrm{MRI}} \equiv \sqrt{1/\left(1 + MVF/AVF\right)}$, where AVF is the axon volume fraction as measured by MRI.

However, without the simplifying assumption that g is constant for all axons, Eq [7.2] can be simply reduced to

$$\frac{A_{\mathrm{M}}}{A_{\mathrm{F}}} = \frac{\sum_{i=1}^{N} R_i^2 - \sum_{i=1}^{N} g_i^2 R_i^2}{\sum_{i=1}^{N} R_i^2} = 1 - \frac{\sum_{i=1}^{N} g_i^2 R_i^2}{\sum_{i=1}^{N} R_i^2}\,. \qquad [7.5]$$

Again, replacing the A_M/A_F with MVF/FVF and using Eq [7.4], we get

$$g_{\mathrm{MRI}}^2 = \frac{\sum_{i=1}^{N} g_i^2 R_i^2}{\sum_{i=1}^{N} R_i^2}\,, \qquad [7.6]$$

which shows that the squared value of the previously proposed MRI measure of g-ratio is equal to the area-weighted mean of g^2 values across the N fibers.

7.3. MATERIALS AND METHODS

7.3.1 Tissue Preparation

Animal studies were approved by the Vanderbilt University Institutional Animal Care and Use Committee. Histology was acquired from control and *Rictor* conditional knockout (CKO) mice, similar to a previously described mouse model of tuberous sclerosis complex (12). Six adult mice were anesthetized with isoflurane and sacrificed via transcardial perfusion of 1X phosphate-buffered saline (PBS) wash followed by 2.5% glutaraldehyde + 2% paraformaldehyde

in PBS (modified Karnovsky solution). Following perfusion, brains were quickly removed from the skull and immersed in the fixative solution for 1 week. For MRI studies not presented here, the perfusion and immersion solutions included a paramagnetic MRI contrast agent and the fixative was washed out of brains prior to imaging and subsequent histology. For histologic preparation, a 1-2 mm sagittal slice of tissue was cut from the left hemisphere beginning at the mid-brain from each of 6 brains (n=4 control and n=2 CKO). Subsequently, 2 regions of white matter from the corpus callosum (genu- GCC and midbody - MidCC) were cut from each slice. Two regions were analyzed to account for potentially different axon populations between regions of the corpus callosum (13). Tissue samples were then processed for transmission electron microscopy in the Vanderbilt Cell Imaging Shared Resource-Research Electron Microscopy facility. Thick sections (0.5 – 1 μm) were collected using a Leica Ultracut microtome (UC-7), then stained with 1% toluidine blue. Ultra-thin sections (70-80 nm) were then cut and collected on 300-mesh copper grids. Copper grids were post-section stained at room temperature with 2% uranyl acetate (aqueous) for 15 minutes and then with lead citrate for 10 minutes. Ultra-thin sections were imaged on the Philips/FEI Tecnai T12 electron microscope at 15,000X magnification. From each section, six images were acquired using a side-mounted AMT CCD camera, resulting in a total of 6 mice x 2 regions x 6 images/region/mouse = 72 images.

7.3.2 Data Analysis

The pipeline of histology analysis is summarized in Fig 7.1. Images were segmented using Otsu's method (14) to distinguish between myelin (white) and non-myelin (black) pixels, providing an estimate of *MVF* and a binary image (Fig 1c). From the binary image, each myelinated axon was manually identified and its area (A_{Ai}, for the i^{th} axon) was computed using a region growing algorithm. This value provided an estimate of axon radius $r_i = \sqrt{A_{Ai}/\pi}$, and the

sum of all axon areas provided an estimate of *AVF*. For each axon, the thickness of the surrounding myelin (Δ_i) was calculated as the average of manual measurements made in two locations, and the g-ratio was estimated as $g_i = r_i / (r_i + \Delta_i)$.

From each image, the *MVF* and *AVF* estimates were used to compute g_{MRI}, as shown above. Also from each image, the N (= 40-60) measures of g were fitted to a gamma distribution as done previously for axon diameter distributions (13,15), from which three descriptive measures were calculated: arithmetic mean (g_{mean}), the area-weighted mean (g_{awm}), the square-root of the area-weighted g^2 (g_{awmgs}, following the right hand side of Eq [7.6]). Calculating these descriptive measures of g from the fitted gamma distribution parameters rather than directly from the samples g_i, i = 1 to N, resulted in lower variance estimates of the area-weighted measures of g-ratio.

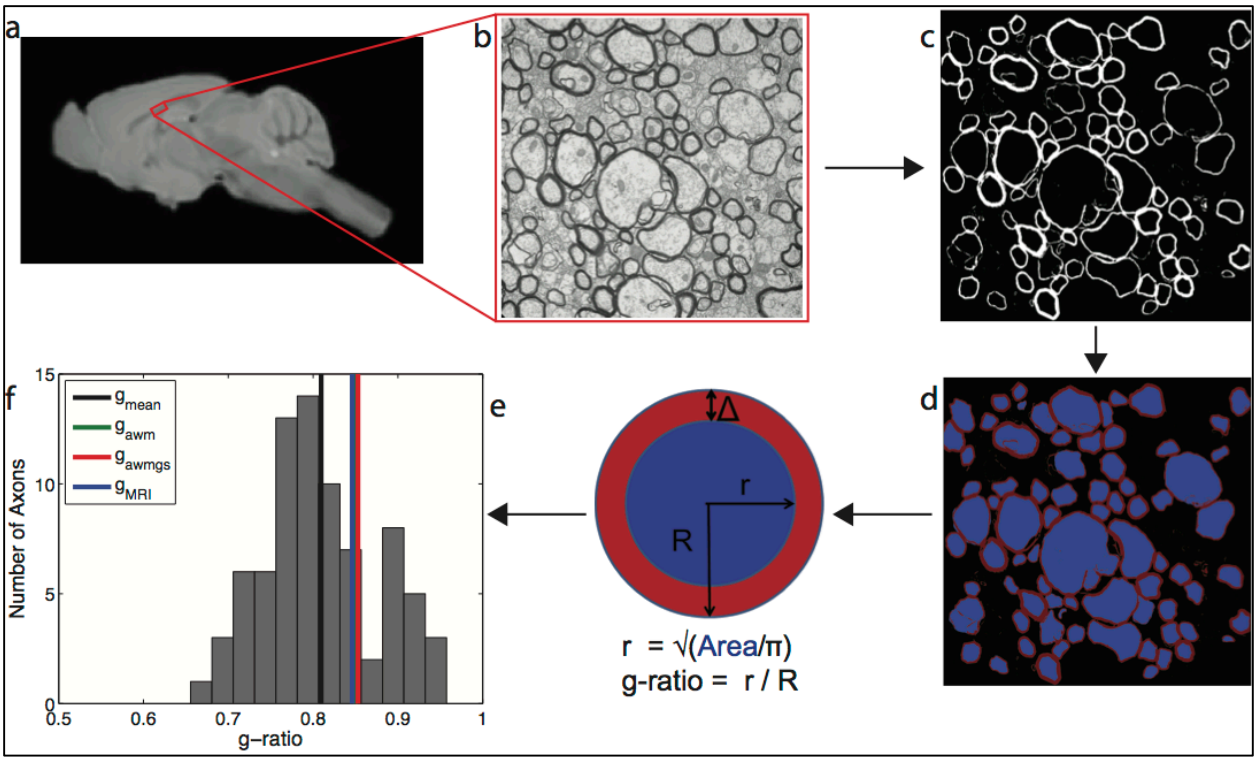

Figure 7.1. Histology analysis methods. a) Demonstration of the middle corpus callosum region chosen for electron microsopy tissue preparation. b) A transmission electron microscope image is acquired from the middle region of the mouse corpus callosum. c) A threshold is applied to separate myelin and non-myelin pixels and obtain a binary myelin mask, providing a myelin volume fraction (*MVF*). d) A region growing algorithm is used to fill all axon areas, and the sum of all axon areas provides an axon volume fraction (*AVF*). Myelin thickness is measured manually in two locations per axon. e) Axon radius (*r*) is derived from the area of each axon, assuming circular geometry. f) The g-ratio is calculated per axon and the histogram of values is fitted to a gamma distribution, from which the following measures are computed: mean (g_{mean}), area-weighted mean (g_{awm}), and the square root of the area-weighted g^2 (g_{awmgs}). The proposed MRI measure, g_{MRI}, was computed from measures of *MVF* and *AVF*.

7.4. RESULTS AND DISCUSSION

Figure 7.1f displays a representative histogram of the g-ratios obtained from one histology image. Each characterization of the g-ratio (g_{mean}, g_{awm}, g_{awmgs}, and g_{MRI}) is displayed on the histogram. It is apparent that g_{mean} (~0.8) is significantly lower than the area-weighted means and g_{MRI}. This characteristic will be true in general for distributions of finite width, but will also depend on the skewness of the distribution.

Figure 7.2 displays comparisons of g_{MRI} with g_{mean}, g_{awm}, and g_{awmgs}, respectively, from left to right. Each point represents the measurements from one image with both MidCC and GCC measures displayed (control = black, CKO = red). The hypomyelination present in the CKO mice is apparent from the generally greater g-ratios. Qualitatively, g_{MRI} shows a reasonable correspondence with all three measures, but the comparisons between g_{MRI} and the area-weighted measures are noticeably closer to the line of identity (dashed line). Quantitatively, these differences are reflected in the root mean squared difference (RMSD), between the two measures for each plot. Similar relationships are found between g_{MRI} and the two area-weighted measures, g_{awm} and g_{awmgs}, indicating that g_{MRI} can be reasonably interpreted as an axon-area-weighted measure of g, which is somewhat easier to intuit than the square root of the axon-area-weighted g^2. Both area-weighted measures show a slight trend toward being underestimated by g_{MRI} at lower values of g, which may reflect the limitations of the histology analysis. As apparent in Figs 7.1c and 7.1d, there was a tendency to overestimate *MVF* from the thresholded image, particularly when myelinated axons were more densely packed and connected, which also corresponded to cases of lower g-ratios. This overestimation of *MVF* will reduce estimates of g_{MRI} but will not affect the other characterizations of g which were derived from direct measures of myelin thickness.

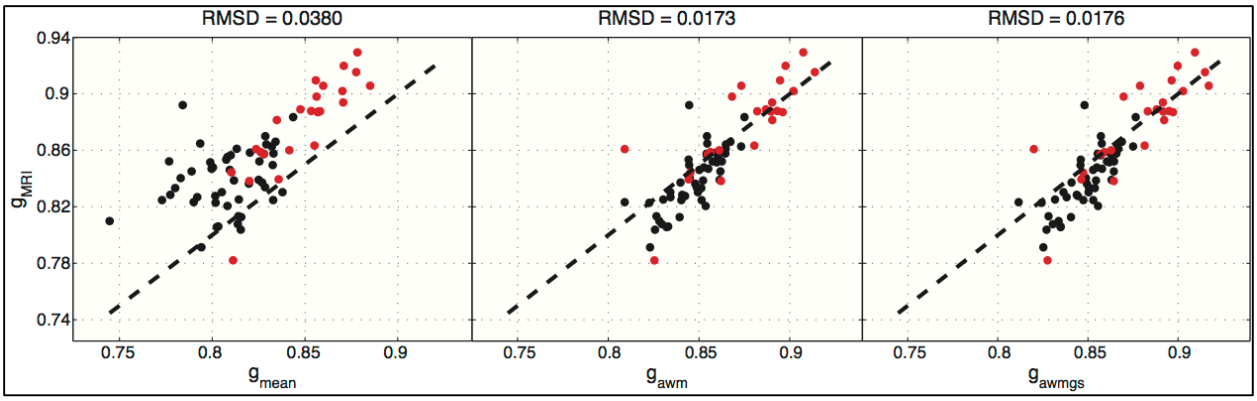

Figure 7.2. Scatter plots of g-ratio. (left) g_{MRI} versus g_{mean}, (middle) g_{MRI} versus g_{awm}, and (right) g_{MRI} versus g_{awmgs} where black and red points signify control and CKO image measures, respectively. The root mean squared difference (RMSD) between each pair of measures is shown above each plot.

Fig 7.3 shows scatter plots of g-ratio versus axon diameter for all 6 images from the representative control and CKO brains for both regions. In all cases, the relationship between axon diameter and *g* exhibited a curved shape seen in some previous studies (10,11), and appear to be well described by the log-linear equation proposed by Berthold et al. ($nl = C_0 + C_1*d + C_2*\log(d)$); where nl = number of myelin lamellae and d = axon diameter (blue line) (10). These observations are in contrast to a recent similar histological evaluation of the macaque corpus callosum (16) who showed only moderate linear correlations between g-ratio and axon diameter.

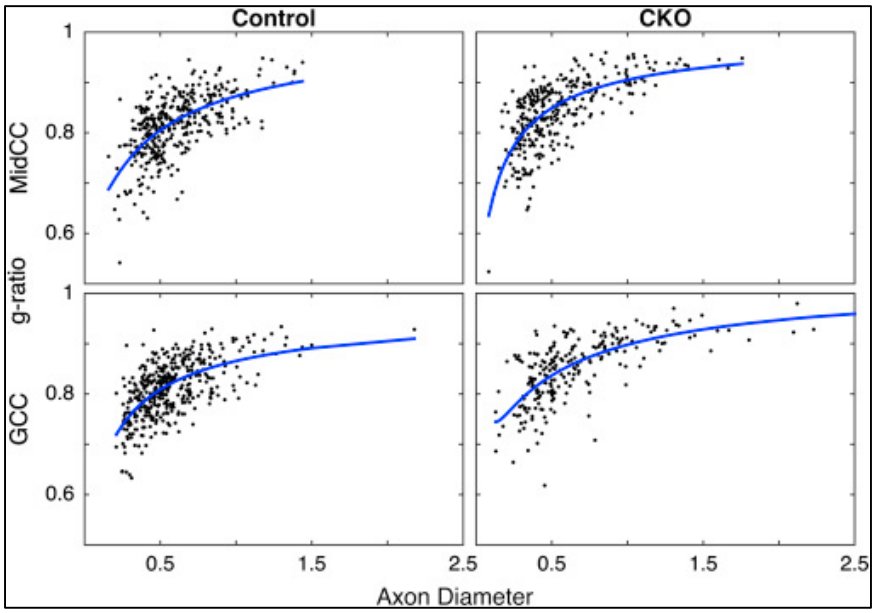

Fig 7.3 Representative g-ratio versus axon diameter scatter plots. Log-linear fits (blue) from MidCC (top) and GCC (bottom) regions of the corpus callosum of control (left) and *Rictor* CKO (right) mice.

The histology data are also summarized in Table 7.1, which displays the mean ± standard error of the mean of the four g–ratio measures across the 6 images from each region (MidCC, GCC) for control and CKO mice. Reported g_{mean} values of control images agree with previously published values for mouse corpus callosum (5,17). It is apparent that the two area-weighted measures (g_{awm}, g_{awmgs}) are nearly identical in all cases and similar to g_{MRI} values. All measures show statistically significant differences (using a two-tailed student's t-test, α=0.05) between control and CKO mice, demonstrating that for this example, g_{MRI}, which reports a significantly different value than g_{mean}, is sufficient to detect differences in microstructure between the control and CKO mice. However, we note the time course of demyeliation and remyelination may not always be well captured by a scalar value, and because of the area-weighting effect, g_{MRI} in particular will be less sensitive to microstructural changes in smaller axons. For example, a previous study of microstructure in the mouse corpus callosum during and following exposure to cuprizone in the diet (5) observed periods with changes in myelin thickness and axon diameter

that were not caputured by the mean g-ratio, and found that recovery periods involved preferential remyelination of smaller axons. Perhaps these limitations can be overcome with more sophisticated models that incorporate axon diameter distributions (such as is done with the AxCaliber method, (13,18)) and established relationships between axon diameter and g-ratio shown in Fig 7.3 (2,10)); however, the practical limits on MRI measures of g-ratio may come from the ability make robust estimates of *MVF* and *FVF*, which remains an area of active study.

Table 7.1. g-ratio values. g_{mean}, g_{awm}, g_{awmgs}, and g_{MRI} mean ± SEM from the middle and genu regions of the corpus callosum across all images for control and Rictor CKO mice.

Region	g_{mean}	g_{awm}	g_{awmgs}	g_{MRI}
	Control			
MidCC	0.815±0.003	0.848±0.003	0.850±0.003	0.844±0.004
GCC	0.803±0.005	0.847±0.003	0.849±0.003	0.834±0.005
	CKO			
MidCC	0.845±0.006	0.873±0.007	0.875±0.007	0.870±0.010
GCC	0.854±0.006	0.880±0.009	0.883±0.009	0.889±0.008

7.5 CONCLUSIONS

As quantitative MRI methods strive to provide more detailed information about underlying tissue properties, such as the g-ratio, histologic comparisons are vital to understand microstructural meaning of derived imaging measures. We have shown here that the recently proposed approach to estimate the aggregate g-ratio index with MRI will, in principal, provide a measure that is close to the axon-area-weighted measures of *g* across all axons in a voxel. This measure will naturally be more sensitive to changes or differences in larger diameter axons and should be interpreted with this knowledge.

7.6 REFERENCES

1. Rushton W. A theory of the effects of fibre size in medullated nerve. The Journal of Physiology 1951;115:101–22. doi: 10.1113/jphysiol.1951.sp004655.

2. Chomiak, Hu. What is the optimal value of the g-ratio for myelinated fibers in the rat CNS? A theoretical approach. 2009. doi: 10.1371/journal.pone.0007754.

3. Albert M, Antel J, Brück W, Stadelmann C. Extensive cortical remyelination in patients with chronic multiple sclerosis. Brain pathology (Zurich, Switzerland) 2007;17:129–38. doi: 10.1111/j.1750-3639.2006.00043.x.

4. Fields D. White matter in learning, cognition and psychiatric disorders. Trends in Neurosciences 2008;31. doi: 10.1016/j.tins.2008.04.001.

5. Mason J, Langaman C, Morell P, Suzuki K, Matsushima G. Episodic demyelination and subsequent remyelination within the murine central nervous system: changes in axonal calibre. Neuropathology and Applied Neurobiology 2001;27:50–8. doi: 10.1046/j.0305-1846.2001.00301.x.

6. Paus T, Toro R. Could sex differences in white matter be explained by g ratio. Frontiers in neuroanatomy [Internet] 2009.

7. Stikov N, Perry L, Mezer A, Stikov N, Perry LM, Mezer A, Rykhlevskaia E, Wandell B, Pauly J, Dougherty R. Bound pool fractions complement diffusion measures to describe white matter micro and macrostructure. NeuroImage 2011;54:1112–21. doi: 10.1016/j.neuroimage.2010.08.068.

8. Stikov N, Campbell JS, Stroh T, Lavelée M, Frey S, Novek J, Nuara S, Ho M-K, Bedell BJ, Dougherty RF. In vivo histology of the myelin g-ratio with magnetic resonance imaging. NeuroImage 2015;118:397–405. doi: 10.1016/j.neuroimage.2015.05.023.

9. Friede RL, Beuche W. Combined scatter diagrams of sheath thickness and fibre calibre in human sural nerves: changes with age and neuropathy. Journal of neurology, neurosurgery, and psychiatry 1985;48:749–56. doi: 10.1136/jnnp.48.8.749.

10. Berthold C, Nilsson I, Rydmark M. Axon diameter and myelin sheath thickness in nerve fibres of the ventral spinal root of the seventh lumbar nerve of the adult and developing cat. Journal of anatomy 1983;136:483–508.

11. Little GJ, Heath JW. Morphometric analysis of axons myelinated during adult life in the mouse superior cervical ganglion. Journal of anatomy 1994;184 (Pt 2):387–98.

12. Carson RP, Fu C, Winzenburger P, Ess KC. Deletion of Rictor in neural progenitor cells reveals contributions of mTORC2 signaling to tuberous sclerosis complex. Human Molecular Genetics 2013;22:140–52. doi: 10.1093/hmg/dds414.

13. Barazany D, Basser PJ, Assaf Y. In vivo measurement of axon diameter distribution in the corpus callosum of rat brain. Brain : a journal of neurology 2009;132:1210–20. doi: 10.1093/brain/awp042.

14. Otsu N. A threshold selection method from gray-level histograms. IEEE Transactions on systems, man, and cybernetics 1979;9:62–6.

15. Olivares, Montiel, Aboitiz F. Species Differences and Similarities in the Fine Structure of the Mammalian Corpus callosum. Brain, Behavior and Evolution 2001;57:98–105. doi: 10.1159/000047229.

16. Stikov N, Campbell J, Stroh T, et al. Quantitative analysis of the myelin g-ratio from electron microscopy images of the macaque corpus callosum. Data in Brief 2015;4:368–73.

17. Arnett HA, Mason J, Marino M, Suzuki K, Matsushima GK, Ting JP. TNF alpha promotes proliferation of oligodendrocyte progenitors and remyelination. Nature neuroscience 2001;4:1116–22. doi: 10.1038/nn738.

18. Assaf, Blumenfeld-Katzir, Yovel. AxCaliber: a method for measuring axon diameter distribution from diffusion MRI. 2008. doi: 10.1002/mrm.21577.

CHAPTER 8

EVALUATION OF G-RATIO FROM MRI IN EX VIVO MOUSE BRAIN

8.1. INTRODUCTION

Myelin is a key component of healthy white matter leading to faster action potential conduction velocity along axons. Changes in myelin content and structure occur in several neurodegenerative diseases, such as Multiple Sclerosis (MS) (1) and Alzheimer's disease (2). Additionally, abnormal axon and myelin development cause altered connectivity that may be a key factor in neuropsychiatric disorders such as Autism Spectrum Disorder (3), Schizophrenia (4), and Obsessive Compulsive Disorder (5). While measures of myelin volume fractions tell about the amount of myelin, a measure capable of relating myelin volume relative to axon volume provides more detail about pathologic changes. The g-ratio is the ratio of axon diameter to myelinated fiber diameter, and has been proposed to capture the microsctructural changes of myelin thickness (6,7). Currently, the only validated technique to measure the g-ratio is electron microscopy, which allows direct visualization of myelinated axons in cross section. However, this approach is slow, expensive, and is limited to *ex vivo* samples and brain locations where axons can be sectioned perpendicular to their orientation.

To overcome these limitations of electron microscopy for evaluating the g-ratio, Stikov et al. proposed that a geometric model using the relationship between the myelin and axon volume fractions (MVF and AVF, respectively) to obtain an "aggregate" g-ratio, shown in Equation 8.1 (8,9).

$$g = \frac{1}{\sqrt{1 + \frac{MVF}{AVF}}} \qquad [8.1]$$

However, each imaging voxel contains a distribution of g-ratios. Based on histology measures, West et al. displayed that this geometric equation for g (*Eq. 8.*1) provides an area-weighted g-ratio from all axons in a voxel (10). This model has been proposed as a method to obtain g-ratio from MRI (g_{MRI}) using measures of myelin and axon volume fraction from MRI techniques.

Myelin content can be estimated using numerous techniques, but measures of MVF from MRI were displayed previously by West et al. and shown to correlate well with histologic measures of MVF (*See* Chapter 5). Briefly, myelin water fraction (MWF) from multiexponential T_2 (MET_2) data or bound pool fraction (BPF) from quantitative magnetization transfer (qMT) can be converted to volume fractions based on a volumetric four-pool model of white matter protons and literature values of water pool fractions. This technique results in two MRI measures of MVF: $f_{M,T2}$ and $f_{M,MT}$, where subscripts "T2" and "MT" describe the method used. While both measures provided promising results, $f_{M,T2}$ may be biased by effects from intercompartmental water exchange and $f_{M,MT}$ is dependent on a calibration factor to account for non-myelin bound proton contributions.

A measure of AVF can be derived from measures of axon water fraction obtained using an advanced diffusion model. There are a variety of techniques that can be used including Neurite Orientation Dispersion and Density Imaging (NODDI) (11), Tensor Fiber Density (TFD) (12), and White Matter Tract Integrity (WMTI) (13), along with numerous others. To obtain tissue-specific characteristics of white matter, each of these methods have *a priori* assumptions which may depend on each tissue of interest. Additionally, AVF still relies on an accurate myelin

volume fraction measure to convert axon water fraction to an axon volume fraction to use in *Eq* 8.1.

The present study uses previously displayed measures of MVF along with measures of AWF from WMTI and compare resulting g_{MRI} estimates to g-ratio measures from quantitative electron microscopy (g_{Hist}). This is shown in control mouse brains along with two models of hypomyelination and one model of hypermyelination to display variations in g-ratio.

8.2. MATERIALS AND METHODS

8.2.1 Tissue Preparation

The Vanderbilt University Institutional Animal Care and Use Committee approved animal studies. 15 adult mice were anesthetized with isoflurane and sacrificed via transcardial perfusion. The perfusion consisted of 1X phosphate-buffered saline (PBS) wash followed by 2.5% glutaraldehyde + 2% paraformaldehyde (modified Karnovsky solution). Following perfusion, brains were quickly removed from skull and immersed in the fixative solution for 1 week. Brains were then washed with 1X PBS + 0.01% sodium azide, changing wash 4-5 times over 1 week to remove excess fixative. In all cases, 1.0mM Gd-DTPA (Magnevist; Berlex, Montville, NJ) was included in the perfusate, immersion and wash solutions, resulting in relatively uniform distribution of Gd-DTPA throughout the brain.

This study used control animals (n=6) along with two previously described models of hypomyelination and one of hypermyelination (n = 3 for each model). All models utilized the *Olig2-Cre* driver to conditionally target proteins involved in PI3K/Akt signaling in oligodendrocyte precursor cells. In the first model, the *Tsc2* gene is deleted (*Tsc2 CKO*–conditional knockout) and exhibits extreme loss of myelin (14). The second model targets *Rictor*

(*Rictor CKO*), a key component of the mTORC2 complex, and also displays hypomyelination, but less severe than *Tsc2* model (15). The third model results from the deletion of *Pten* (*Pten* CKO) leading to activation of the PI3K/Akt signaling pathway and subsequent hypermyelination (16).

2.2 Magnetic Resonance Imaging

All imaging was performed on a 15.2-T 11-cm horizontal bore Bruker (Rheinstetten, Germany) BioSpec scanner, using a 35-mm diameter Bruker quadrature volume coil for transmission and reception. Both MET_2 and qMT scans were encoded with a matrix size of 128 × 96 × 72 over a 1.92 × 1.44 × 1.08 cm^3 FOV, providing 150μm isotropic resolution.

For MET_2 imaging, a 3D multiple spin-echo sequence was used with non-selective excitation and refocusing pulses, 160 μs and 100 μs in duration, respectively. Each refocusing pulse was surrounded by 428 μs duration 6 G/cm amplitude crusher gradients, phase-encoding gradients were rewound after each echo, and a two-part (+X/-X) phase cycling scheme was used. With these constraints, secondary echoes that were not excited by the initial excitation pulse were removed, and the observed echo magnitudes could be computed with the extended phase graph (EPG) algorithm (17–19). Scan parameters were: repetition time (T_R) = 520ms, echo time (T_E) = 5.8ms, number of echoes (N_E) = 18, receiver bandwidth (BW) = 38.5kHz, and number of excitations (N_{EX}) = 6. Total scan time was ≈ 6 hr.

For qMT imaging, a 3D selective inversion-recovery prepared fast spin echo sequence (20) was used with 8 collected echoes, 5-ms echo spacing and centric phase encoding. To ensure that the longitudinal magnetization (M_z) recovered from $M_z = 0$ at the start of every pre-delay period, 8 additional refocusing pulses, also with 5-ms echo spacing, followed the 8th echo. A 1-ms hard pulse was used to selectively invert the free water magnetization, while macromolecular spins

were mostly unaffected. The sequence was repeated N_I = 15 times with inversion times (T_I) log-spaced from 3.5 to 2000 ms. A constant predelay (T_d) of 590 ms resulted in a scan time of ~ 3.5hr.

Diffusion kurtosis imaging data were acquired using a 3D diffusion-weighted fast spin-echo sequence with TR/TE/ESP = 200/19.0/7.1 ms and ETL = 4 (Beaulieu et al., 1993). For excitation and refocusing, non-selective hard pulses were implemented with durations of 125 and 250 μs, respectively. Receiver bandwidth for signal acquisition = 75 kHz. Diffusion weighting was achieved with gradient pulse duration (δ) = 5 ms, diffusion time (Δ) = 12 ms, prescribed b-values = 3000 and 6000 s/mm^2, 30 directions (Jones et al., 1999), and 2 signal averages with gradient polarity reversal to mitigate background gradient cross-terms. 5 b=0 images were collected and averaged to improve the precision of DKI fits. In all, for each brain, 125 3D volumes were collected in a total scan time of ≈ 12 hr.

8.2.3 Data Analysis

All data analysis was performed using MATLAB R2015a (The Mathworks, Natick MA) and MET_2 analyses were performed using the freely available Multi Exponential Relaxation Analysis (MERA) toolbox (21). Prior to Fourier reconstruction, k-space data for all images were apodized using a 3D Tukey window with a 0.25 taper-to-window ratio and zero-padded 2×, resulting in 75 μm nominal isotropic resolution.

For each voxel, the MET_2 analysis used a separable non-linear approach. The T_2 spectrum was estimated by linear inverse (22) using a non-negative least-squares fit (NNLS; Lawson and Hanson, 1974) of the N_E echo magnitudes to the sum of 100 EPG-defined signals with T_2 values logarithmically spaced between T_E/2 as 500 ms. The linear model was augmented with minimum curvature constraint weighted at a constant and conservative level across all voxels (μ = 0.002).

This linear inverse was repeated to find the refocusing pulse flip angle (θ) by non-linear regression, similar to previous work (Lebel and Wilman, 2010; Prasloski et al., 2012). From all spectra, the myelin water fraction (MWF) was defined as the fraction of signal with $T_2 < 17$ ms. MWF was then converted to a myelin volume fraction ($f_{M,T2}$) as shown previously (*See* Chapter 5) using Eq 8.2

$$f_{M,T2} = \frac{MWF \times \Phi_{W,NM}}{MWF \times \left(\Phi_{W,NM} - \Phi_{W,M}\right) + \Phi_{W,M}}, \quad [8.2]$$

where $\Phi_{H20,M}$ and $\Phi_{H20,NM}$ are the proton pool volume fraction in myelin and non-myelin white matter, respectively.

For qMT analysis, the N_I image magnitudes were fitted voxel-wise to the Bloch-McConnell equations describing longitudinal relaxation and magnetization transfer between water and macromolecular protons (20,23). The five fitted model parameters were: M_{0f}, M_{0m}, k_{mf}, R_{1f}, and S_f, where $M_{0f/m}$ are the equilibrium magnetizations of the free and macromolecular pools, respectively, k_{mf} is the rate constant of magnetization transfer from the macromolecular to free water pool, R_{1f} is the longitudinal relaxation rate of the free water pool, and S_f is the efficiency of the inversion pulse on the free water pool. The corresponding R_{1m} and S_m values were constrained to R_{1m} = 1s and S_m = 0.83 based in accord with prior studies (20). The macromolecular proton fraction (MPF) was then defined as $MPF = M_{0m} / (M_{0m} + M_{0f})$. MPF was then converted to a myelin volume fraction ($f_{M,MT}$) as described previously (*See* Chapter 5) as shown in Eq 8.3.

$$f_{M,MT} = \left(1 + \frac{\Phi_{W,M}}{1 - \Phi_{W,M}}\right) \times \left[BPF - \beta\right], \quad [8.3]$$

where β is a calibration constant from the non-myelin macromolecular contribution defined here by histology = 0.086.

Diffusion Kurtosis image data were analyzed using in-house written code in MATLAB (Mathworks, Natick, MA, USA). For DKI analysis, 3D k-space data were zero-padded 2x in each direction before reconstruction. b=0 images were averaged and diffusion-weighted images with opposite gradient polarities were geometrically averaged to reduce contributions from background gradient cross-terms (24). Diffusion and kurtosis tensors were then estimated voxel-wise using a constrained linear least-squares approach (25). From these tensors, DTI indices FA, MD, AD, and RD and DKI indices MK, AK, and RK were calculated on a voxel-wise basis (26). For WMTI analysis, AWF (or $f_{A,\,WMTI}$) was estimated voxel-wise by Eq 8.4:

$$f_{A,WMTI} = \frac{K_{max}}{K_{max} + 3} \qquad [8.4]$$

where K_{max} is the maximum kurtosis over all directions derived from the kurtosis tensor.

After fitting, all parameter maps of a given model were co-registered in order to define closely comparable regions of interest (ROI) in each brain. For each mouse model, the first spin echo image of one brain was arbitrarily defined as the reference and then corresponding image from each other brain was registered to the reference using a rigid affine registration followed by a non-rigid deformable demons registration (27) of the 1st spin echo images. The resulting deformation fields of this registration were then applied to parameter maps. Four ROIs were then drawn corresponding to the four regions extracted for histology (below): 3 in the corpus callosum in the mid-sagittal slice (genu (GCC), mid-body (MidCC), and splenium (SCC)) and the other in the anterior commissure (AC). In addition, a cortical gray matter (GM) ROI was drawn in the sagittal slice for comparison. Mean ROI values from different parameter maps and values derived from histology were compared using two-sample *t*-tests ($\alpha = 0.05$) and linear correlation.

8.2.4 Microscopy

For each brain, after MRI, a 1-2 mm thick sagittal section of tissue was cut from the left hemisphere beginning at the mid-brain. Subsequently, 4 regions of white matter were cut from the slice: the genu, mid-body, and splenium of the corpus callosum and the anterior commissure. Tissue samples were then processed for Transmission Electron Microscopy (TEM) in the Vanderbilt Cell Imaging Shared Resource-Research Electron Microscopy facility. Thick sections (0.5-1 μm) were collected then stained with 1% toluidine blue. Subsequently, ultra-thin section (~ 500 x 500 x 0.07 μm) were cut and then collected on 300-mesh copper grids. Copper grids were stained at room temperature with 2% uranyl acetate (aqueous) for 15 minutes and then with lead citrate for 10 minutes.

Ultra-thin sections were imaged on the Philips/FEI Tecnai T12 electron microscope (FEI Company, Hillsboro, OR) at various magnifications and pictures were acquired with a side-mounted AMT CCD camera. For quantification of myelinated axon microstructure, 6-12 15,000x images were collected (~300 axons) per ROI per animal. Each image was analyzed semi-automatically to derive myelin volume fraction ($f_{M,HIST}$), axon volume fraction ($f_{A,HIST}$), mean axon diameter ($\bar{d}$), and mean myelin thickness ($\bar{\Delta}$).

The histology pipeline was implemented using MATLAB 2015a (The Mathworks, Natick MA) and is shown in Fig 5.2. First, a local Otsu threshold was applied to each image, resulting in a binary image (myelin=1, non-myelin=0). In this binary image, the operator manually identified an intra-axonal point of each myelinated axon and corrected the labeling of pixels that were deemed to be erroneous identified as myelin. Beginning from each manually identified seed point, an active contour algorithm (28) was used to segment each individual axon. The resulting image (Fig 5.2d) provided per axon measures of area and diameter (a_{ax} and $d = 2*\sqrt{a_{ax}/\pi}$,

respectively) and total axon volume fraction. (Note that only axons lying fully within the image frame were included in the per-axon measures, but all axon area contributed to the axon volume fraction.)

Because the Otsu threshold resulted in uneven segmentation of the myelin, the myelin of each myelinated axon was independently segmented on the original histology image using the final boundary of the axon segmentation as the starting contour. Each contour was grown outward along lines normal to its tangent (~0.06μm/line) until reaching a pixel intensity greater than the average intensity of pixels from the initial contour (Fig 5.2e). In order to reject normal lines that grew into the myelin of adjacent axons, a line was discarded if 1) its terminal point matched the location of an axon boundary defined above, or 2) length was more than 3 times the median absolute deviation (29). The ends of the remaining normal lines created a contour defining the outer myelin boundary, and the median length of these lines defined the myelin thickness for that axon, Δ. Finally, myelin area for each axon was determined by uniformly growing the initial contour of each axon to a uniform thickness, Δ as shown in Fig 5.2f. The resulting binary image provided a measure of myelin volume fraction, $f_{M,HIST}$, for each image. g_{HIST} was calculated per image using $f_{A,HIST}$ and $f_{M,HIST}$ in *Eq* 8.1. Across all images per mouse model and brain region, mean values of $\overline{f_{M,HIST}}$, $\overline{f_{A,HIST}}$, $\overline{d}$, and $\overline{\Delta}$, and $\overline{g_{HIST}}$ were calculated.

8.3. RESULTS

Fig 8.1 displays g_{HIST} against $f_{M,HIST}$. We see expected significant decreases in g_{HIST} for *Rictor* CKO and increases in g_{HIST} for *Pten* CKO mice compared to control mice in agreement with decreases and increases in $f_{M,HIST}$, respectively. However, in the *Tsc2* CKO model there is bulk

loss of myelination while the remaining myelinated axons maintain g_{HIST} measures similar to controls.

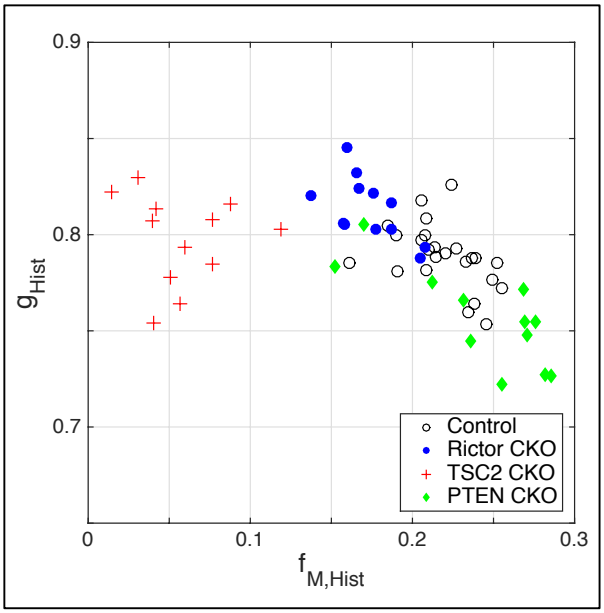

Figure 8.1. g-ratio versus myelin volume fraction. Scatter plot of g_{HIST} versus $f_{M,HIST}$ from control, *Rictor CKO*, *Tsc2* CKO, and *Pten* CKO mice

Figure 8.2a shows MRI measures of myelin volume fraction ($f_{M,T2}$ and $f_{M,MT}$) versus histologic myelin volume fraction, $f_{M,HIST}$. $f_{M,T2}$ and $f_{M,MT}$ display strong correlation (ρ = 0.83 and 0.84, respectively) as shown previously (*See* Chapter 5). Using both measures of myelin volume fraction, axon volume fraction ($f_{A,WMTI}$) is calculated as AWF*(1- $f_{M,T2}$ or $f_{M,MT}$). Fig 8.2b displays $f_{A,WMTI}$ versus $f_{A,HIST}$ showing strong correlation (ρ = 0.60 and 0.58, respectively). There is little difference in $f_{A,WMTI}$ between control, *Rictor* CKO, and *Pten* CKO mice. Red lines display correlations considering all data except *Tsc2* CKO mice, with very weak ($f_{M,T2}$) and non-significant ($f_{M,MT}$) correlation. While $f_{M,T2}$ and $f_{M,MT}$ lie near the line of unity, $f_{A,WMTI}$ overestimates $f_{A,HIST}$ in all cases, especially in the *Tsc2* CKO mice. This is because $f_{A,HIST}$ is

specific to myelinated axons while $f_{A,WMTI}$ provides an area-weighted measure of all myelinated and unmyelinated axons.

Next, the MRI measures for MVF and AVF are used to calculate g_{T2} and g_{MT} (MVF = $f_{M,T2}$ or $f_{M,MT}$ and AVF = $f_{A,WMTI}$ = AWF * [1- $f_{M,T2}$ or $f_{M,MT}$]) from *Eq* 8.1. There is good correlations to g_{HIST} (ρ = 0.64 and 0.57, respectively) shown in Fig 8.2c. As before, both g_{T2} and g_{MT} slightly overestimate g-ratio compared to g_{HIST} due to the unmyelinated axon contribution from $f_{A,WMTI}$. g_{T2} displays slightly higher RMSE (0.094) compared to g_{MT} (RMSE=0.085). However, g_{T2} lies tighter to the line of best fit but with slope > 1, which may be due to intercompartmental water exchange effects, decreasing $f_{M,T2}$. In accord with g_{HIST}, both g_{T2} and g_{MT} depict a significant increase between control and *Rictor* CKO mice but only g_{T2} displays a significant decrease from controls in *Pten* CKO.

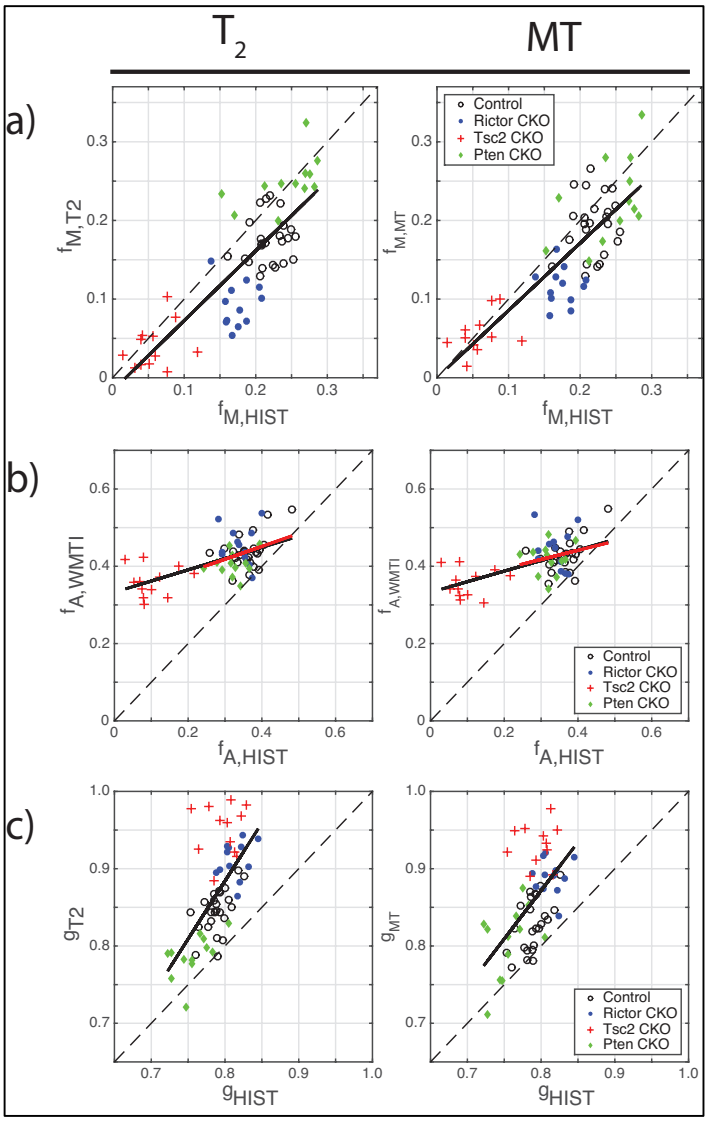

Figure 8.2. MRI versus histology scatter plots. a) $f_{M,T2}$ and $f_{M,MT}$ versus $f_{M,HIST}$, b) $f_{A,WMTI}$ using $f_{M,T2}$ and $f_{M,MT}$ versus $f_{A,HIST}$, c) g_{T2} and g_{MT} versus g_{HIST} from control, *Rictor CKO*, *Tsc2* CKO, and *Pten* CKO mice

Fig 8.3 displays g_{T2} and g_{MT} values from white matter overlaid on T_2-weighted images (T_E = 5.8ms) from control, *Rictor* CKO, *Tsc2* CKO, and *Pten* CKO brains. The two maps display similar values across the corpus callosum with expected changes in CKO models similar to Fig 8.2c.

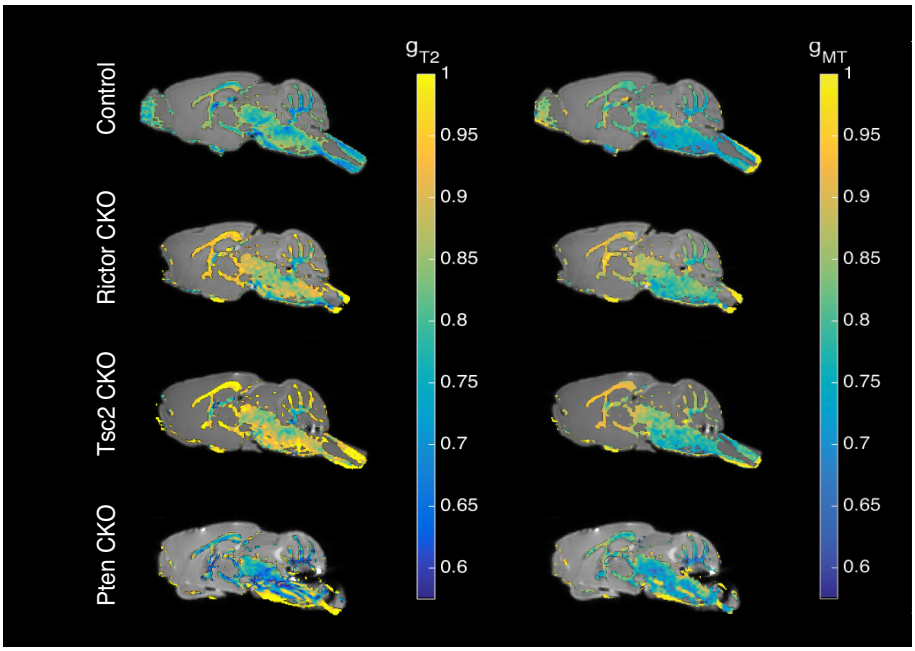

Figure 8.3. Represenative MRI g-ratio maps. g_{T2} and g_{MT} maps from sagittal slice from control, *Rictor CKO*, *Tsc2* CKO, and *Pten* CKO mice.

8.4. DISCUSSION

$f_{M,T2}$ or $f_{M,MT}$ reports on changes in myelination, which could be due to either axonal loss or demyelination. $f_{A,WMTI}$ can detect bulk axon loss but the state of myelination is otherwise unknown. Using both measures, an estimate of g-ratio can be calculated which describes the relationship between axon size and myelin thickness in each voxel. This allows for a better understanding of changes on a microstructural level to discriminate between axon loss and demyelination.

However, to accurately assess pathology, we need to fully understand what MRI measures of MVF and AVF are providing. If we consider the case of *Tsc2* CKO mice, Fig 8.1 displays that although much myelin is lost, the histology measures show that the remaining myelinated axons display g_{HIST} similar to control mice (~0.75 - 0.83). $f_{M,T2}$ and $f_{M,MT}$ reflect the drastict reduction in myelin similar to $f_{M,HIST}$. However, as shown in Fig 8.2b, f_{AWMTI} (or any

axon water fraction measure from MRI) reports only a small decrease in axons compared to $f_{A,HIST}$ in *Tsc2* CKO mice. Therefore, g_{MRI} reports the area-weighted g-ratio of all axons, not just myelinated axons. From this, we cannot distinguish if the remaining myelinated axons are healthy. This is exemplified by the diagram in Fig 8.4. Here, there are 3 diseased voxels, that all began as a normal, control tissue voxel. In voxel 1, half of the axons were lost while the remaining axons remain normally myelinated. In voxel 2, there is no axon loss, but all myelin becomes thinner. And in voxel 3, again there is no axon loss, but half of the axons become dysmyelinated while the others remain normally myelinated. Using our MRI measures of MVF and AVF to calculate g_{MRI}, we would be able to detect all diseased voxels from normal tissue. We could assess differences between voxels 1 and 2/3 due to both axon and myelin loss in voxel 1. However, we cannot discriminate bewteen voxels 2 and 3 since our measure of AWF will remain the same. In many cases, it may be enough to distinguish disease from normal (which should be feasible), but it is important when developing a new metric to thouroughly assess its merits and limitations.

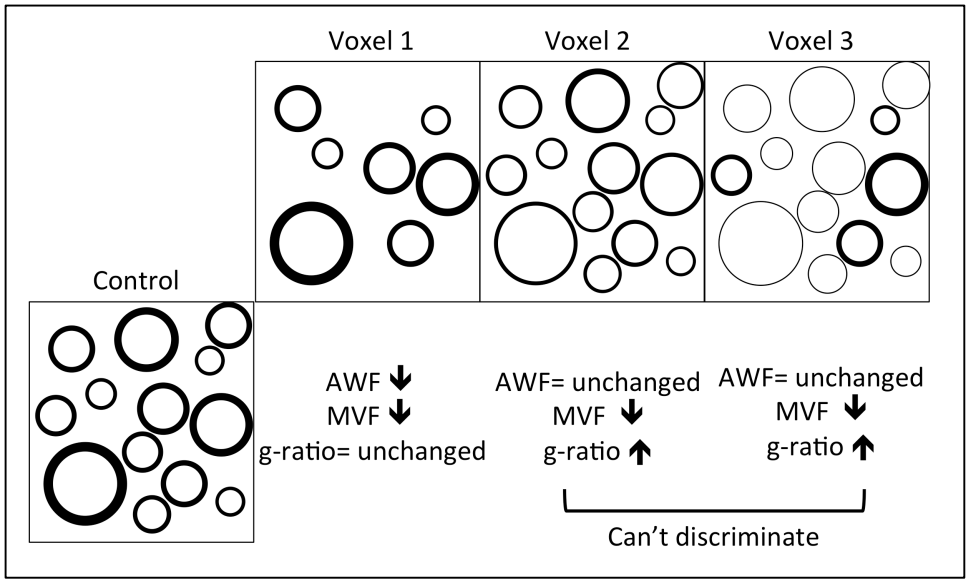

Figure 8.4. Diagram of g-ratio imaging limitations. a) $f_{M,T2}$ and $f_{M,MT}$ versus $f_{M,HIST}$, b) $f_{A,WMTI}$ using $f_{M,T2}$ and $f_{M,MT}$ versus $f_{A,HIST}$, c) g_{T2} and g_{MT} versus g_{HIST} from control, *Rictor CKO*, *Tsc2* CKO, and *Pten* CKO mice.

In contrast to Fig 8.3b, previous work has displayed changes in AWF from WMTI due to decreases in myelin fraction. This results from an increase in extra-axonal water fracton since myelin is considered to be 'silent' (30,31); However, here, we are normalizing AWF by including the myelin fraction, so we are only sensitive to changes in the intra-axonal fraction. It is apparent from Fig 8.3b that $f_{A,WMTI}$ is relatively consistent between control, *Rictor* and *Pten* CKO mice which is consistent with $f_{A,HIST}$ measures across models displayed previously (*See* Chapter 5). This is not suprising since these models do not display large axonal loss. A limitation of the WMTI model is the assumption of highly aligned white matter tracts (13). While this is not a problem in the corpus callosum, it will not be translatable to all white matter tracts. Besides the WMTI model, there are numerous other diffusion models that can be used to estimate the axon water fraction as used previously (8,32) but many of the same issues remain regardless of the model used. We attempted to apply the NODDI model to our data, but the resulting NODDI parameters were highly sensitive to *a priori* assumptions of intrinsic diffusivity, which is unknown in *ex vivo* tissue.

However, it may be possible to assess myelin thickness without the need for diffusion models. It has been shown that MET_2 estimates of myelin volume fraction may be sensitive to the thickness of the myelin (33–35, Ch 5) As shown in Dula et al., we can use the sensitivity of MET_2 to exchange and the robustness of qMT to probe myelin thickness. Using our measures of myelin volume fraction ($f_{M,T2}$ and $f_{M,MT}$) we can compare the measures one-to-one. Fig 8.6a displays the ratio of $f_{M,T2}$ to $f_{M,MT}$ versus mean myelin thickness ($\overline{\Delta}$). While these measures are a bit noisy, we see the expected trend with ratios closer to 1 as $\overline{\Delta}$ increases. We can also compare $f_{M,T2}$ to the recently proposed measure of myelin volume from proton density measures (36).

While we did not measure proton density directly, the total water content (M_0) is the sum of the T_2 spectrum for each voxel. We can normalize M_0 in our white matter ROIs to M_0 in gray matter to obtain normalized water content (NWC) as displayed previously (*See* Chapter 5). Next, since we do not have a pure water reference marker, we can assume that when myelin volume = 0, the ratio of WM/GM should = 1. Therefore we can subtract an offset (δ ~0.11). Then, our estimate of $f_{M,PD}$ will simply be 1-[NWC-δ]. Again in Fig 8.6b we can display the ratio of $f_{M,T2}$ to $f_{M,PD}$ versus mean myelin thickness ($\overline{\Delta}$), since total proton density should not be affected by exchange. We see slightly noisier but similar results. However, with the addition of a reference water marker (which would likely increase precision), this technique would allow for assessment of myelin thickness using only MET_2.

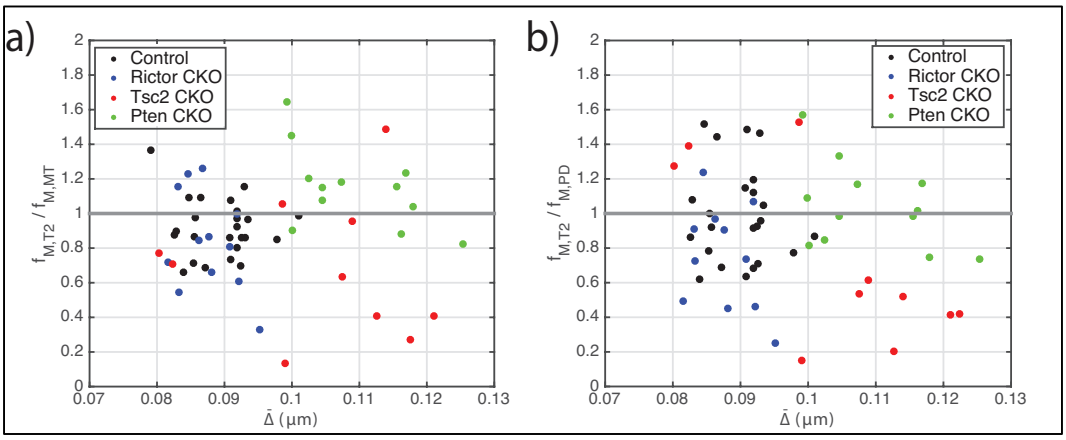

Figure 8.5. Myelin volume fraction ratio versus myelin thickneess. a) $f_{M,T2}$ / $f_{M,MT}$ versus $\overline{\Delta}$, b) $f_{M,T2}$ / $f_{M,PD}$ versus $\overline{\Delta}$, from control, *Rictor CKO*, *Tsc2* CKO, and *Pten* CKO mice

Beyond myelin thickness, to assess possible differences in myelin ultrastructure (i.e., changes in myelin wrapping), we acquired TEM images at 350,000X from 3 axons in the splenium region from a control animal and one animal from each CKO model. Figures 8.6a,b display an example image with a profile line (blue) drawn across the myelin. Fig 8c displays the line profile

intensities (blue) and after smoothing with a 12-pt moving average (red line). The peaks (red circles) correspond to the middle of each myelin water layer. The width of each layer is calculated by finding the peaks (green circles) and troughs (black circles) of the derivative of the smooth line profile to determine where the layer of myelin water begins and ends, respectively (Fig 8c). We applied the same process to the inverted profile line to determine the size of myelin lipid layers.

Figure 8d displays the mean +/- SEM thickness of myelin water and lipid layers. From the image in Fig 8b, we cannot distinguish betwwen major dense lines and intraperiod lines, but this is consistent with data from similar aged (P60) rats with similar peridocity measures (~10nm) (37) . *Tsc2* CKO and *Pten* CKO mice appear to have thinner water and lipid layers, but as seen before (Fig 5.4) thicker overall myelin thickness ($\overline{\Delta}$) compared to control and *Rictor* CKO mice. From simulations, we know that MWF will be less affected by intercompartmental water exchange as myelin layer packing density and/or overall myelin thickness increases. These changes in micro- and ultra-structure in *Tsc2* CKO and *Pten* CKO mice could explain the lack of underestimation of $f_{M,T2}$ in Fig 8.5 as compared to control and *Rictor* CKO data points. While our MRI measures show there might be a minor exchange effect, in this *ex vivo* application, water diffusion is much slower and exchange effects are not as drastic as previously exhibited in spinal cord or peripheral nerve (33,34,38) .

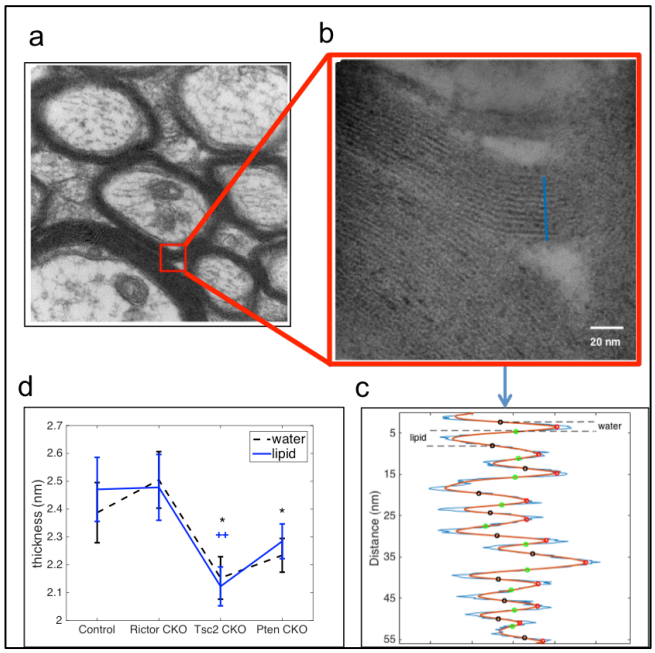

Figure 8.6. Myelin ultrastructure analysis a) 67,000X TEM image of a control axon. b) 350,000X TEM image of myelin layers and line profile. c) (blue) myelin intesity along line profile, (red) smoothed line profile with (red, circle) myelin water peaks and (black and green circles) peaks and troughs of the derivative of smooth line profile, respectively. Myelin water and lipid layers are denoted. d,) myelin (black, dahed) water and (blue) lipid thicknesses, across mouse models with (*, +) denoting significant differences to control and *Rictor* CKO.

Beyond the sensitivites of MVF and AVF shown here, it is also important to remember that g_{MRI} is inherently an area-weighted measure. Therefore, during diseases targeting either large (amyotrophic lateral sclerosis (37)) or small axons (cuprizone model of demyelination (30,38,39) or changes during development where large axons are typically myelinated first (40,41), the observed g_{MRI} will more heavily reflect changes in the larger axons. In addition, the g-ratio is not constant across axon size, with larger axons generally having higher g-ratios (42); hence, if the distribution of axons in tissue changes, a different g_{MRI} may be detected.

8.5. CONCLUSIONS

Imaging g-ratio with MRI, necessitates accurate measures of both myelin volume and axon volume fraction. Using recent work to obtain MRI myelin volume fractions, we display good correlations between histologic and MRI g-ratios across multiple mouse models. However, we also highlight some sensitivities and possible limitations to the method—a) g_{MRI} provides an axon-area-weighted g-ratio, b) axon water fraction from models of diffusion are sensitive to all axons, c) myelin volume fractions from MET_2 may be affected by intercompartmental water exchange and those from qMT require calibration. As shown here, while these can be limitations, they may also be opportunities to gain more information about the tissue such as myelin thickness. This study shows the potential and promise for imaging myelin microstructure and the g-ratio non-invasively using MRI.

8.6 REFERENCES

1. Laule, Vavasour, Kolind, Li D. Magnetic resonance imaging of myelin. 2007.

2. Bartzokis G. Age-related myelin breakdown: a developmental model of cognitive decline and Alzheimer's disease. Neurobiology of aging 2004;25:5–18.

3. Weinstein M, Ben-Sira L, Levy Y, Zachor DA, Ben Itzhak E, Artzi M, Tarrasch R, Eksteine PM, Hendler T, Ben Bashat D. Abnormal white matter integrity in young children with autism. Hum Brain Mapp 2011;32:534–43. doi: 10.1002/hbm.21042.

4. Mighdoll MI, Tao R, Kleinman JE, Hyde TM. Myelin, myelin-related disorders, and psychosis. Schizophrenia research 2015;161:85–93. doi: 10.1016/j.schres.2014.09.040.

5. Menzies L, Chamberlain SR, Laird AR, Thelen SM, Sahakian BJ, Bullmore ET. Integrating evidence from neuroimaging and neuropsychological studies of obsessive-compulsive disorder: the orbitofronto-striatal model revisited. Neuroscience and biobehavioral reviews 2008;32:525–49. doi: 10.1016/j.neubiorev.2007.09.005.

6. Rushton W. A theory of the effects of fibre size in medullated nerve. The Journal of Physiology 1951;115:101–22. doi: 10.1113/jphysiol.1951.sp004655.

7. Chomiak, Hu. What is the optimal value of the g-ratio for myelinated fibers in the rat CNS? A theoretical approach. 2009. doi: 10.1371/journal.pone.0007754.

8. Stikov N, Campbell JS, Stroh T, Lavelée M, Frey S, Novek J, Nuara S, Ho M-K, Bedell BJ, Dougherty RF. In vivo histology of the myelin g-ratio with magnetic resonance imaging. NeuroImage 2015;118:397–405. doi: 10.1016/j.neuroimage.2015.05.023.

9. Stikov N, Perry L, Mezer A, Stikov N, Perry LM, Mezer A, Rykhlevskaia E, Wandell B, Pauly J, Dougherty R. Bound pool fractions complement diffusion measures to describe white matter micro and macrostructure. NeuroImage 2011;54:1112–21. doi: 10.1016/j.neuroimage.2010.08.068.

10. West K, Kelm N, Carson R, Does M. A revised model for estimating g-ratio from MRI. NeuroImage 2016;125:1155–8.

11. Zhang H, Schneider T, Wheeler-Kingshott C, Alexander D. NODDI: practical in vivo neurite orientation dispersion and density imaging of the human brain. Neuroimage 2012;61:1000–16.

12. Reisert M, Mader I, Umarova R, Maier S, Tebartz van Elst L, Kiselev VG. Fiber density estimation from single q-shell diffusion imaging by tensor divergence. NeuroImage 2013;77:166–76. doi: 10.1016/j.neuroimage.2013.03.032.

13. Fieremans E, Jensen JH, Helpern JA. White matter characterization with diffusional kurtosis imaging. NeuroImage 2011;58:177–88. doi: 10.1016/j.neuroimage.2011.06.006.

14. Carson R, Kelm N, West K, Does M, Fu C, Weaver G, McBrier E, Parker B, Grier M, Ess K. Hypomyelination following deletion of Tsc2 in oligodendrocyte precursors. Annals of Clinical Translational Neurology 2015;2:1041–54. doi: 10.1002/acn3.254.

15. Carson RP, Fu C, Winzenburger P, Ess KC. Deletion of Rictor in neural progenitor cells reveals contributions of mTORC2 signaling to tuberous sclerosis complex. Human Molecular Genetics 2013;22:140–52. doi: 10.1093/hmg/dds414.

16. Harrington EP, Zhao C, Fancy SP, Kaing S, Franklin RJ, Rowitch DH. Oligodendrocyte PTEN is required for myelin and axonal integrity, not remyelination. Annals of Neurology 2010;68:703–16. doi: 10.1002/ana.22090.

17. Hennig J. Echoes—how to generate, recognize, use or avoid them in MR-imaging sequences. Part II: Echoes in imaging sequences. Concepts in Magnetic Resonance 1991;3:179–92. doi: 10.1002/cmr.1820030402.

18. Lebel MR, Wilman AH. Transverse relaxometry with stimulated echo compensation. Magnetic Resonance in Medicine 2010;64:1005–14. doi: 10.1002/mrm.22487.

19. Prasloski T, Mädler B, Xiang Q. Applications of stimulated echo correction to multicomponent T2 analysis. Magnetic Resonance in Medicine 2012;67:1803–14. doi: 10.1002/mrm.23157.

20. Gochberg DF, Gore JC. Quantitative magnetization transfer imaging via selective inversion recovery with short repetition times. Magnetic Resonance in Medicine 2007;57:437–41. doi: 10.1002/mrm.21143.

21. Does MD. Multi-Exponential Relaxation Analysis (MERA) Toolbox, Version 2, http://www.vuiis.vanderbilt.edu/~doesmd/MERA/MERA_Toolbox.html. 2014.

22. Whittall K, MacKay A. Quantitative interpretation of NMR relaxation data. Journal of Magnetic Resonance 1989;84:134–52. doi: 10.1016/0022-2364(89)90011-5.

23. Li K, Zu Z, Xu J, Janve V, Gore J, Does M, Gochberg D. Optimized inversion recovery sequences for quantitative T1 and magnetization transfer imaging. Magnetic Resonance in Medicine 2010;64:491–500. doi: 10.1002/mrm.22440.

24. Neeman M, Freyer J, Sillerud L. A simple method for obtaining cross-term-free images for diffusion anisotropy studies in NMR microimaging. Magnetic Resonance in Medicine 1991;21:138–43. doi: 10.1002/mrm.1910210117.

25. Tabesh A, Jensen J, Ardekani B, Helpern J. Estimation of tensors and tensor-derived measures in diffusional kurtosis imaging. Magnetic Resonance in Medicine 2011;65:823–36. doi: 10.1002/mrm.22655.

26. Jensen J, Helpern J. MRI quantification of non-Gaussian water diffusion by kurtosis analysis. NMR in Biomedicine 2010;23:698–710. doi: 10.1002/nbm.1518.

27. Thirion J-P. Image matching as a diffusion process: an analogy with Maxwell's demons. Medical Image Analysis 1998;2:243–60. doi: 10.1016/S1361-8415(98)80022-4.

28. Kass M, Witkin A, Terzopoulos D. Snakes: Active contour models. International Journal of Computer Vision 1988;1:321–31.

29. Leys C, Ley C, Klein O, Bernard P, Licata L. Detecting outliers: Do not use standard deviation around the mean, use absolute deviation around the median. Journal of Experimental Psychology 2013;49:764–6.

30. Jelescu I, Zurek M, Winters K, et al. In vivo quantification of demyelination and recovery using compartment-specific diffusion MRI metrics validated by electron microscopy. Neuroimage 2016;132:104–14.

31. Kelm ND, West KL, Carson RP, Gochberg DF, Ess KC, Does MD. Evaluation of diffusion kurtosis imaging in ex vivo hypomyelinated mouse brains. NeuroImage 2016;124:612–26. doi: 10.1016/j.neuroimage.2015.09.028.

32. Mohammadi S, Carey D, Dick F, Diedrichsen J, Sereno MI, Reisert M, Callaghan MF, Weiskopf N. Whole-brain in-vivo measurements of the axonal g-ratio in a group of 37 healthy volunteers. Frontiers in neuroscience 2015;9:1–13. doi: 10.3389/fnins.2015.00441.

33. Dula AN, Gochberg DF, Valentine HL, Valentine WM, Does MD. Multiexponential T2, magnetization transfer, and quantitative histology in white matter tracts of rat spinal cord. Magnetic Resonance in Medicine 2010;63:902–9. doi: 10.1002/mrm.22267.

34. Harkins K, Dula A, Does M. Effect of intercompartmental water exchange on the apparent myelin water fraction in multiexponential T2 measurements of rat spinal cord. Magnetic

Resonance in Medicine 2012;67:793–800. doi: 10.1002/mrm.23053.

35. Levesque I, Pike G. Characterizing healthy and diseased white matter using quantitative magnetization transfer and multicomponent T2 relaxometry: A unified view via a four-pool model. Magnetic Resonance in Medicine 2009;62:1487–96. doi: 10.1002/mrm.22131.

36. Mezer A, Yeatman J, Stikov N, et al. Quantifying the local tissue volume and composition in individual brains with magnetic resonance imaging. Natue Medicine 2013;19:1667–71. doi: 10.1038/nm.3390.

37. Xie F, Liang P, Fu H, Zhang J. Effects of normal aging on myelin sheath ultrastructures in the somatic sensorimotor system of rats. Molecular Medicine Reports 2014;10:459–66. doi: 10.3892/mmr.2014.2228.

38. Dortch RD, Harkins KD, Juttukonda MR, Gore JC, Does MD. Characterizing inter compartmental water exchange in myelinated tissue using relaxation exchange spectroscopy. Magnetic resonance in medicine 2013;70:1450–59. doi: 10.1002/mrm.24571.

39. Nguyen M, Lariviere R, Julien J-P. Reduction of axonal caliber does not alleviate motor neuron disease caused by mutant superoxide dismutase 1. Proceeding of the National Academy of Sciences 2000;97:12306–11. doi: 10.1073/pnas.97.22.12306.

40. Mason J, Langaman C, Morell P, Suzuki K, Matsushima G. Episodic demyelination and subsequent remyelination within the murine central nervous system: changes in axonal calibre. Neuropathology and Applied Neurobiology 2001;27:50–8. doi: 10.1046/j.0305-1846.2001.00301.x.

41. Thiessen JD, Zhang Y, Zhang H, Wang L, Buist R, Bigio MR, Kong J, Li X, Martin M. Quantitative MRI and ultrastructural examination of the cuprizone mouse model of demyelination. NMR in Biomedicine 2013;26:1562–81. doi: 10.1002/nbm.2992.

42. Remahl S, Hildebrand C. Changing relation between onset of myelination and axon diameter range in developing feline white matter. Journal of the Neurological Sciences 1982;54:33–45. doi: 10.1016/0022-510X(82)90216-7.

43. Matthews M, Duncan D. A quantitative study of morphological changes accompanying the initiation and progress of myelin production in the dorsal funiculus of the rat spinal cord. Journal of Comparative Neurology 1971;142:1–22. doi: 10.1002/cne.901420102.

44. Berthold C, Nilsson I, Rydmark M. Axon diameter and myelin sheath thickness in nerve fibres of the ventral spinal root of the seventh lumbar nerve of the adult and developing cat. Journal of anatomy 1983;136:483–508.

CHAPTER 9

CONCLUSIONS AND FUTURE DIRECTIONS

9.1 CONCLUSIONS

Overall, the work in this dissertation aimed to advance the ability to quantitatively assess myelin and white matter microstructure in rodent brains. Before this work, myelin imaging in rodent brain was limited to magnetization transfer techniques and there were only a few studies using quantitative histology for validation. I furthered the field of white matter imaging by filling these holes.

Applying MET_2 to obtain MWF maps in rodent brains had never been shown due to SNR and resolution requirements. Therefore, I assessed optimal parameters to acquire and fit MET_2 data. We saw that use of optimal parameters was not critical at high field strengths with and without gadolinium. Additionally, we displayed the ability to obtain MWF maps in rodent brains for the first time. Next, in order to quantitatively evaluate our MRI techniques, we needed methods to accurately analyze electron microscopy images. Therefore, I developed analysis code to reproducibly calculate myelin volume fraction, axon volume fraction, axon diameter, myelin thickness, and g-ratio from electron microscopy images to compare to MRI.

Then, I displayed similar results as previous work using current myelin imaging parameters (MWF and BPF) compared to histology in adult mice with normal myelination and multiple models of white matter disease. I used a volumetric model of white matter to extend our

capabilities to myelin volume imaging and validated it against quantitative histology. This provides the ability to obtain histologic-like measures of myelin which can be utilized in models like g-ratio imaging. I also applied myelin volume imaging to normally developing mouse brains and displayed the ability to specifically investigate myelin development.

Finally, I used quantitative histology to evaluate the proposed geometric g-ratio model. I found that it provides an area-weighted g-ratio, which is an important consideration to know when the technique is applied in various disease models. Lastly, I applied g-ratio imaging using our method for myelin volume imaging and axon water fraction from diffusion imaging in adult mouse brains with normal myelination and multiple models of white matter disease. We were able to assess the capability and sensitivity of g-ratio imaging with comparison to quantitative histology. This provides promise for the technique along with an outline of possible limitations.

9.2 FUTURE DIRECTIONS

There are numerous future directions to be taken from the work in this dissertation. First, it is of interest to compare our myelin volume imaging metrics to recently proposed myelin volume from proton density measures (1). While we have attempted to do this using gray matter as a reference, we have started including a water reference to allow comparisons. This technique is of great interest because it is a straightforward measure and more easily translatable to clinical use. However, similar to BPF, this technique will still be affected by non-myelin bound protons.

A second direction of interest is extending g-ratio imaging to compare male and female brains during adolescence and fully matured adults. Previous work has displayed sexual dimorphism of myelin density during adolescence. While white matter area increases in males,

myelin content decreases leading to a higher g-ratio. It is predicted that these changes are due to larger increases in axon size in males, which may be due to testosterone levels (2–4). Using all of the techniques validated in this dissertation, we have the tools necessary to investigate this hypothesis and have begun a study with adolescent and adult male and female rats.

Finally, in addition to assessing disease, it would be useful to also evaluate possible disease treatments. This work provides validation to use MRI to obtain histologic information of myelin volume and g-ratio across whole rodent brains. Using MRI to understand what treatments are doing can aid in and speed up the drug development pipeline in preclinical studies. Additionally, MRI techniques can be translated to patients to assess the disease and treatment in the clinic. Overall, the work in this dissertation furthers the ability of white matter imaging to specifically understand myelin development, disease, and recovery.

9.3 REFERENCES

1. Mezer A, Yeatman J, Stikov N, et al. Quantifying the local tissue volume and composition in individual brains with magnetic resonance imaging. Natue Medicine 2013;19:1667–71. doi: 10.1038/nm.3390.

2. Paus T, Toro R. Could Sex Differences in White Matter be Explained by g ratio? Front Neuroanat 2009;3:14. doi: 10.3389/neuro.05.014.2009.

3. Perrin JS, Leonard G, Perron M, Pike GB, Pitiot A, Richer L, Veillette S, Pausova Z, Paus T. Sex differences in the growth of white matter during adolescence. Neuroimage 2009;45:1055–66. doi: 10.1016/j.neuroimage.2009.01.023.

4. Perrin J, Hervé P-Y, Leonard G, Perron M, Pike B, Pitiot A, Richer L, Veillette S, Pausova Z, Paus T. Growth of White Matter in the Adolescent Brain: Role of Testosterone and Androgen Receptor. J Neurosci 2008;28:9519–9524. doi: 10.1523/JNEUROSCI.1212-08.2008.